MIGRATION KINETICS OF ANTIPHASE BOUNDARIES IN Fe - Al ORDERED ALLOYS

by

WOONSUP PARK

B.S. Seoul National University, Korea
(1980)

M.S. Seoul National University, Korea
(1982)

Submitted to the Department of Materials Science
and Engineering in Partial Fulfillment of the
Requirements of the Degree of

DOCTOR OF PHILOSOPHY

at the

MASSACHUSETTS INSTITUTE OF TECHNOLOGY

May 1988

Signature of Author _____
Department of Materials Science and Engineering
April 29, 1988

Certified by _____
Samuel M. Allen
Associate Professor, Physical Metallurgy
Thesis Supervisor

Accepted by _____
John B. Vander Sande
Chairman, Departmental Committee on Graduate Students

MIGRATION KINETICS OF ANTIPHASE BOUNDARIES IN Fe - Al ORDERED ALLOYS

by

WOONSUP PARK

Submitted to the Department of Materials Science and Engineering on April 29, 1988 in partial fulfillment of the requirements for the Degree of Doctor of Philosophy.

ABSTRACT

Migration kinetics of antiphase boundaries (APBs) in the B2 and DO_3 ordered phases of the Fe-Al system, with the alloy compositions of 24-26 percent of aluminum, have been investigated experimentally. Theoretical efforts to model the structures of the APBs have also been made using an improved Bragg-Williams model.

In the experimental part of the study, the focus was on the direct relationship between the instantaneous local curvature and the instantaneous velocity of the moving APBs. Although this relationship is the basis of the kinetics of the migration of APBs and of domain coarsening, there have been no experimental studies to establish this relationship because of the difficulties involved in measuring the local curvatures. New experimental techniques, employing in-situ hot-stage transmission electron microscopy, have been developed to directly address this problem, and the mobility of the migrating APBs, which is the proportionality constant relating the velocity to the local curvature, has been successfully determined for the first time using these techniques.

Three orders of magnitude change in kinetics could be covered in our experiments. The mobility of the APBs in the Fe-26%Al alloy is ranging from 4.8×10^{-19} m^2/s at 745K to 4.7×10^{-18} m^2/s at 800K for the APBs in the DO_3 phase, and from 1.7×10^{-17} m^2/s at 838K to 1.5×10^{-16} m^2/s at 910K for the APBs in the B2 phase. From the temperature dependency of M, the activation energies of the APB migration in both B2 and DO_3 phases have been calculated to be about 2×10^5 J/mol which are very similar to the activation energy of the interdiffusion in the disordered A2 phase of the Fe-Al system. From the comparison of the results of these in-situ experiments with the results of conventional bulk coarsening experiments, it is concluded that the mobility M determined from in-situ experiments is truly intrinsic.

An improved description of the free energy of Fe-Al solid solution has been achieved using a Bragg-Williams model with pairwise interactions to third neighbors, and using composition-dependent interaction energies calculated from the experimental phase diagram. Gradient energy coefficients for order parameters and the composition in the Fe-Al system have been derived using the improved Bragg-Williams model, giving positive values for the order parameters and negative values for the composition, which are consistent with the known fact that the Fe-Al system tends to order.

Due to the negative value of the gradient energy coefficient for the composition, it was not possible to use continuum diffuse interface theory to calculate the solute drag force on APB migration, which would be present if there were composition variations at the APBs. Assuming no composition variation at APBs, the order parameter profiles and the energies of APBs in the Fe-Al ordered alloys have been calculated approximately using continuum diffuse interface theory. Calculated results are comparable to those obtained in previous work and show good agreement with expected trends resulting from changes of temperature and composition.

Thesis supervisor: Dr. Samuel M. Allen
Title: Associate Professor of Physical Metallurgy

Table of Contents

LIST OF FIGURES

LIST OF TABLES

Tables

ACKNOWLEDGEMENTS

I would like to express my appreciation and gratitude to many individuals whose support and assistance make this thesis possible.

My foremost gratitude goes to Professor Samuel M. Allen. His insights and suggestions throughout this research were invaluable. He is the one who made my education at M.I.T. possible by offering me a research assistantship when I was looking for an opportunity to pursue advanced education in the United States. I also wish to thank him and his family for their hospitality.

I would also like to thank Professors R. W. Balluffi and Y. -M. Chiang for agreeing to be on my thesis committee. Their suggestions and comments on this work have been very much appreciated. I am especially grateful to Professor Balluffi for his role as the acting thesis supervisor for the last several months of this study while Professor Allen was on sabbatical leave.

Helpful advice and critical review of the draft of this work by Professor J. E. Krzanowski of University of New Hampshire are gratefully appreciated. He also was on my thesis committee as an outside reviewer.

Excellent technical supports by the technical staffs of the Center for Materials Science and Engineering at M.I.T. are also appreciated. I would like to thank Mike Frongillo and Gabriella Chapman for their support in using the electron microscope facility.

Many fellow graduate students helped me through ups and downs of my days at M.I.T. I could not mention them all, but I feel obligated to thank Dr. Taewook Kang for his help during my early days at M.I.T. and for lending me his expertise in numerical analysis.

Alloys used in this study were kindly provided by William Kerr of the Air Force Wright Aeronautical Laboratories. This research project has been supported by the National Science Foundation Grants 8022277-DMR and 8606706-DMR.

My deepest gratitude goes to my family members who have been always supportive through this educational journey. My parents have been so dedicated to the education of their children, and their encouragement and belief in me drove me to excel from the early stages of my education. My brother, Dr. H. Park made the cultural adjustment easy for me when I first came to the U.S. and has always been my inspiration. I also feel special need to mention my parents-in-law who have stood by me with all their love and guidance.

Words are insufficient to thank my wife Grace Young Min for her understanding, patience and support throughout our years at M.I.T. She sacrificed her own career to support me in every aspect imaginable. Our daughter Jane has been the center of our family life ever since she was born, and she never ceases to amuse us.

Finally I thank God, my Lord for all his blessings to me and my family.

CHAPTER 1

INTRODUCTION

Interfacial surfaces in solids, such as grain boundaries, interphase boundaries, and antiphase boundaries, migrate to reduce their area, and hence the total excess free energy associated with the boundaries. A number of driving forces can cause the migration, such as capillarity, stress, or the free energy change from a phase transformation. To understand the migration kinetics of interfaces, it is necessary to know the relationship between the rate of migration and the driving force.

Depending on the extent of atomic rearrangement occurring as the interface migrates, interfacial migration can be categorized into two groups. In some interfaces, such as grain boundaries in pure metals, martensitic phase boundaries, and twin boundaries, only a structural change involving atomic movements over the distance of the order of an atomic spacing is required for migration. Migration of the martensitic phase boundaries and twin boundaries are athermal migration whereas the grain boundary migration is a thermal process. On the other hand, long-range diffusion is required for the growth of precipitates from supersaturated solid solution and the migration of interfaces with segregation. The interfacial velocity-driving force relationships and mobilities for both types of migration have been the subject of many studies, especially in grain boundaries. The relatively simple structure of antiphase boundaries (APB) has made theoretical modelling of these boundaries feasible and there have been some studies on the migration kinetics of antiphase boundaries in ordered alloys.

Several velocity-driving force relationships have been proposed for different types of migration. But most of the existing experimental techniques are not adequate for direct experimental determination of these relationships. In this study, new experimental techniques are developed for studying the migration kinetics of antiphase boundaries in Fe-Al ordered alloys such that the velocity-driving force relationship can be directly studied. A theoretical effort to model the APB structure has also been made.

In this chapter, previous work on migration kinetics of interfaces in general, and antiphase boundaries in particular, are reviewed.

1.1 Migration Kinetics of Interfaces

There have been many studies on the migration kinetics of interfaces both with and without segregation [1-4]. Most of these works are on grain boundaries, which is reviewed in this section.

A widely-used phenomenological theory of interfacial motion [1,2] states that interfacial velocity V is proportional to the thermodynamic driving force, the proportionality constant being a positive quantity called mobility. The driving force is the product of the mean of the local curvature ($K_1 + K_2$) of the boundary and its excess free energy per unit area σ, leading to the relationship

$$V = \mu\sigma(K_1 + K_2) \tag{1-1}$$

where μ is the mobility which in some theories is inversely proportional to interface thickness [2].

Equation (1-1) is certainly valid for the coarsening of a soap froth, due to gas transpiration through curved soap films because of pressure differences. This equation has generally been invoked in models of grain growth [5] and antiphase domain coarsening [6,7]. But generally in applications of Equation (1-1) to experimental situations, σ has been considered a constant. Thus the validity of Equation (1-1) for the system where σ changes with composition, temperature and/or local curvature is doubtful.

A more general velocity equation relating the interfacial mobility μ and the driving force P_d has been suggested by Rath and Hu [8] and is given by:

$$V = \mu(P_d)^n \tag{1-2}$$

For unsegregated boundaries a value of n=1 is usually obtained from ex-

perimental studies.

Excess concentrations of alloy components or impurity species at interfaces may have significant effects on interfacial migration kinetics, interfacial shape stability, and macroscopic material properties. The effect of adsorption on the migration kinetics of a planar interface have been treated in the "solute-drag" theory [9,10] which models the diffusion of solute species whose profile of interaction energy with the interfaces is known. Cahn [10] estimated the impurity drag in two limiting cases of low velocity and high velocity extremes. In the low velocity regime where the impurity drag force is much greater than the intrinsic drag force, the velocity is proportional to driving force at constant composition, and is given by:

$$V = \frac{P_d}{(\frac{1}{\mu_i} + \alpha\bar{c})} \tag{1-3}$$

Where μ_i is the intrinsic mobility (mobility of the unsegregated boundary) and α is given by:

$$\alpha = 4N_v\, k_B\, T \int \frac{\sinh^2 \frac{E(x)}{2k_B T}}{D(x)}\, dx \tag{1-4}$$

Where E(x) and D(x) are the interaction energy between impurities and the grain boundary, and the diffusion coefficient of impurities respectively as functions of distance. For capillarity-driven boundaries where the impurity drag force is much greater than the intrinsic drag force, the velocity in the low velocity extreme can be written as:

$$V = \mu\sigma(K_1 + K_2) \tag{1-5}$$

where $$\mu = \frac{1}{N_v k_B T \alpha \bar{c}} \tag{1-6}$$

At the high velocity/high driving force extreme, the velocity is given by:

$$V = \mu_i P_d - (\frac{\alpha}{\beta^2})\frac{\bar{c}}{P_d} \tag{1-7}$$

where $$\frac{\alpha}{\beta^2} = \frac{N_v}{k_B T} \int D(x) \left(\frac{dE}{dx}\right)^2 dx \tag{1-8}$$

At sufficiently high driving forces, the velocity equation is similar to the expression for intrinsic migration, Equation (1-2) with n=1. In this case, the boundary effectively breaks away from impurity segregation and the migration kinetics become similar to that of an unsegregated boundary. In between the low and high velocity extremes, a transition region was identified. The solution in this region indicates the velocity may be unstable and migration at both low and high velocity extremes is possible.

Hillert and Sundman [11] studied solute drag applying an energy dissipation theorem and generalized the solute drag theory in order to treat phase interfaces as well as grain boundaries. In both studies of solute drag effects [10,11], an exact profile of impurity concentration is needed to calculate the parameters describing the impurity drag phenomena. But there have been no theoretical calculations of impurity profiles in the grain boundary regions. Krzanowski and Allen [12] calculated the composition profiles in antiphase boundaries (APBs) in Fe-rich Fe-Al alloys in order to study the effects of composition changes at APBs on migration kinetics.

Despite the lack of specific theoretical calculations of solute profiles, the basic results of the impurity drag theory have been experimentally observed. The results of Rutter and Aust [13] on the effects of silver, gold, and tin in lead are explained by impurity drag theory [10]. The existence of both high and low velocity extremes was experimentally demonstrated by Frois and Ditrimov [14] in studying the effect of magnesium impurity in aluminum recrystallization, by Sun and Bauer [15] in studying the migration of [100] tilt boundaries in NaCl bicrystals, and by Glaeser et al. [16] in studying the grain boundary migration in doped and undoped alkali halides. By applying impurity drag theory, Krzanowski and Allen [21,22] explained the observed transition from high velocity extreme to low velocity extreme in the domain coarsening of the APBs in the Fe-Al alloys.

1.2 Migration Kinetics of Antiphase Boundaries (APBs)

Antiphase boundaries (APBs) in ordered phases are structurally simpler than grain boundaries, and consequently, are easier to model theoretically. Equilibrium structures of APBs (structure is taken here to mean variations in order parameter) can be obtained by application of diffuse interface theory [17]. For a planar APB at equilibrium, the order parameter profile can be computed by solving the differential equation

$$\frac{d\eta}{dx} = \left(\frac{\Delta f}{K_\eta}\right)^{\frac{1}{2}} \tag{1-9}$$

where η is the long-range order parameter and Δf is the free energy difference between the free energy in the interfacial region and the free energy of the equilibrium state with order parameter η_e. A schematic diagram of f, the free energy per unit volume of a homogeneous phase, as a function of long-range order parameter η is shown in Figure (1-1). f is an even function of long-range order parameter η when ordering occurs as a higher-order phase transition. K_η is the gradient energy coefficient for ordering introduced to describe the free energy of an inhomogeneously ordered system. A typical APB profile is shown in Figure (1-2). Equation (1-9) can be solved for known Δf when there is no variation in composition near APB, and the excess free energy per unit area σ of a planar APB can be expressed by:

$$\sigma = \int_{-\eta_e}^{+\eta_e} 2(K\,\Delta f)^{\frac{1}{2}} d\eta \tag{1-10}$$

For a coherent interface in an unstrained cubic lattice, σ is shown to be isotropic for diffuse interfaces [17]. An expression for the antiphase

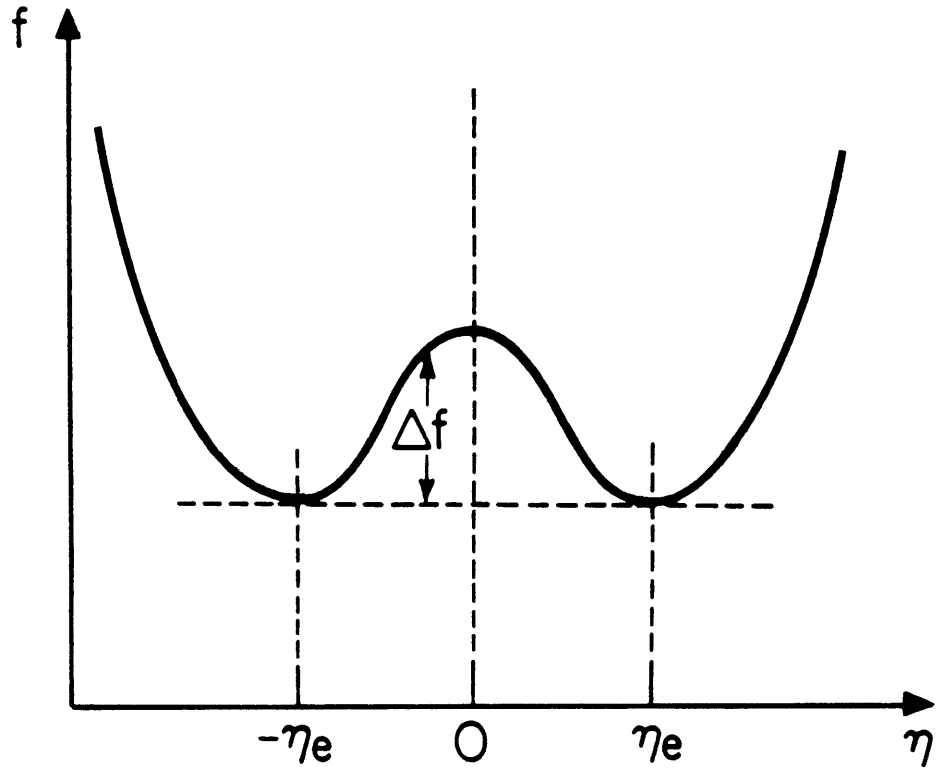

Figure (1-1) The free energy per unit volume, f. f is an even function of long-range order parameter η when ordering occurs as a higher-order transition. Below the critical temperature, f has minima at $\pm\eta_e$. Δf is the increase in f when η differs from η_e. From reference [18]

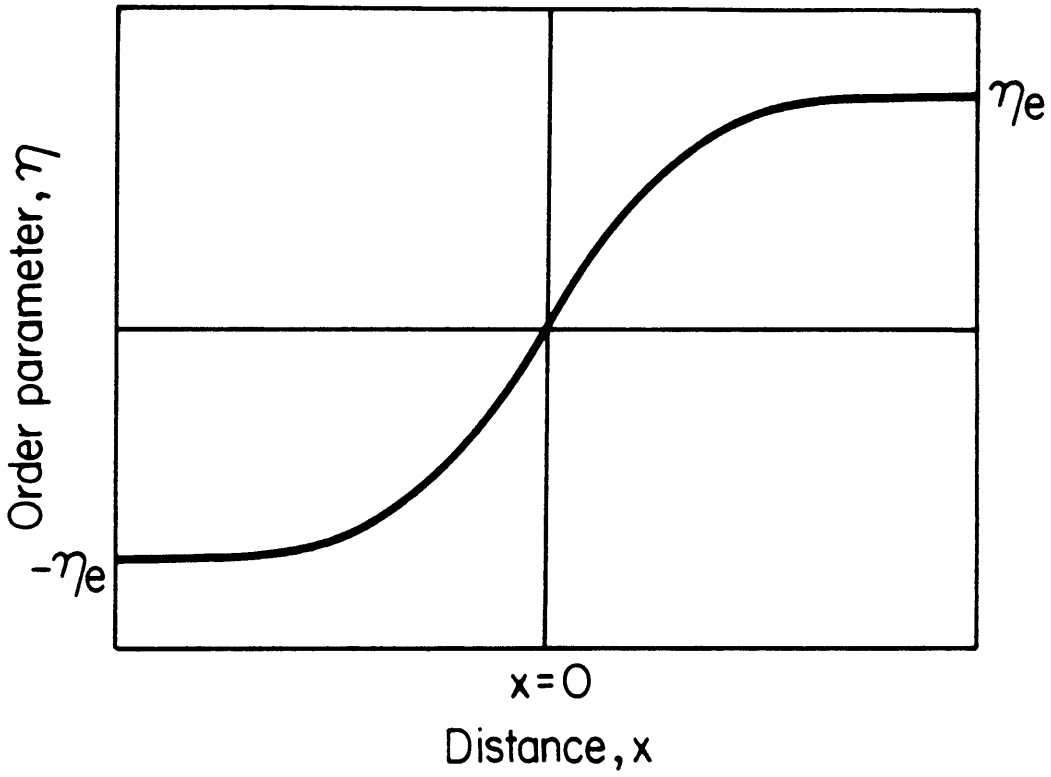

Figure (1-2) Schematic structure of an antiphase boundary at an elevated temperature which shows a gradual change of the order parameter η. From reference [20]

thickness δ_η over which $\partial\eta/\partial x$ differs appreciably from zero is easily developed from Equation (1-9), given by:

$$\delta_\eta = 2\eta_e\left[\frac{K_\eta}{(\Delta f)_{max}}\right]^{\frac{1}{2}} \tag{1-11}$$

where $(\Delta f)_{max}$ is the local maximum value of Δf which occurs at $\eta = 0$.

Allen and Cahn [18] studied the migration of APBs in ordered alloys which are formed by higher-order phase transformations. Considering the kinetics of ordering where the long-range order parameter η is not a conserved quantity, along with the free energy of a diffuse interface, the velocity expression for APBs was given by:

$$V = M(K_1 + K_2) \tag{1-12}$$

where M, the mobility, is a kinetic term with units of a diffusion coefficient and is defined as:

$$M \equiv 2\alpha K_\eta \tag{1-13}$$

where α is a positive kinetic coefficient and K_η is a positive gradient energy coefficient for ordering. In deriving Equation (1-12) no variation of composition near the APB was considered, and this equation is valid for the intrinsic migration of APBs. The significant difference between Equation (1-12) and the results of previous theories is that in Equation (1-12) the velocity is not proportional to the driving force, which would involve the interfacial free energy. Nonetheless, the dissipation of free energy by an APB migrating according to Equation (1-12) was shown to be correctly given in the form of:

$$\frac{\partial F}{\partial t} = \sigma\frac{dS}{dt} \tag{1-14}$$

which indicates that the rate of free energy decrease of the system is

equal to the rate of surface area decrease times σ.

Migration of APBs which were wetted by a second disordered phase of a different composition was studied by Krzanowski and Allen [19] in the Fe-Al system. The second phase layer wetting the APB was approximately 20nm thick and a model of the migration kinetics could be developed by considering the rate of diffusion through the layer. Modelling this layer as a spherical shell, a velocity expression was developed, and was given by:

$$V = \frac{2\tilde{D}\,\sigma(K_1 + K_2)}{F^{\alpha}_{cc}\,(c^{\alpha})\cdot(c^{\alpha} - c^{F})^2 \cdot \delta} \qquad (1\text{-}15)$$

where $\tilde{D}$ = interdiffusion coefficient

σ = interfacial free energy of one Interphase Boundary (IPB) between α layer and FeAl phase

$F^{\alpha}(c^{\alpha})$ = the second derivative of F, the bulk free energy, evaluated at c^{α}

c^{α} = atomic fraction of iron in the α phase at a planar IPB

c^{F} = atomic fraction of iron in the FeAl phase at a planar IPB

δ = thickness of the α layer

δ was time dependent and given by:

$$\frac{d\delta}{dt} = \frac{4\tilde{D}\Gamma_w}{(c^{\alpha} - c^{F})\,\bar{R}^2} \qquad (1\text{-}16)$$

where $\Gamma_w = \sigma/[F^{\alpha}_{cc}(c^{\alpha}) \cdot (c^{\alpha} - c^{F})]$ and $\bar{R}$ is the average radius of the spherical shell. However, the volume fraction of the α phase was shown in the theory to be correctly given as independent of time.

Comparison of Equation (1-12) and Equation (1-15) shows interesting effects of the variation in composition near the APB: when segregation

was absent, the velocity was not linearly related to the driving force, while the presence of the wetting layer did result in a linear velocity-driving force relationship. In addition, it was noted that the presence of the wetting α layer markedly slowed the migration kinetics and also introduced shape instabilities into the morphology.

It was stated [19] that the common phenomenon of interfacial segregation refers to a film at the interface which is at most several monolayers thick, and the theory of wetted APBs may not be directly applicable to this type of interface. However the transition from wetted APBs in the α + FeAl region to nonwetted APBs in the FeAl phase involves a segregation phenomenon similar to the more common type.

Krzanowski and Allen [20,21] studied the possibility of adsorption of Fe atoms to the APBs in single phase FeAl-ordered alloys and its effects on migration kinetics of APBs. By applying diffuse interface theory [17] and a simple thermodynamic model of the Fe-Al system, composition and order parameter profiles about APBs in the single phase FeAl region which resulted in the lowest interfacial energy were calculated for different temperatures and alloy compositions. It was found that adsorption of Fe atoms on APBs reduces the interfacial energy. Solute drag theory of Hillert and Sundman [11] was applied to study migration kinetics of this type of APB. There are two types of drag force. An extrinsic drag force arises from the presence of segregated solute, and an intrinsic drag force arises from the irreversible change in order parameter and is linear to interface velocity. For the low velocity extreme, where the extrinsic drag force is much larger than the intrinsic drag, the velocity equation was given by:

$$V = \frac{D\sigma(K_1 + K_2)}{Nk_BT\alpha_1\delta_c} \tag{1-17}$$

or

$$V = \mu\sigma(K_1 + K_2) \tag{1-18}$$

where

$$\mu = \frac{D}{Nk_BT\alpha_1\delta_c} \tag{1-19}$$

α_1 is a drag coefficient which was calculated theoretically and δ_c is the thickness of the interfacial region where substantial segregation occurs. In a subsequent experimental study of antiphase domain coarsening in Fe-24%* and Fe-25%Al alloys in the FeAl phase near the α + FeAl two phase boundary [22], Krzanowski and Allen provided some experimental verification of reduced kinetics hypothetically due to segregation of Fe atoms around APB. Coarsening of fine initial antiphase domains occurred rapidly in the early stage, and Equation (1-12) was applicable because the high curvatures of fine APBs were enough to "break away" from any possible solute drag force. As domains coarsened, transition from intrinsic migration to extrinsic migration was detected due to the reducing curvatures of the coarsening APBs. This reduced kinetics at the low velocity, low curvature regime was explained by applying Equation (1-18).

Although their derivation of solute drag effects on APBs in Fe-Al alloys was very rigorous and thorough, the results of the aforementioned study by Krzanowski and Allen [21,22] cannot be readily applicable over the wide range of composition and temperature in Fe-Al alloys. The thermodynamic model they used was successful in giving a reasonable match to the experimental phase diagram only near the phase boundary between

---

* all subsequent composition is in atomic percent.

the FeAl single phase and the α + FeAl two-phase region. Furthermore, the validity of the diffuse interface theory [17] in studying composition variation at APBs in Fe-Al system is in doubt. Positive values for gradient energy coefficients were assumed in the development of the diffuse interface theory [17]. But the thermodynamic model calculation in the Fe-Al system gives negative values for compositional gradient energy coefficients. This will be discussed in detail in the following chapter.

Currently, there is no experimental study revealing any compositional variation or impurity segregation at APBs in Fe-Al alloys. The largest compositional variation predicted in [21] is about 1% over the range of 2 nm, and there is yet no experimental tool to detect this type of compositional variation.

In this study we attempted to study migration kinetics of APBs in the Fe-Al system more directly, in terms of the velocity/curvature relationship, than conventional domain coarsening experiments which gives the change of average domain size with time. This approach has the potential of detecting the transition from intrinsic migration to extrinsic migration if there is any solute segregation effect on APB migration. An effort to improve the thermodynamic model of Fe-Al alloys was also made.

1.3 Description of Present Efforts

In describing the present efforts, shortcomings of previous works (in studying migration kinetics of APBs) will be mentioned first, and attempts to improve those problems will be briefly described.

1.3.1 Shortcomings of Domain Coarsening Experiments.

As briefly mentioned in the previous section, most experiments on migration kinetics of interfaces were in the form of the observation of interface coarsening in the bulk material containing three dimensional interfaces. Thermal APBs (in contrast to the APBs formed by dislocation movements) in Fe-Al alloys have a multiply-connected "Swiss cheese" morphology [23] in which the principal curvatures are generally of opposite sign. This makes it impossible to measure mean principal curvatures of APB from two dimensional observation. Also the measurement of the instantaneous velocity of a point on a moving interface is not possible without dynamic in-situ observation of the moving interface. Because of these difficulties in measuring instantaneous velocities and instantaneous principal curvatures, direct experimental testing of Equation (1-12) or Equation (1-18) is impossible in domain coarsening experiments in the bulk specimen.

A domain coarsening equation which relates the averages of curvature to velocity was developed [18] from equation (1-12). Assuming that the general morphological features remain unchanged during coarsening, the equation was given by:

$$[S_V(t)]^{-2} - [S_V(0)]^{-2} = 2M\phi t \qquad (1\text{-}20)$$

where $S_V(t)$ and $S_V(0)$ are surface area per unit volume at time t and at t=0 respectively, and ϕ is a morphological constant introduced by a scaling assumption, and is given by:

$$K_m^2 = \phi S_v^2 \tag{1-21}$$

where K_m^2 is the averaged square mean curvature defined by:

$$K_m^2 = \langle (K_1 + K_2)^2 \rangle = \frac{1}{S} \int (K_1 + K_2)^2 dS \tag{1-22}$$

Here, S is the total surface area of the specimen. We can derive a similar domain coarsening equation out of Equation (1-18) in the form of:

$$[S_V(t)]^{-2} - [S_V(0)]^{-2} = 2\mu\sigma\phi t \tag{1-23}$$

The best we can do with domain coarsening experiments using Equation (1-20) or Equation (1-23) is to get the combined value of $M\phi$ or $\mu\sigma\phi$ for various temperatures and average domain sizes. (The mean linear intercept domain size $\bar{D}$ is given by $\bar{D} = 2/S_V$). Because of the aforementioned complexity of the APB morphology, ϕ values have not been determined theoretically or experimentally. Thus we can not get the intrinsic mobility M or the extrinsic mobility $\mu\sigma$ directly, even though we can study the changes of the combined values of $M\phi$ or $\mu\sigma\phi$ as the average domain size changes.

1.3.2 Problems of Previous Theoretical Efforts

A good test of the validity of a thermodynamic model of an alloy system is provided by calculating a phase diagram based on that model and comparing it with the existing experimental phase diagram of the alloy system. The thermodynamic model used in studying APB structures in Fe-Al system was not able to give a good match between calculated and experimental phase diagrams over wide ranges of composition and temperature [20]. This resulted from the use of a simplified Bragg-Williams approximation [24] in computing the free energy of the system. The range of interaction was limited only up to the second nearest neighbors, and the pair-wise interaction energies were assumed to be independent of composition. The Bragg-Williams approximation was used because of its advantage in the bond counting scheme in studying inhomogeneously ordered alloys and its ability to give simple analytical expressions for the free energy of the system.

The application of diffuse interface theory to study the profiles of order parameter and composition at APBs in previous studies [20,21] is in question, because the gradient energy coefficient of composition in Fe-Al system has turned out to have a negative value in our current study.

1.3.3 Present Efforts

New experimental techniques employing in-situ hot-stage transmission electron microscopy were developed in order to study the direct relationship between the local instantaneous curvature and the velocity of moving APBs. Using in-situ hot-stage TEM, we have succeeded in observing APB migration as it occurs, and due to the two-dimensionality of the thin foil samples, measurements of the local curvatures of moving APBs were possible. Two experimental techniques which can determine the mobilities of APBs will be described in the later chapter on experiments.

Efforts to improve the thermodynamic model of the Fe-Al system while maintaining the advantage of the bond counting method of the Bragg-Williams approximation were also made. This was achieved by considering the interaction of up to third nearest neighbor atoms with composition-dependent interaction energies calculated from the experimental phase diagram.

Calculation of gradient energy coefficients from this model gives positive values for order parameter and negative values for composition. Application of the diffuse interface theory in the form as originally developed by Cahn and Hilliard in studying the profile of composition at APBs is not valid because of the basic assumption of positive gradient energy coefficients in the development of continuum description of the diffuse interface theory [17]. But the energies and order parameter profiles of APBs with no composition variation can be successfully calculated from the continuum version of the diffuse interface theory.

In order to calculate possible compositional variations at APBs, a discrete lattice formulation similar to the one used by Cook et al. [25] should be developed, but it turned out to be a major task by itself, and

it will be left out for a future project in our current study.

In the following chapter, efforts of thermodynamic modelling of the Fe-Al system will be described in detail, followed by a chapter which explains the experimental details of our study.

CHAPTER 2

THERMODYNAMIC MODEL FOR THE Fe-Al SYSTEM

Since the ordered phases FeAl (which has B2 structure) and Fe_3Al (DO_3 structure) were first discovered in Fe-rich Fe-Al alloys by Bradley and Jay [26], much effort has been put into understanding order-disorder transformations in general and the transitions in iron-aluminum alloys in particular. Various phase diagrams of the Fe-Al binary system have been proposed through experimental studies employing X-ray [27-32], electrical resistivity [33], Mössbauer spectroscopy [34-36] and direct TEM [37,38] observations as well as theoretical calculations using various statistical mechanics approaches [39-43]. Semenovskaya [44] applied Khachaturyan's concentration wave approach [45,46] of considering the interatomic long-range interactions in the statistical theory of solid solutions to calculate the Fe-Al phase diagram using data obtained from X-ray diffuse scattering experiments.

The currently accepted experimental phase diagram of Fe-rich portion of the Fe-Al binary system has been clarified by Allen and Cahn [47] who distinguished between coherent and incoherent equilibrium phase diagrams of Swann et al. [37,38] and Okamota et al. [36], respectively. The coherent phase diagram, Figure (2-1), displays some remarkable features: it has two atomic ordered phases, FeAl(B2,Pm3m) which has the CsCl structure and $Fe_3Al(DO_3,Fm3m)$ which has the BiF_3 structure, and one magnetic ordering transition from paramagnetic to ferromagnetic states. The transitions α_p(paramagnetic disordered bcc solid solution) $\rightarrow$ $FeAl_p$ (paramagnetic B2) and $FeAl_p \rightarrow Fe_3Al_p$(paramagnetic DO_3) are higher-order tran-

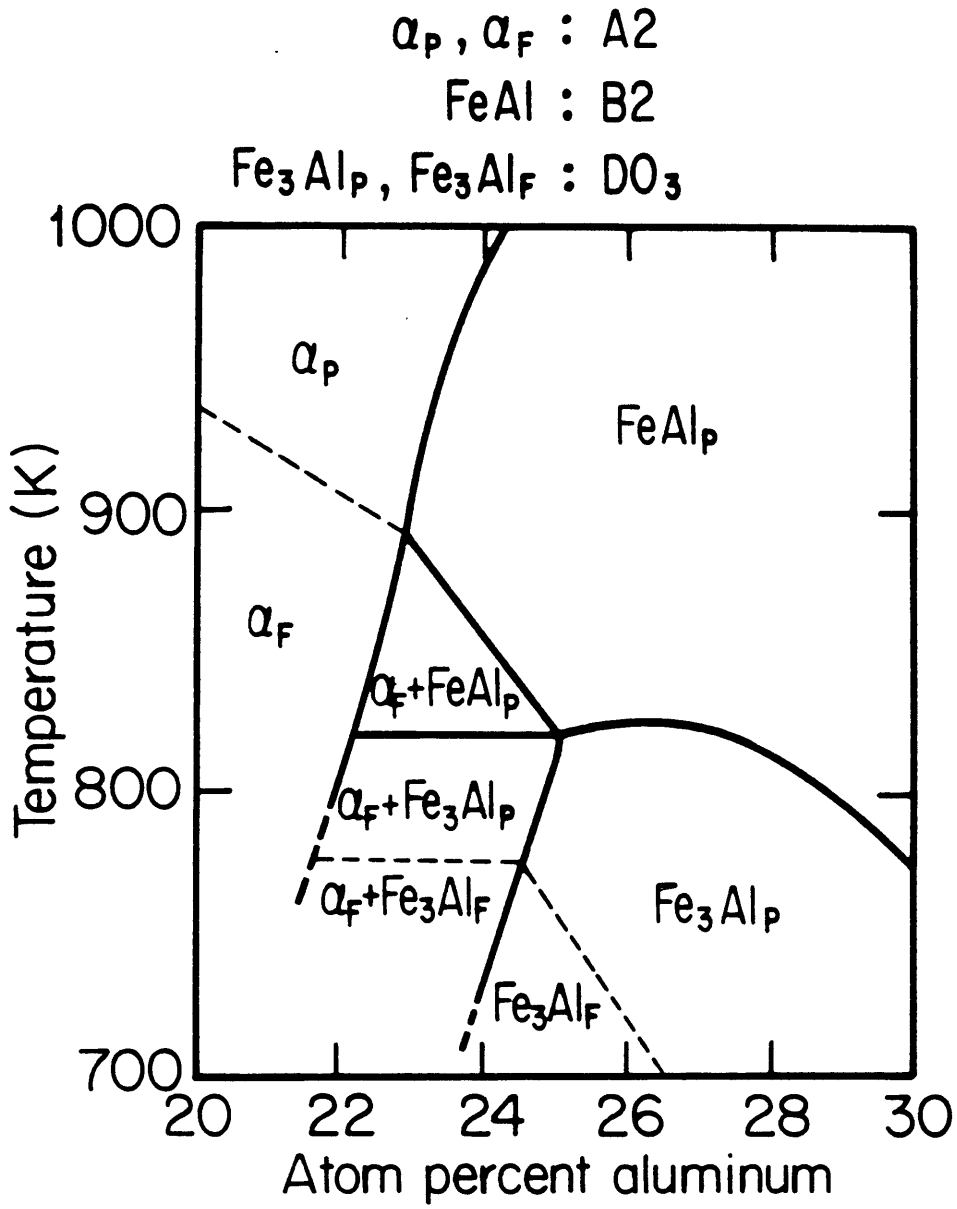

Figure (2-1) The Fe-rich portion of the Fe-Al phase diagram. From reference [38,47]

sitions (sometimes called λ-transitions), and the line of higher-order transitions for $\alpha_p \rightarrow FeAl_p$ ends at a bicritical point located at the intersection of the structural and magnetic ordering transitions located at about 900K and 23 atomic percent of Al. Below the bicritical point a miscibility gap exists where α_F and FeAlp phases coexist, and the transition is first-order.

Up to now, quantitative agreements between the experimental phase diagram of Figure (2-1) and calculated phase diagrams [39-43] have been poor. Though new approaches like computer simulation techniques and first-principles calculations look promising in calculating phase diagrams [48], the simple model of Bragg and Williams [24] has two main advantages in studying APB structures: first, the bond counting method of Bragg-Williams model lends itself nicely to computing the internal energy of inhomogeneously ordered alloys: and second, the analytical expressions for the free energy are possible in comparison with less direct methods such as Monte Carlo simulations. Before interfaces can be modelled, a good thermodynamic description of bulk phases is necessary, and the agreement of calculated phase diagram with the experimentally determined phase diagram is a good indication of the validity of the thermodynamic model of a bulk phase.

Krzanowski [20] used the Bragg-Williams model considering up to the second nearest neighbor interactions with composition-independent interaction energies in studying the APB profiles and migration kinetics in FeAl(B2) phase in Fe-24%Al and Fe-25%Al alloys. He calculated only a portion of the Fe-Al phase diagram near the bicritical point and the agreement with the experimental phase diagram was poor except at the

α_F+FeAl → FeAl phase boundary which was the main concern in his work.

In the current study, an effort has been made to improve the agreement between the calculated phase diagram from a thermodynamic model and the experimental phase diagram, while retaining the advantage of the bond counting method which is essential for getting the gradient energy coefficients needed to study APB structure and behavior.

Khachaturyan's theory [45,46] used in Semenovskaya's work [44] is very powerful because even in the long-range interaction model all the thermodynamic functions can be evaluated in the self-consistent field approximation if we know only a few energy parameters. These parameters $V(\vec{k}_s)$ are the Fourier transformations of real space pair-interaction energies, $v(\vec{r})$, and are expressed as:

$$V(\vec{k}_s) = \sum_r v(\vec{r})\exp(-i\vec{k}_s \cdot \vec{r}) \qquad (2\text{-}1)$$

where $\vec{k}_s$ is a reciprocal lattice vector and $v(\vec{r})$ is defined by:

$$v(\vec{r}) = \epsilon^r_{AA} + \epsilon^r_{BB} - 2\epsilon^r_{AB} \qquad (2\text{-}2)$$

ϵ^r_{AA}, ϵ^r_{BB}, ϵ^r_{AB} are bonding energies of A-A, B-B, and A-B bond of distance r, respectively in A-B binary alloys. The sum in Equation (2-1) is taken over all crystal lattice sites $\vec{r}$. Thus, $V(\vec{k}_s)$ contains all the interaction energies associated with the different distances between atoms.

In the Fe-Al system, the three energy parameters $V(0)$, $V(\vec{k}_1)$, $V(\vec{k}_2)$ completely determine the thermodynamics, where $\vec{k}_1 = 2\pi(\vec{a}^*_1 + \vec{a}^*_2 + \vec{a}^*_3)$, $\vec{k}_2 = \pi(\vec{a}^*_1 + \vec{a}^*_2 + \vec{a}^*_3)$ and $\vec{k} = 0$ are the (111) ($\frac{1}{2}\frac{1}{2}\frac{1}{2}$) and (000) reciprocal lattice points of the bcc solid solution respectively. $\vec{a}^*_1$, $\vec{a}^*_2$, $\vec{a}^*_3$ are the vectors of the reciprocal lattice in [100], [010], [001] directions.

Semenovskaya [44] experimentally determined these $V(\vec{k}_s)$ values from

X-ray diffuse scattering and calculated a Fe-Al phase diagram using theses values. But the later interpretation of X-Ray diffuse scattering data to get $V(\vec{k}_s)$ values [49-51] leaves doubts about the accuracy of the $V(\vec{k}_s)$ values she used to calculate the phase diagram in reference [44].

We worked along the reverse direction of Semenovskaya's approach, starting with the well established experimental phase diagram of Fe-Al [38,47] to get the energy parameters $V(\vec{k}_s)$ which can produce the phase diagram giving the best fit to the experimental one. From these $V(\vec{k}_s)$ values which are composition dependent, interaction energies up to third nearest neighbors can be calculated, and with these interaction energies, gradient energy coefficients are calculated using the bond counting scheme of the Bragg-Williams model considering up to third nearest neighbor interactions.

2.1 Calculation of $V(\vec{k}_s)$ from the Experimental Phase Diagram.

In our experimental work, our main concern was the kinetics of APB migration in FeAl(B2) phase and $Fe_3Al(DO_3)$ phase at elevated temperatures (T>740K) where the system is paramagnetic. Subsequent treatment of the thermodynamics in this chapter will be valid only in the paramagnetic region of the equilibrium phase diagram because a magnetic ordering contribution to the free energy was not included.

The free energy of the homogeneous system of the $Fe_3Al(DO_3)$ ordered Fe-Al binary alloy can be expressed [44] as:

$$\begin{aligned}\Delta F = {} & \frac{N}{2}[V(0)\ c\ (c-1) + V(\vec{k}_1)\eta_1^2 + \frac{1}{2}V(\vec{k}_2)\eta_2^2] \\ & + \frac{Nk_BT}{2}[(c-\eta_1)\ln(c-\eta_1) + (1-c+\eta_1)\ln(1-c+\eta_1)] \\ & + \frac{Nk_BT}{4}[(c+\eta_1+\eta_2)\ln(c+\eta_1+\eta_2) + (1-c-\eta_1-\eta_2)\ln(1-c-\eta_1-\eta)] \\ & + (c+\eta_1-\eta_2)\ln(c+\eta_1-\eta_2) + (1-c-\eta_1+\eta_2)\ln(1-c-\eta_1+\eta_2)]\end{aligned} \tag{2-3}$$

c is the atomic fraction of Al atoms, N is the total number of lattice sites per unit volume, T is the absolute temperature and K_B is Boltzmann's constant and η_1 and η_2 are long-range order parameters of Fe_3Al structures defined as :

$$\eta_1 = \{\frac{c^\beta + c^\gamma}{2} - c^\alpha\}/\ 2 \tag{2-4}$$

$$\eta_2 = \frac{c^\gamma - c^\beta}{2} \tag{2-5}$$

where c^α, c^β, c^γ are the atomic fraction of Al at α, β, γ sublattice

sites respectively as shown in Figure (2-2). In this sublattice designation, the site ratio of α, β, γ is 2:1:1. c^{α}, c^{β}, c^{γ} can be expressed as functions of c, η_1, and η_2 as:

$$c^{\alpha} = c-\eta_1 \tag{2-6}$$

$$c^{\beta} = c+\eta_1-\eta_2 \tag{2-7}$$

$$c^{\gamma} = c+\eta_1+\eta_2 \tag{2-8}$$

Higher-order transition lines of $\alpha_p \rightarrow FeAl_p$ and $FeAl_p \rightarrow Fe_3Al_p$ in the Fe-Al phase diagram in Figure (2-1) are the loci where equilibrium order parameters η_{1e} and η_{2e} become zero respectively. Equilibrium order parameters η_{1e} and η_{2e} can be determined from the conditions $\partial F/\partial\eta_1 = 0$ and $\partial F/\partial\eta_2 = 0$. These conditions can be reduced to a set of two transcendental equations as:

$$\eta_2 = \left[\frac{(c+\eta_1)^2(1-c+\eta_1)^2\exp\left(\frac{4\eta_1}{k_B T} V(\vec{k}_1)\right) - (c-\eta_1)^2(1-c-\eta_1)^2}{(1-c+\eta_1)^2\exp\left(\frac{4\eta_1}{k_B T} V(\vec{k}_1)\right) - (c-\eta_1)^2} \right]^{\frac{1}{2}} \tag{2-9}$$

$$\ln\left[\frac{(c+\eta_1-\eta_2)(1-c-\eta_1-\eta_1)}{(c+\eta_1+\eta_2)(1-c-\eta_1+\eta_2)}\right] = \frac{2\eta_2}{k_B T} V(\vec{k}_2) \tag{2-10}$$

A non-zero value for η_{2e} is only possible when η_{1e} has a non-zero value because η_{2e} describes the order of $Fe_3Al(DO_3)$ which can be formed only after FeAl(B2) order with η_{1e} is formed. If the energy parameters $V(\vec{k}_1)$ and $V(\vec{k}_2)$ are known, the equilibrium order parameters η_{1e} and η_{2e} can be found from Equations (2-9) and (2-10) for a given temperature and composition. On the other hand, if we know the loci of critical temperatures $T_{cr}(\alpha_p \rightarrow FeAl_p)$ where η_{1e} becomes zero, and $T_{cr}(FeAl_p \rightarrow Fe_3Al_p)$ where

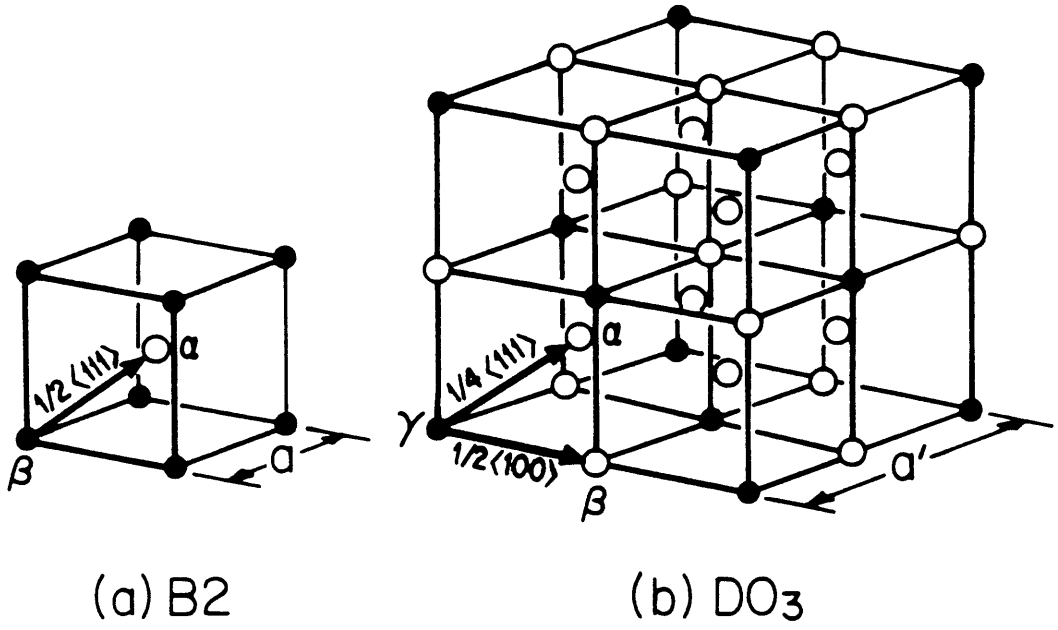

Figure (2-2) Atomic arrangements and APB diplacement vectors for B2 and DO_3 structures. The lattice paramener a' for DO_3 is twice the lattice parameter a of B2. Sublattices α, β, γ are defined as shown, giving lattice site ratios of $\alpha:\beta:\gamma$ = 2:1:1 for DO_3 structure.

η_{2e} becomes zero with non-zero η_{1e}, we can calculate the energy parameters $V(\vec{k}_1)$ and $V(\vec{k}_2)$. The loci of $T_{cr}(\alpha_p \rightarrow FeAl_p)$ is the phase boundaries between α_p and $FeAl_p$ in the phase diagram where the condition $\partial^2 F/\partial \eta_1^2 = 0$ is satisfied [52]. This condition gives:

$$T_{cr}(\alpha_p \rightarrow FeAl_p) = \frac{V(\vec{k}_1)}{k_B} c(c-1) \qquad (2\text{-}11)$$

Thus $V(\vec{k}_1)$ can be calculated from

$$V(\vec{k}_1) = \frac{k_B T_{cr}(\alpha_p \rightarrow FeAl_p)}{c(c-1)} \qquad (2\text{-}12)$$

An analytical solution for $V(\vec{k}_2)$ is not possible, but we can solve Equation (2-9) at $T_{cr}(FeAl_p \rightarrow Fe_3Al_p)$ and $\eta_{2e} = 0$ for η_{1e}. Then Equation (2-10) can be solved for $V(\vec{k}_2)$.

$T_{cr}(\alpha_p \rightarrow FeAl_p)$ and $T_{cr}(FeAl \rightarrow Fe_3Al)$ were fit numerically to parabolic curves using the existing phase diagram data from reference [38]. The experimental data points used and the fitted parabolas are presented in Figure (2-3). The resultant parabolic equations are given by:

$$T_{cr}(\alpha_p \rightarrow FeAl_p) = -2.366 \times 10^4 c^2 + 1.835 \times 10^4 (1-c) - 2.076 \times 10^3 \qquad (2\text{-}13)$$

$$T_{cr}(FeAl_p \rightarrow Fe_3Al_p) = -3.670 \times 10^4 c^2 + 1.934 \times 10^4 (1-c) - 1.725 \times 10^3 \qquad (2\text{-}14)$$

Calculated values of $V(\vec{k}_1)$ and $V(\vec{k}_2)$ are plotted in Figure (2-4) as functions of composition. $V(\vec{k}_1)$ varies substantially with composition from $-5042k_B$ at c = 0.23 to $-6368k_B$ at c = 0.35. $V(\vec{k}_2)$ remains virtually constant in the composition range of c = 0.25 to c = 0.3 at around $-3300k_B$. V(0) is not dependent on temperature and composition [44], and the value determined by Semenovskaya, $V(0) = 5800k_B$, is used in our study.

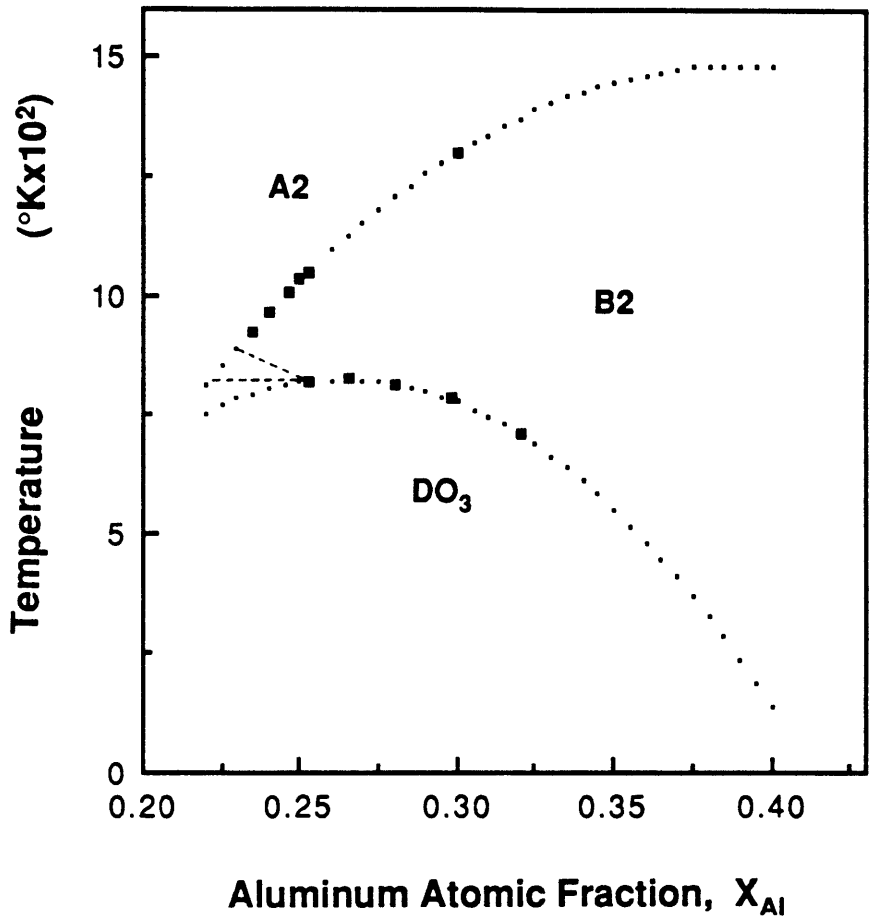

Figure (2-3) Parabolic fitting of T_{cr} (A2→B2) and T_{cr} (B2→DO_3) where A2, B2 and DO_3 are Strukturbericht notation for α, FeAl, Fe_3Al respectively. Large square dots represent experimental data from reference [38]

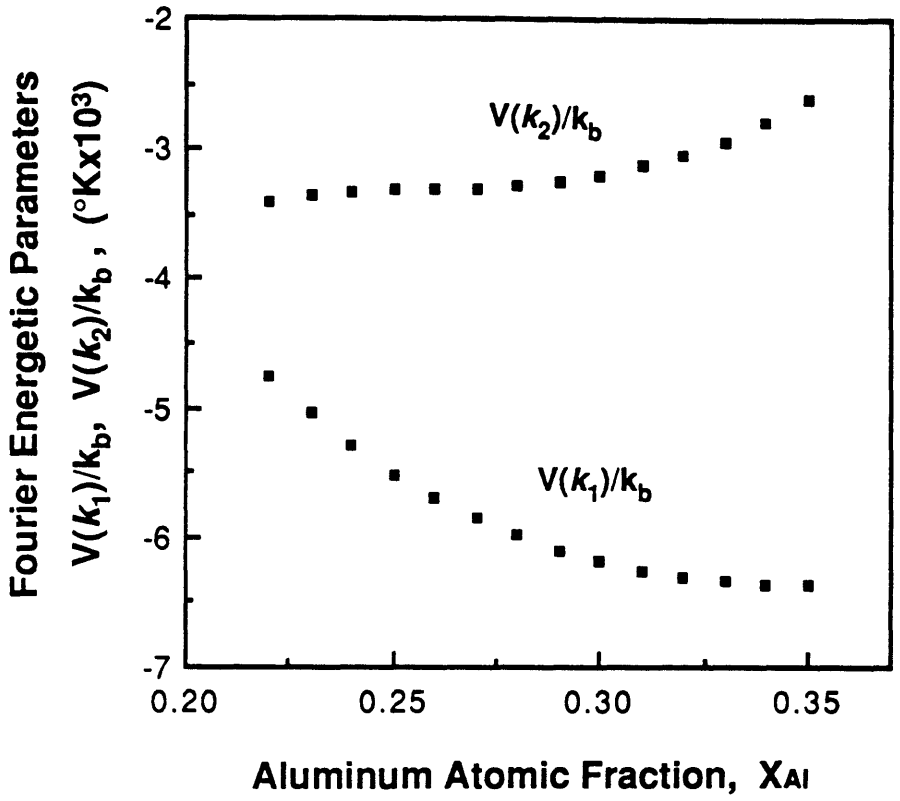

Figure (2-4) Energy parameters $V(\vec{k}_1)$ and $V(\vec{k}_2)$ calculated as functions of the composition in the Fe-Al binary system

2.2 Expressions for the Free Energy using Bragg-Williams Model.

In this section, expressions for the enthalpy and entropy for the FeAl(B2) and the $Fe_3Al(DO_3)$ structures are derived using the Bragg-Williams model considering up to third nearest neighbor interaction. These expressions will be used to calculate the gradient energy coefficients which are necessary to describe APB structures. All of the following derivations are for $Fe_3Al(DO_3)$ ordered structures. Corresponding results for FeAl(B2) can be obtained simply by replacing all η_2's with zero.

According to the definition of order parameters and sublattices in DO_3 structure in the previous section, the probability of Al and Fe atoms occupying α, β, and γ sites in a homogeneously ordered system are given by:

$$\rho_A^{\alpha} = c-\eta_1 \tag{2-15}$$

$$\rho_A^{\beta} = c+\eta_1-\eta_2 \tag{2-16}$$

$$\rho_A^{\gamma} = c+\eta_1+\eta_2 \tag{2-17}$$

$$\rho_F^{\alpha} = 1-c+\eta_1 \tag{2-18}$$

$$\rho_F^{\beta} = 1-c-\eta_1+\eta_2 \tag{2-19}$$

$$\rho_F^{\gamma} = 1-c-\eta_1-\eta_2 \tag{2-20}$$

where an Al atom is denoted by A and an Fe by F.

The probability of an Fe-Fe first nearest neighbor bond between an Fe atom in the α sublattice and an Fe atom in the β sublattice is given by:

$$\rho_F^{\alpha}\,\rho_F^{\beta} = (1-c+\eta_1)(1-c-\eta_1+\eta_2) \tag{2-21}$$

An Fe atom in the α sublattice can also form an Fe-Fe first nearest neighbor bond with an Fe atom in the γ sublattice, the probability being given by:

$$\rho_F^{\alpha}\ \rho_F^{\gamma} = (1\text{-}c+\eta_1)(1\text{-}c\text{-}\eta_1\text{-}\eta_2) \tag{2-22}$$

Multiplying the total number of bonds possible for each type of bond with the respective probabilities around an Fe atom in the α sublattice, the total probability of Fe-Fe first nearest neighbor bonds around an Fe atom in the α sublattice can be given by:

$$(P_{FF}^1)_{\alpha} = 4\rho_F^{\alpha}\ \rho_F^{\beta} + 4\rho_F^{\alpha}\ \rho_F^{\gamma} = 8(1\text{-}c)^2 - 8\eta_1^2 \tag{2-23}$$

Similarly, the total probabilities of Fe-Fe first nearest neighbor bonds around an Fe atom in the β sublattice and the γ sublattice are given respectively by:

$$(P_{FF}^1)_{\beta} = 8\rho_F^{\beta}\ \rho_F^{\alpha} = 8(1\text{-}c\text{-}\eta_1+\eta_2)(1\text{-}c+\eta_1) \tag{2-24}$$

$$(P_{FF}^1)_{\gamma} = 8\rho_F^{\gamma}\ \rho_F^{\alpha} = 8(1\text{-}c\text{-}\eta_1\text{-}\eta_2)(1\text{-}c+\eta_1) \tag{2-25}$$

The total number of Fe-Fe first nearest neighbor bonds per atomic site can be obtained by taking the average of $(P_{FF}^1)_{\alpha}$, $(P_{FF}^1)_{\beta}$ and $(P_{FF}^1)_{\gamma}$ considering the lattice site ratio of the three sublattice sites, and is given by:

$$P_{FF}^1 = \tfrac{1}{4}\{2(P_{FF}^1)_{\alpha} + (P_{FF}^1)_{\beta} + (P_{FF}^1)_{\gamma}\} = 8\{(1\text{-}c)^2 - \eta_1^2\} \tag{2-26}$$

Similarly, the total numbers of Fe-Al first nearest neighbor bonds and Al-Al first nearest neighbor bonds per atomic sites are respectively given by:

$$P^1_{FA} = 16(c-c^2+\eta_1^2) \tag{2-27}$$

$$P^1_{AA} = 8(c^2- \eta_1^2) \tag{2-28}$$

For the second nearest neighbor bonds, a similar procedure results in the following:

$$P^2_{FF} = 3\{2(1-c)^2+2\eta_1^2-\eta_2^2\} \tag{2-29}$$

$$P^2_{FA} = 6(2c-2c^2-2\eta_1^2+\eta_2^2) \tag{2-30}$$

$$P^2_{AA} = 3(2c^2+2\eta_1^2-\eta_2^2) \tag{2-31}$$

Similarly, the numbers of total third nearest neighbor bonds per atomic site are given by:

$$P^3_{FF} = 6\{2(1-c)^2+2\eta_1^2+\eta_2^2\} \tag{2-32}$$

$$P^3_{FA} = 12(2c-2c^2-2\eta_1^2-\eta_2^2) \tag{2-33}$$

$$P^3_{AA} = 6(2c^2+2\eta_1^2+\eta_2^2) \tag{2-34}$$

The enthalpy of the Fe-Al system in the $Fe_3Al(DO_3)$ ordered phase considering up to third nearest neighbors is given by:

$$H = \frac{N}{2}\sum_{i=1}^{3} (P^i_{FF}\epsilon^i_{FF} + P^i_{FA}\epsilon^i_{FA} + P^i_{AA}\epsilon^i_{AA}) \tag{2-35}$$

where N is the total number of atomic sites per unit volume and ϵ^i_{AB} is the energy of an A-B bond for the i^{th} coordination shell. The factor of ½ is included since each bond would otherwise be counted twice. The enthalpy of the pure components can be expressed as:

$$H_{pure} = \frac{N}{2}\sum_i z^i\{c\epsilon^i_{AA} + (1-c)\epsilon^i_{FF}\} \tag{2-36}$$

where z is the coordination number for the i^{th} coordination shell. The enthalpy relative to the pure components, i.e. the enthalpy of formation of a homogeneously ordered alloy, is then given by:

$$\Delta H = H - H_{pure}$$

$$= \frac{N}{2}\left[8(c^2-c-\eta_1^2)v_1+3(2c^2-2c+2\eta_1^2-\eta_2^2)v_2+ 6(2c^2-2c+2\eta_1^2+\eta_2^2)v_3\right] \tag{2-37}$$

where $v_i = \epsilon^i_{AA} + \epsilon^i_{FF} - 2\epsilon^i_{FA}$ (2-38)

The entropy terms are found by determining the number of configurational states, Ω, and the entropy is then given by $-k_B \ln\Omega$, where k_B is Boltzmann's constant. Bragg-Williams model considers entropy of mixing on each sublattice to be ideal. For the DO_3 atomic ordering in Fe_3Al, the entropy is given by:

$$\Delta S = \frac{-Nk_B}{2}\left[(c-\eta_1)\ln(c-\eta_1) + (1-c+\eta_1)\ln(1-c+\eta_1)\right.$$
$$+\frac{1}{2}\{(c+\eta_1+\eta_2)\ln(c+\eta_1+\eta_2) + (1-c-\eta_1-\eta_2)\ln(1-c-\eta_1-\eta_2)$$
$$\left. + (c+\eta_1-\eta_2)\ln(c+\eta_1-\eta_2) + (1-c-\eta_1+\eta_2)\ln(1-c-\eta_1+\eta_2)\}\right] \tag{2-39}$$

The total free energy of a homogeneously ordered system relative to that of the pure components is given by:

$$\Delta F = \Delta H - T\Delta S \tag{2-40}$$

with the application of Equations (2-37) and (2-39). The free energy calculated by Equation (2-40) is an approximation, considering up to the third nearest neighbor interactions of the free energy expressed by Equation (2-3).

The $V(\vec{k}_s)$'s, as defined in Equation (2-1), are infinite series of interaction energies v_i of Equation (2-38) which is equivalent to Equation (2-2). We can get truncated expressions for $V(\vec{k}_s)$'s including only

up to the third nearest interaction energy v_3 by substituting suitable $\vec{r}$ for atomic bonds of first, second and third nearest neighbors in Equation (2-1). These are given by:

$$V(0) = 8v_1 + 6v_2 + 12v_3 + \ldots \quad (2\text{-}41)$$

$$V(\vec{k}_1) = -8v_1 + 6v_2 + 12v_3 + \ldots \quad (2\text{-}42)$$

$$V(\vec{k}_2) = -6v_2 + 12v_3 + \ldots \quad (2\text{-}43)$$

From these equations v_i can be calculated using the $V(\vec{k}_s)$ values calculated in the previous section as :

$$v_1 = [V(0) - V(\vec{k}_1)]/16 \quad (2\text{-}44)$$

$$v_2 = [V(0) + V(\vec{k}_1) - 2V(\vec{k}_2)]/24 \quad (2\text{-}45)$$

$$v_3 = [V(0) + V(\vec{k}_1) + 2V(\vec{k}_2)]/48 \quad (2\text{-}46)$$

Values of $V(\vec{k}_s)$'s and v_i's in the composition range of interest in the Fe-Al system are shown in Table (2-1). The v_i's are also plotted in Figure (2-5).

Values of v_1 and v_2 calculated here are substantially different from previously reported values of $v_1/k_B \simeq 1050\text{~}1100K$ and $v_2/k_B \simeq 540\text{~}560K$ which were experimentally determined from phase transition temperatures considering only up to second nearest neighbor interactions [20,43,53]. These differences suggest the importance of including third nearest neighbor interactions for a successful thermodynamic model of the Fe-Al system. Reported values of v_1, v_2, and v_3, when the third nearest neighbor interaction contribution is considered, are comparable to the values we calculated [49,50]. A very different approach in the experimental determination of the interaction energies v_1 and v_2 in the Fe-Al system

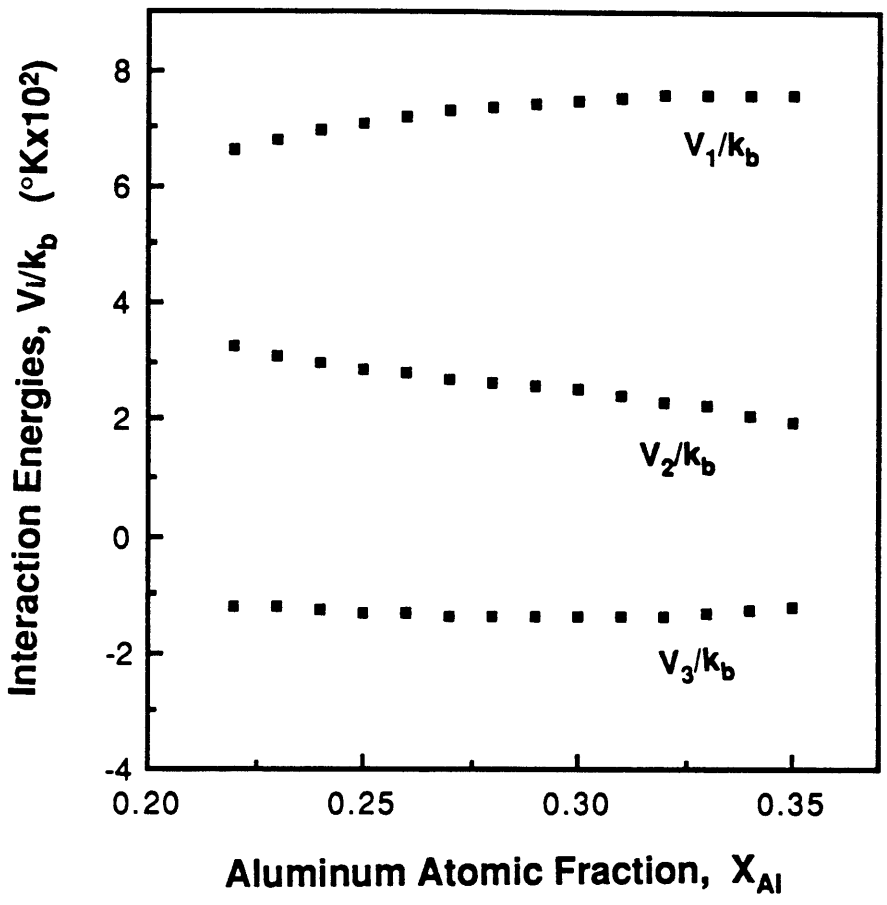

Figure (2-5) First, second, and third nearest neighbor interaction energies v_1, v_2, v_3 of the Fe-Al binary system calculated from the energy parameters $V(\vec{k}_1)$, $V(\vec{k}_2)$ and $V(0)$. v_i is defined as

$$v_i = \epsilon^i_{AA} + \epsilon^i_{FF} - 2\epsilon^i_{FA}$$

was carried out by Crawford [65]. He used the APB energies, which were determined by measuring the separation distances between superlattice dislocations [66], to calculate the interaction energies v_1 and v_2 in several alloy compositions. He found that v_1 increases and v_2 decreases as the Al content increases in the range of 25%Al to 30%Al. Both this trend and the values of v_1 and v_2 are in accord with our calculation.

The composition dependency of pairwise interaction energies v_i's calculated from a fit of the phase diagram indicates the effect of many-body interactions in real alloy systems. In our model calculation we did not consider many-body correlation effect. But the use of composition dependent pairwise interaction energies in our model would reduce errors of ignoring these correlation effects.

Table 2-1

Calculated values of $V(\vec{k}_s)$ and v_i in the Fe-Al binary system

Comp.	$V(0)k_B$	$V(\vec{k}_1)/k_B$	$V(\vec{k}_2)/k_B$	v_1/k_B	v_2/k_B	v_3/k_B
0.22	5800	-4755	-3405	659.7	327.3	-120.1
0.23	5800	-5042	-3340	677.6	309.9	-123.4
0.24	5800	-5292	-3318	693.2	297.7	-127.7
0.25	5800	-5509	-3310	706.8	288.0	-131.8
0.26	5800	-5695	-3303	718.4	279.6	-135.4
0.27	5800	-5854	-3292	728.3	272.1	-138.3
0.28	5800	-5989	-3272	736.8	264.8	-140.3
0.29	5800	-6100	-3241	743.7	257.6	-141.3
0.30	5800	-6190	-3196	749.3	250.1	-141.3
0.31	5800	-6260	-3133	753.7	244.9	-140.1
0.32	5800	-6313	-3049	757.1	232.7	-137.7
0.33	5800	-6347	-2940	759.2	222.2	-133.9
0.34	5800	-6365	-2799	760.3	209.7	-128.4
0.35	5800	-6368	-2620	760.5	194.7	-121.0

compositions are in atomic fraction of Al. k_B is Boltzmann's constant. All the units of $V(\vec{k}_s)/k_B$ and v_i/k_B are in absolute temperature K.

2.3 Expressions for the Gradient Energy Coefficients.

In this section, gradient energy coefficients for B2 ordering, DO_3 ordering, and composition were determined using Bragg-Williams approximation.

The concept of gradient energy coefficients was first introduced by Cahn and Hilliard [17] in the development of the diffuse interface theory. The free energy of the inhomogeneous system, in which the order parameters and composition can vary spatially, can be expressed as a Taylor series expansion about the free energy of a uniform system as far as the free energy is a continuous analytic function of its dependent variables at the point where the expansion is done.

Using a regular solution model, Cahn and Hilliard [17] showed that there is no contribution to the configurational entropy from a composition gradient, thus making it sufficient to consider enthalpy changes to get the free energy of the inhomogeneous system. They also argued that the free energy of a coherent interface in an unstrained cubic lattice is isotropic, and this point was supported by the calculation of APB energies in model bcc system by Kikuch and Cahn [54].

In our derivation of gradient energy coefficients, we only consider the change of the enthalpy allowing a one-dimensional variation in the composition and the order parameters along the [100] direction, effectively considering planar APBs parallel to {100} plane. Composition and order parameters in the bond probability expressions in the previous section are now functions of distance and these expressions can be Taylor expanded up to second derivatives. Corresponding equations for Equation (2-26) through Equation (2-34) are given by:

$$P^1_{FF} = 8\{(1-c)^2-\eta_1^2\} - (1-c)a^2\frac{d^2c}{dx^2} - \eta_1 a^2\frac{d^2\eta_1}{dx^2} \quad (2\text{-}47)$$

$$P^1_{FA} = 16(c-c^2+\eta_1^2) + (1-2c)a^2\frac{d^2c}{dx^2} + 2\eta_1 a^2\frac{d^2\eta_1}{dx^2} \quad (2\text{-}48)$$

$$P^1_{AA} = 8(c^2-\eta_1^2) + ca^2\frac{d^2c}{dx^2} - \eta_1 a^2\frac{d^2\eta_1}{dx^2} \quad (2\text{-}49)$$

$$P^2_{FF} = 3\{2(1-c)^2+2\eta_1^2-\eta_2^2\} - (1-c)a^2\frac{d^2c}{dx^2} + \eta_1 a^2\frac{d^2\eta_1}{dx^2} - \frac{\eta_2}{2}a^2\frac{d^2\eta_2}{dx^2} \quad (2\text{-}50)$$

$$P^2_{FA} = 6(2c-2c^2-2\eta_1^2+\eta_2^2) + (1-2c)a^2\frac{d^2c}{dx^2} - 2\eta_1 a^2\frac{d^2\eta_1}{dx^2} + \eta_2 a^2\frac{d^2\eta_2}{dx^2} \quad (2\text{-}51)$$

$$P^2_{AA} = 3(2c^2+2\eta_1^2-\eta_2^2) + ca^2\frac{d^2c}{dx^2} + \eta_1 a^2\frac{d^2\eta}{dx^2} - \frac{\eta_2}{2}a^2\frac{d^2\eta_2}{dx^2} \quad (2\text{-}52)$$

$$P^3_{FF} = 6\{2(1-c)^2+2\eta_1^2+\eta_2^2\} - 4(1-c)a^2\frac{d^2c}{dx^2} + 4\eta_1 a^2\frac{d^2\eta_1}{dx^2} + 2\eta_2 a^2\frac{d^2\eta_2}{dx^2} \quad (2\text{-}53)$$

$$P^3_{FA} = 12(2c-2c^2-2\eta_1^2-\eta_2^2\} + 4(1-2c)a^2\frac{d^2c}{dx^2} - 8\eta_1 a^2\frac{d^2\eta_1}{dx^2} - 4\eta_2 a^2\frac{d^2\eta_2}{dx^2} \quad (2\text{-}54)$$

$$P^3_{AA} = 6(2c^2+2\eta_1^2+\eta_2^2\} + 4ca^2\frac{d^2c}{dx^2} + 4\eta_1 a^2\frac{d^2\eta_1}{dx^2} + 2a^2\eta_2\frac{d^2\eta_2}{dx^2} \quad (2\text{-}55)$$

where a is the lattice constant of the alloy as denoted in Figure (2.2)(a). The composition, c, in the above equations is the average composition of the whole alloy given in the atomic fraction of Al.

The enthalpy per unit volume is expressed by:

$$h = \frac{\Delta H}{N} = \frac{1}{2}[8(c^2-c-\eta_1^2)v_1 + 3(2c^2-2c+2\eta_1^2-\eta_2^2)v_2 + 6(2c^2-2c+2\eta_1^2+\eta_2^2)v_3$$

$$+ a^2\frac{d^2c}{dx^2}\{cv_1+\epsilon^1_{FA}-\epsilon^1_{FF}+cv_2+\epsilon^2_{FA}-\epsilon^2_{FF}+4cv_3+ 4\epsilon^3_{FA}-4\epsilon^3_{FF}\ \}$$

$$+ \eta_1 a^2\frac{d^2\eta_1}{dx^2}(-v_1+v_2+4v_3) + \eta_2 a^2\frac{d^2\eta_2}{dx^2}(-\tfrac{1}{2}v_2+2v_3)] \qquad (2\text{-}56)$$

Using the enthalpy expression for the homogeneous system, Equation (2-37), Equation (2-56) can be written as:

$$h = h^\circ + K_{1c}\frac{d^2c}{dx^2} + K_{1\eta_1}\frac{d^2\eta_1}{dx^2} + K_{1\eta_2}\frac{d^2\eta_2}{dx^2} \qquad (2\text{-}57)$$

where:

$$h^\circ = \frac{\Delta H \text{ (homogeneous)}}{N}$$

$$K_{1c} = \frac{a^2}{2}(cv_1+cv_2+4cv_3+\epsilon^1_{FA}-\epsilon^1_{FF}+\epsilon^2_{FA}-\epsilon^2_{FF}+4\epsilon^3_{FA}-4\epsilon^3_{FF})$$

$$K_{1\eta_1} = \frac{a^2}{2}\eta_1(-v_1+v_2+4v_3)$$

$$K_{1\eta_2} = \frac{a}{2}\eta_2(-\tfrac{1}{2}v_2+2v_3)$$

The gradient energy coefficients for the composition, and order parameters η_1 and η_2 can be obtained following Cahn and Hilliard's definition of these coefficients [17], and are given by:

$$K_c = -\partial K_{1c}/\partial c = \frac{-a^2}{2}(v_1+ v_2+ 4v_3) \qquad (2\text{-}58)$$

$$K_{\eta_1} = -\partial K_{1\eta_1}/\partial \eta_1 = \frac{a^2}{2}(v_1- v_2- 4v_3) \qquad (2\text{-}59)$$

$$K_{\eta_2} = -\partial K_{1\eta_2}/\partial \eta_2 = \frac{a^2}{2}(v_2/2 - 2v_3) \qquad (2\text{-}60)$$

To calculate K_c accurately, we should know the compositional dependencies of the individual bond energies ϵ^i_{FA} and ϵ^i_{FF}, as well as the compositional

dependencies of the interaction energies v_1, v_2, and v_3. As an approximation, we neglect the weak composition dependencies of the interaction energies and the individual bond energies to calculate the partial differential $\partial K_{1c}/\partial c$.

Calculated values of the gradient energy coefficients are shown in Table (2-2) and also plotted in Figure (2-6).

The gradient energy coefficient for the composition is negative for all the composition range in the Fe-Al system, and this is consistent with the fact that the alloy tends to order [25]. The magnitude of K_c is of comparable order to the experimentally measured value for gold-silver alloys [55] which also displays a tendency to form ordered phases.

In this chapter we have improved the Bragg-Williams model of the Fe-Al system by considering up to third nearest neighbor interactions. Composition-dependent interaction energies have been calculated from the experimental phase diagram of the Fe-Al system. The expressions for the gradient energy coefficients K_{η_1}, K_{η_2} and K_c have been derived as functions of these interaction energies from the improved Bragg-Williams model. These gradient energy coefficients are essential in calculating APB profiles and energies. Actual calculation of APB profiles and energies using these parameters is presented in Chapter 4.

Table 2-2

Calculated values of gradient energy coefficients in the Fe-Al system.

Comp. (X_{Al})	K_c(J/m)	K_{η_1}(J/m)	K_{η_2}(J/m)
0.22	-2.42×10^{-11}	3.88×10^{-11}	1.98×10^{-11}
0.23	-2.36×10^{-11}	4.11×10^{-11}	1.92×10^{-11}
0.24	-2.29×10^{-11}	4.33×10^{-11}	1.93×10^{-11}
0.25	-2.23×10^{-11}	4.52×10^{-11}	1.95×10^{-11}
0.26	-2.18×10^{-11}	4.68×10^{-11}	1.96×10^{-11}
0.27	-2.14×10^{-11}	4.82×10^{-11}	1.97×10^{-11}
0.28	-2.10×10^{-11}	4.93×10^{-11}	1.97×10^{-11}
0.29	-2.08×10^{-11}	5.02×10^{-11}	1.96×10^{-11}
0.30	-2.07×10^{-11}	5.08×10^{-11}	1.95×10^{-11}
0.31	-2.08×10^{-11}	5.12×10^{-11}	1.92×10^{-11}
0.32	-2.10×10^{-11}	5.13×10^{-11}	1.87×10^{-11}
0.33	-2.13×10^{-11}	5.12×10^{-11}	1.81×10^{-11}
0.34	-2.18×10^{-11}	5.08×10^{-11}	1.73×10^{-11}
0.35	-2.25×10^{-11}	5.15×10^{-11}	1.62×10^{-11}

In calculating above values, the values $k_B = 1.38 \times 10^{-23}$ J/K and $a=2.90 \times 10^{-10}$ m are used.

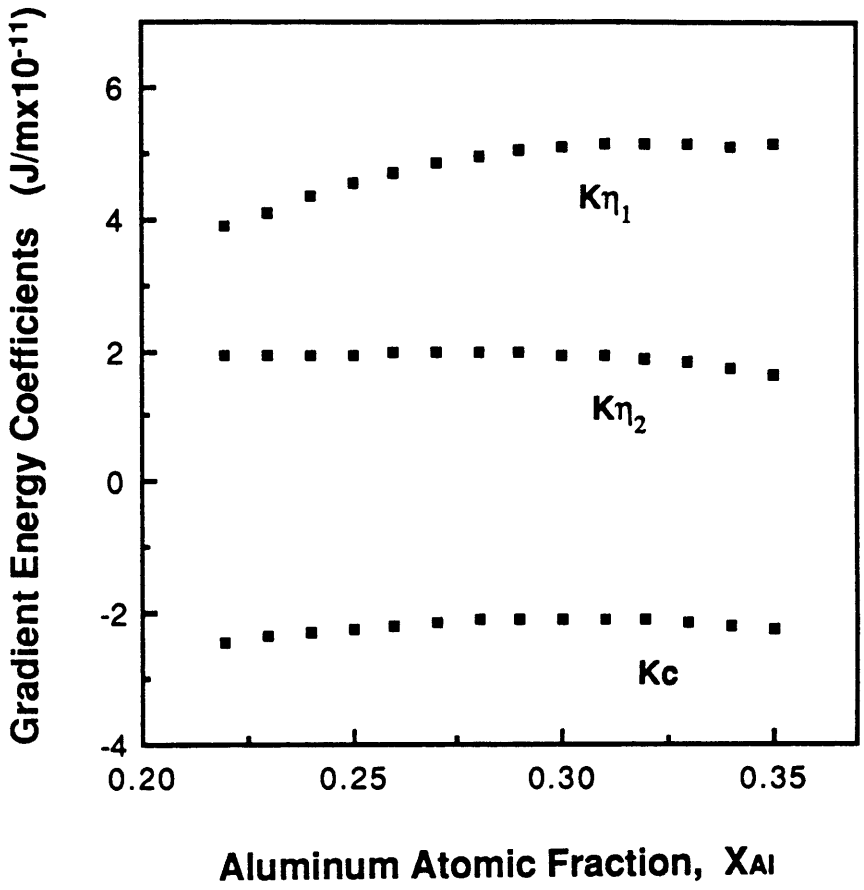

Figure (2-6) Gradient energy coefficients for composition (K_C), B2 order parameter (K_{η_1}), and DO_3 order parameter (K_{η_2}) in the Fe-Al binary system. Note the negative values for K_C.

CHAPTER 3

EXPERIMENTS

The main focus of the experimental part of this study is on the determination of the direct relationship between the velocity of migration and the local curvature of APBs, which will determine the APB mobility.

Antiphase domains in bulk specimens have a multiply interconnected morphology [23] in which the principal curvatures are generally of opposite sign. This morphological characteristic, which is true for both of the APBs in B2 and DO_3 phases in the Fe-Al system, results from the fact that there are only two possible domains which have the equivalent structures with order parameter η or $-\eta$ [56]. In B2 phases, there are only two different domains separated by the APBs having a displacement vector $\frac{1}{2}a\langle 111\rangle$ (see Figure (2-2)). The APBs in B2 will be called <111> APBs for the rest of this thesis. In the DO_3 phase, there are two different domains separated by APBs with $\frac{1}{2}a'\langle 100\rangle$ displacement vector within a much larger domain separated by <111> APBs. Although there are four possible domains altogether in DO_3 phases, only two different domains are possible within each of the large domains inherited from the B2 phase. Thus, the APBs in the DO_3 phase are composed of fine scale <100> APBs within larger scale <111> APBs. The actual sizes of <100> APBs and <111> APBs in the DO_3 phase are dependent on the specific heat treatment history of the alloy. Typical APB structures in the DO_3 phase are shown in Figure (3-1).

The antiphase domain coarsening experiments that have been used previously to investigate APB motion in bulk specimens [18, 19, 22, 57] do not allow the direct determination of APB mobilities. This is due to the extreme difficulty in measuring the principal curvatures of APBs from two-dimensional projected images such as Figure (3-1). Therefore, the use of bulk antiphase coarsening data for the determination of velocity-curvature relationships is impossible.

Using in-situ hot-stage transmission electron microscopy, we have succeeded in observing APB migration directly as it occurs. Because of the two-dimensionality of APBs in the thin foil samples (either planar APBs introduced by dislocation movements or thermal APBs aligned themselves normal to the thin foil surface during heating), measurements of the local curvatures from recorded images of moving APBs were possible. The direct relationship between the migrating velocity and the local curvature of APBs could then be determined by applying velocity equations like Equation (1-12) and Equation (1-18).

Surface pinning of moving APBs in thin foil specimens should be negligible because the energy of APBs ($\simeq$ 1 mJ/m^2, see Chapter 4 for calculated values) is much smaller than the surface energy ($\simeq$ 1 J/m^2), and virtually no surface groove will be formed at the intersection of APBs with the foil surface.

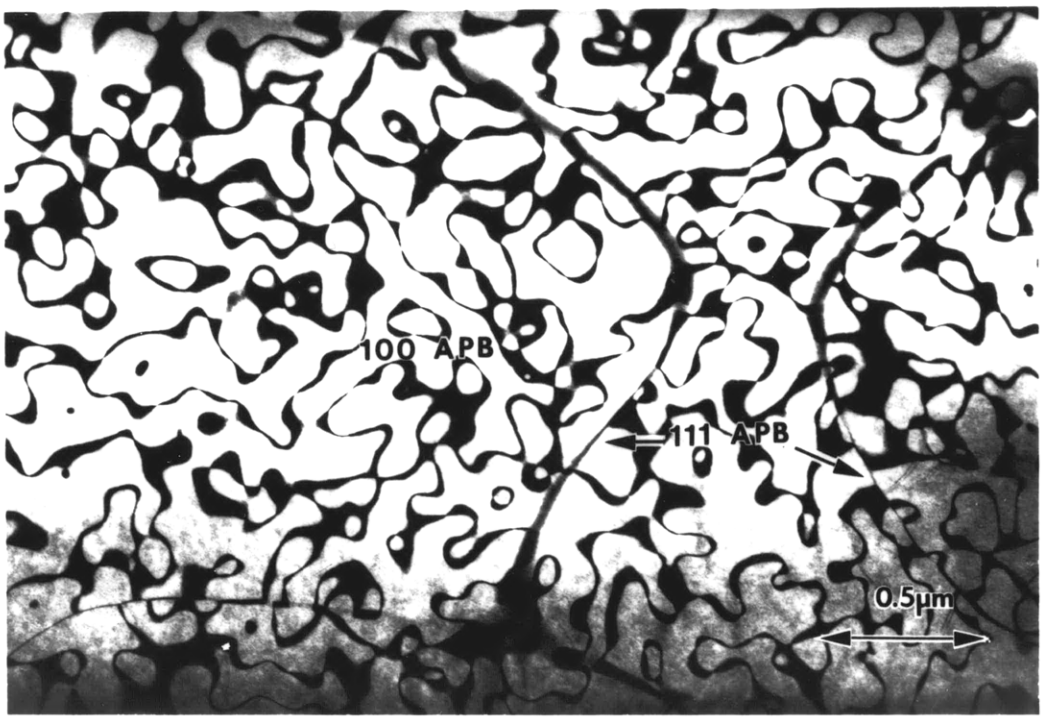

Figure (3-1) A dark-field electron micrograph showing typical structures of thermal APBs in the DO_3 phase. Fine <100> APBs are produced inside the large domains inherited from the B2 phase which are separated by much coarser <111> APBs. The speciman of Fe-26%Al was heat treated at 1474K for 1800 s and air cooled, and then reheated at 745K from 7200 s followed by water quenching.

3-1 EXPERIMENTAL PROCEDURES

3-1-1 Specimen Composition and Preparation

Nominal compositions of the alloys used were Fe-24%Al and Fe-26%Al (all compositions are in atomic percent unless otherwise stated). The Fe-24%Al alloy was prepared at the General Electric Research and Development Center. This alloy was made by vacuum melting, and the ingots were chill cast into 25 mm diameter molds. The alloy was then hot swaged to 5.0 mm diameter rods, which were later machined to 3.0 mm diameter. A chemical analysis of this material showed the following impurities to be present (in wt %): 0.01% O, 0.007% C, <0.001% N, <0.001% S, 0.0004% Mg, <0.002% Ni, 0.0003% Ti, <0.02% Si, 0.001% V, <0.0031% Zn, <0.002% Pb, <0.002% Ga, <0.005% Cr and <0.005% Cu. The Fe-26%Al alloy was obtained from the Air Force Wright Aeronautical Laboratories. This alloy was prepared by arc melting three times, followed by an isothermal forging treatment at 1173K. Out of pancake-like, as received, alloy pieces of thickness about 5mm, 3mm diameter rods were machined. A chemical analysis of the alloy showed the following impurities to be present (in wt %): 0.022% O, 0.014% C, <0.001% N, <0.001% S and "very small amounts" (<0.001%) of metallic impurities like Mn, Ni, Si, Ca and Cu.

The Fe-26%Al alloy has the transition temperatures [38] of $T_c(A2 \rightarrow B2)$ = 1096K and $T_c(B2 \rightarrow DO_3)$ = 826K. The Fe-24%Al alloy has the transition temperatures of $T_c(A2 \rightarrow B2)$ = 965K, $T(B2 \rightarrow A2+B2)$ = 858K, $T(A2+B2 \rightarrow A2+DO_3)$ = 820K, and $T(A2+DO_3 \rightarrow DO_3)$ = 730K.

3.1.2 Isothermal Antiphase Domain Coarsening

Even though a conventional antiphase domain coarsening experiment does not allow to study direct relation between the velocity and the curvature of migrating APBs, it has its own merit in studying the migration kinetics. Unlike in-situ experiments, very slow kinetics can be detected rather easily because we can heat a bulk specimen at a constant temperature for a long time without any problem in an inert atmosphere or in a salt bath. Therefore we can detect the transition from the high velocity regime to the low velocity regime of the migration kinetics from a bulk domain coarsening experiment. By comparing the corresponding results of bulk domain coarsening experiments with those of in-situ experiments, we can also determine the value of the morphological constant ϕ in Equation (1-20). For these reasons we have done the following domain coarsening experiments.

A three millimeter diameter rod was machined from the Fe-26%Al alloy, homogenized for 7200 s at 1373K and subsequently air-cooled. Discs 0.2 mm thick for isothermal antiphase domain coarsening heat treatments were cut from this rod by electro-discharge machining. These discs were then wrapped in nickel wire meshes, and heat treated in a molten salt bath at the desired temperatures for various time followed by a water quench. The accuracy of the temperature of the salt bath was ±2K, and the stability of the temperature of the salt bath during heat treatment was ±2K. Following the heat treatments, specimens were carefully ground on both sides of the discs using up to #600 emery papers until a thickness of 0.08 - 0.1 mm was obtained. The specimens were then electropolished in a solution of 1 part nitric acid (HNO_3) and 2 parts methanol (CH_3OH) in

-40°≃-45°C at a voltage of 10≃12 V, using a twin-jet apparatus.

Transmission electron microscopy observations of the specimens were made employing superlattice dark field imaging as described by Marcinkowski and Brown [58]. A JEOL 200-CX TEM with a double tilt holder was used at 200 kV accelerating voltage. The optimum imaging condition for observing <100> APBs in DO_3 ordered alloys can be achieved by tilting the specimen for strong diffraction of <111> superlattice reflections near a (011) pole or a (112) pole along 222 Kikuchi lines. The effective extinction distance for a <111> superlattice reflection is in the order of 200 nm for small deviations from the exact Bragg condition which we used [58]. The brightest dark-field images are formed when the specimen thickness is a half of the effective extinction distance. The average thickness of the sample we observed could be estimated to be around 100 nm because we observed the first bright area from the edge of the sample. Fringe patterns which are common in stacking fault images are not expected in APB images in Fe-Al alloys because of the large effective extinction distances of the superlattice reflections. Figure (3-1) shows no fringe patterns in APB images as expected.

Measurements of S_V (the APB area per unit volume, which is related to the mean linear intercept domain size, D, by $S_V = \frac{2}{D}$) from dark field electron micrographs of APBs were made by counting the number of APB intercepts with a test circle of known length. The value of S_V was obtained by dividing twice the total number of intercepts by the total line length of the circle [59]. A correction factor for the error introduced by tilting the specimen with respect to the beam direction of the electron microscope was applied to the line length for each application

of the test circle. More detailed descriptions of the S_v measurements can be found elsewhere [20].

3.1.3 In-situ Hot-Stage Experiments

In-situ hot-stage experiments were carried out using a double-tilt heating holder (Model EM-SHTH) in a JEOL-200CX electron microscope operating at 200 kV. The heating holder can heat a thin foil sample up to 1073K with a electric resistance heating coil. It has a specimen tilting capacity of ±45° X-tilt and ±10° Y-tilt. Even though quicker heating might be possible, it requires at least 30 or 40 minutes wait to make the specimen stable enough for photography. The temperature reading of the heating holder is given by the voltage reading of a W-5%Re/W-26%Re thermocouple embedded in the holder. In order to know the real temperature of the sample being observed, a temperature calibration is needed.

(a) Temperature Calibration

The temperature reading of the heating holder requires calibration, because the indicated temperature is the temperature of the rim of a specimen disc, where the heating coil and the thermocouple are in thermal contact with the specimen. Most of the observations are made around the edge of a hole in the center of the specimen disc. The actual temperature of the observed area can differ from the indicated temperature, due to the temperature gradients which will vary from material to material. Thus the use of the same kind of the specimens (in the sense of thermal contact to specimen holder and thermal conductivity of the specimen) for temperature calibration is desirable.

For the calibration we have used the invariant transformation α_F + $FeAl_p$ = α_F + Fe_3Al_p in the Fe-Al binary system (see Figure 2-1) which has been determined to occur at 820K in coherent phase transformation [38].

If we consider the unit cell of the DO_3 structure with lattice parameter a′ which is composed of 8 unit cells of the bcc lattice containing 16 atomic sites (see Figure 2-2), fundamental Bragg diffraction of the A2 structure occurs for h + k + l = 4n where n is an integer. B2 superlattice diffraction occurs for h + k + l = 4n + 2. The DO_3 diffraction occurs for h, k, l unmixed. When h, k, l are even, the diffraction coincides with either fundamental or B2 diffraction. When h, k, l are all odd, the diffraction belongs to DO_3 alone. By observing the change of the diffraction pattern in either the (011) or (112) pole with the change of the ordered structure, we can calibrate the exact transformation temperature for $\alpha_F + FeAl_p = \alpha_F + Fe_3Al_p$ in Fe-24%Al specimens. Figure (3-2) shows the change of diffraction patterns of (011) pole with temperature.

We also tried to use the melting points of tin (Sn) and aluminum for temperature calibration using thin film deposits of these metals on copper grids. But due to the aforementioned difference in thermal conductivity and specimen configuration, these calibration are not valid for our experiments. Having only one reliable point for calibration, linear calibration elsewhere is assumed. The calibrated temperature is estimated to be correct to within an error of ±5K. This error range is due to the difficulty of detecting very weak superlattice reflection spots in the diffraction pattern like Figure (3-2) when the temperature is within 5K of the invariant transition temperature.

(b) Separation of Planar Intersecting APBs

By deforming ordered Fe-Al alloys on multiple slip systems of {110}

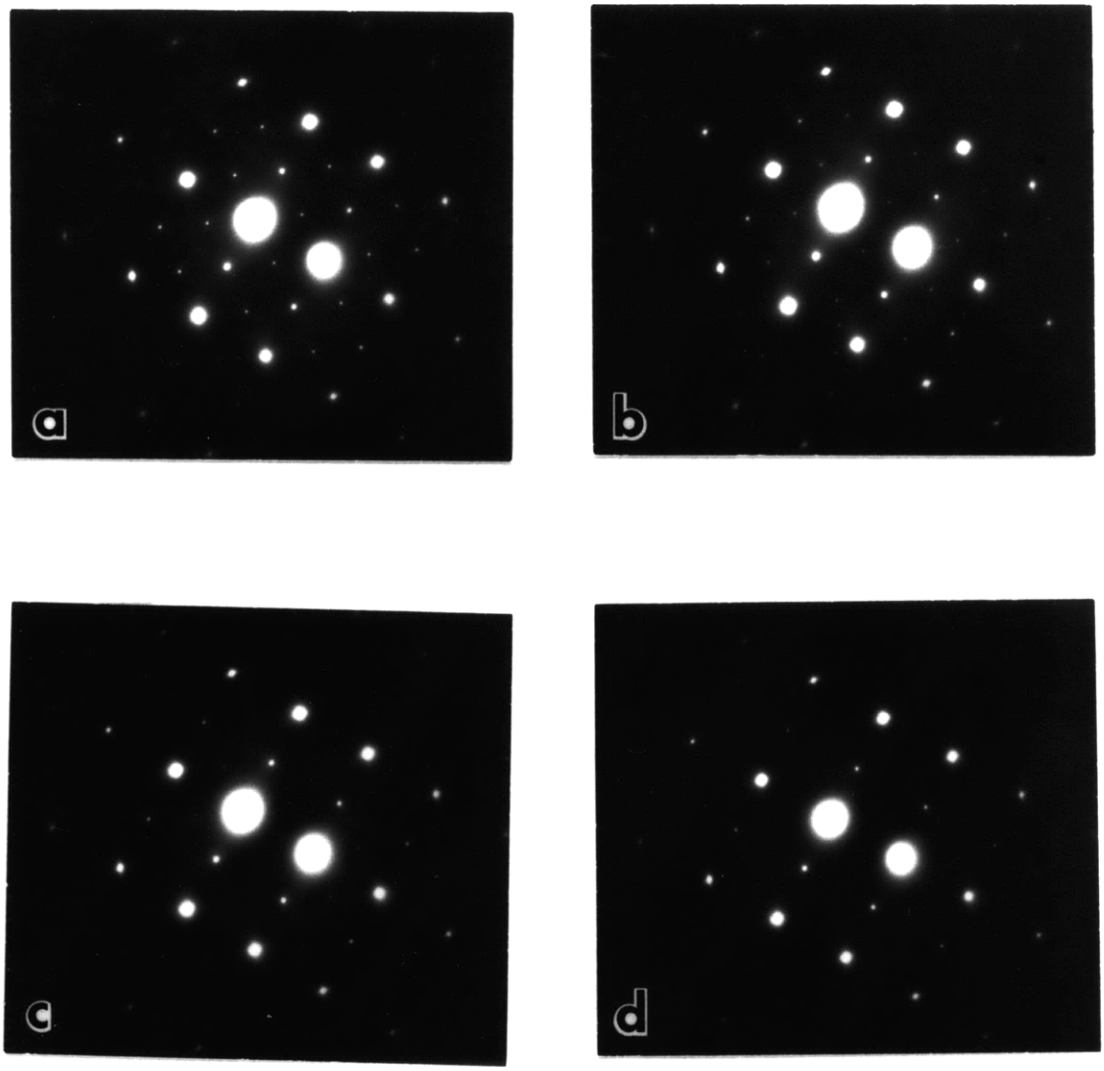

Figure (3-2) Changes in the diffraction pattern at (011) pole in the Fe-24%Al alloy with the temperature change (a) T=780K, (b) T=798K, (c) T=810K, (d) T=820K. As the temperature increases, superlattice reflection spots from the DO_3 phase become weaker and disappear at the invariant transition temperature of 820K. Temperatures given above are calibrated temperatures.

<111> type, we have been able to create planar APBs on the slip planes by the movement of dislocations that have numerous places of intersection with each other. The intersections of these planar APBs are unstable, and subsequent heat treatments allow the boundaries to pull apart into a hyperbolic sheet-like morphology having only one non-zero principal curvature [83]. This is schematically represented in Figure (3.3).

Planar APBs produced by deformation will not have any segregation initially, even though the thermal APBs in the same specimen may have some segregation. And at the early stage of separation, the curvature at the tip of the hyperbola is infinitely large, producing a driving force large enough to break away from any solute-drag. These two facts assure that the mobility determined from the separation of these intersections is intrinsic.

Sun and Bauer[60] analyzed the motion of hyperbolic interfaces by applying Mullins' theory [61] of the two-dimensional motion of idealized grain boundaries. Using the intrinsic velocity equation (Equation (1-12) $V = M(K_1 + K_2)$), the motion of hyperbolic APBs is described by:

$$R(t) = \{2Mf(\alpha)t\}^{\frac{1}{2}} \qquad (3\text{-}1)$$

where R is the distance of migration from the initial point of intersection at time t (see Figure (3-3) (c)), and $f(\alpha)$ is the magnifying function where α is one-half the angle between the asymptotes of the hyperbola. $f(\alpha)$ cannot be expressed analytically. Sun and Bauer used a finite-difference analysis to generate the curve for $f(\alpha)$ versus α shown in Figure (3-4). In the case of $f(\alpha) = 1$, the curvature at the tip of

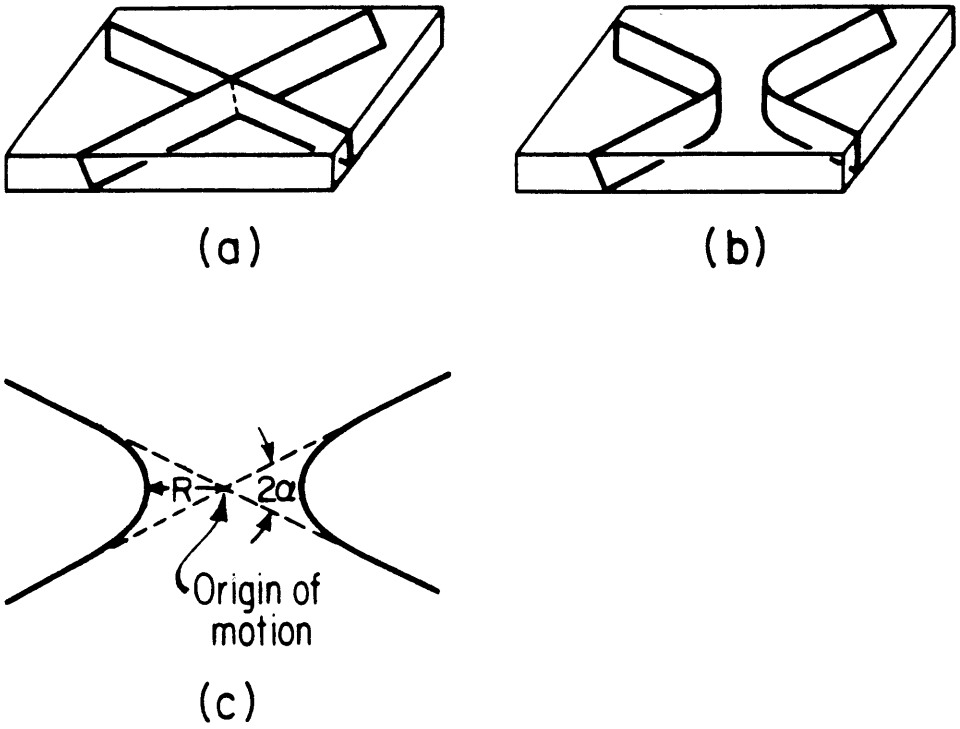

Figure (3-3) Schematic diagram of a thin foil sample which has an intersection of two planar APBs produced by deformation. (a) Before any separation, (b) separated intersection after some heating, (c) schematic view of (b) along the direction of intersection.

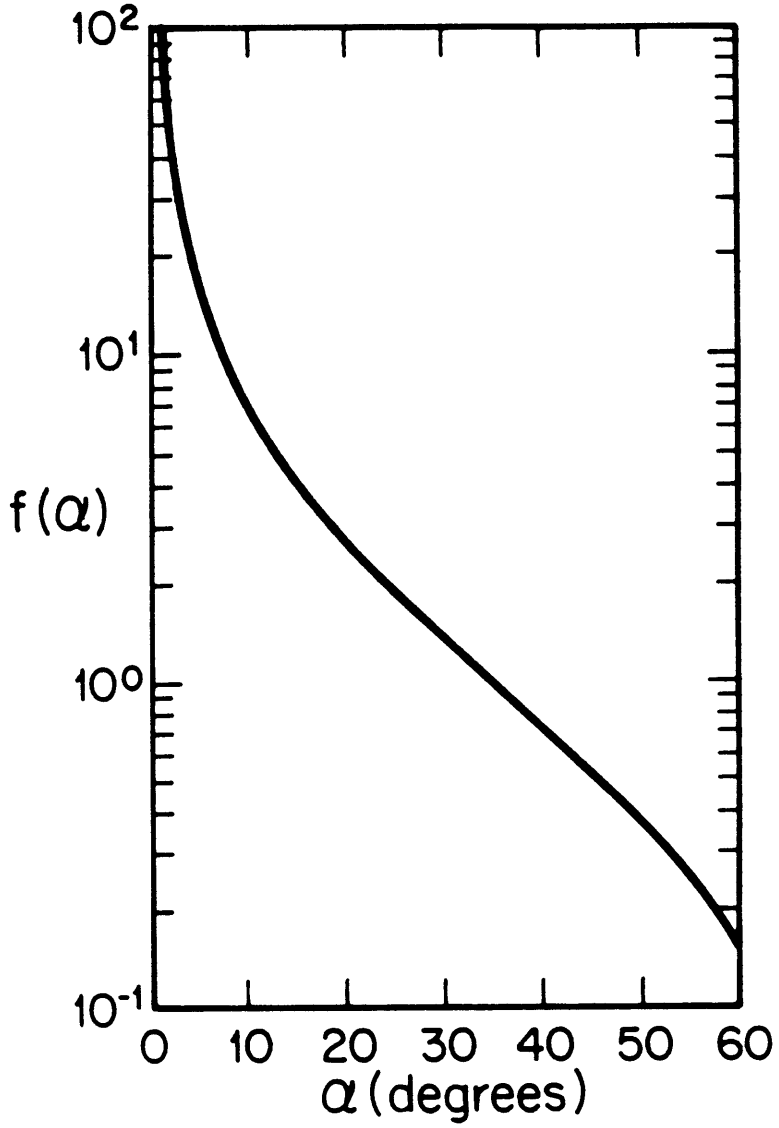

Figure (3-4) Variation of the magnifacation factor $f(\alpha)$ with angle α. From reference [60]

the hyperbola is exactly the same as the curvature of a circle of radius R. As α reduces, $f(\alpha)$ increases rapidly giving increasingly higher curvature at the hyperbolic tip.

By observing R vs. t at a constant temperature, the intrinsic mobility M can be determined using Equation (3-1). For a correct stereological analysis of data from this type of experiment, it is essential to get several sets of dark-field micrographs of the same area from various beam directions, along with the relevant diffraction patterns which show Kikuchi lines for accurate beam direction determination. A diffraction pattern of the sample with all the tilts zeroed should also be taken to determine the foil's surface normal. Slip systems forming the intersection can be determined from the above data by trace analysis, and the real values of α and R can be calculated from the projected image using the geometrical relationship between image projection and slip systems. It is helpful to do all the stereological analysis described above before heating. Knowing the direction of intersection, the beam direction which gives the closest edge-on projections can be chosen to reduce the experimental error related to separation distance measurement.

Fe-24%Al alloy rod of 3 mm diameter was annealed at 1223K for 9000 s and then held at 700K for 5×10^5 s and quenched. The resultant microstructure consisted of <100> thermal APBs of the DO_3 structure with the average domain size of 0.3 μm. The rod was cut to 6 mm length and was compressed to a total plastic strain of 1.0% at 433K in an oil bath to encourage smooth slip deformation. Thin foil TEM specimens were prepared from this material according to the process described in section 3.1.2. Thin foil specimens were heated to 700K while being observed in TEM.

A detailed description of trace analysis and true separation distance calculations from measured R can be found in Appendix A.

(c) Two-dimensional Coarsening of Thermal APBs

When a thin foil specimen, made out of a bulk specimen which contains thermal APBs, is heated in a hot-stage specimen holder, two different types of adjustments are observed to occur. APBs inclined with respect to the foil surface rotate rapidly into orientations such that the APBs meet the foil surface at 90°. This rotation occurs more rapidly where the foil is thinner. This is shown in Figure (3-5) where the APBs near the edge of a hole in the thin foil sample are aligned normal to the foil surface while the APBs in the thicker area still have three-dimensional morphology.

Coarsening of antiphase domain structures occurs continuously, but this process is slower than the rotation of APBs normal to the foil surface. And, after a while, a two dimensional approximation, which considers the curvature of APBs as viewed normal to the foil surface as the only non-zero principal curvature, becomes valid. By measuring the local curvatures and migration distances from a series of micrographs taken at a constant temperature, the proportionality constant relating velocity to curvature can be calculated.

Fe-26%Al alloy rods of 3 mm diameter were quenched after being held for 1800 s at 1373K. Discs of 0.2 mm thickness were cut from these rods and underwent subsequent isothermal heat treatments in the salt bath to give various starting domain size of <100> APBs and <111> APBs. Thin foil samples were prepared according to the procedures described in

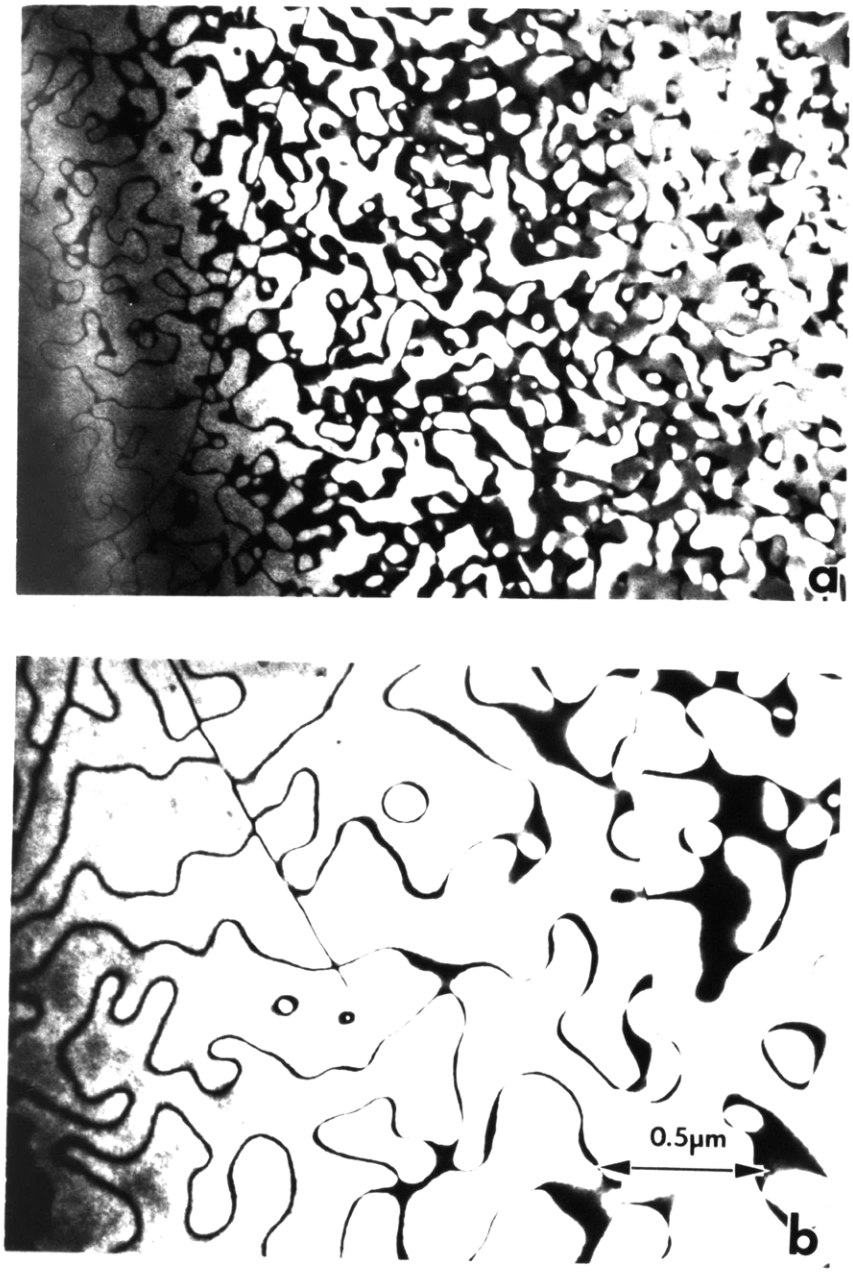

Figure (3-5) APBs near the edge of thin foil TEM samples where the foil thickness is smaller (the left hand side of the micrographs) aligned faster to establish two-dimensionality regardless of initial domain sizes.

section 3.1.2. These samples were observed in TEM using superlattice dark field imaging at various temperatures ranging from 745K to 910K, micrographs being taken at various time intervals to record sequential changes in the two-dimensional domain structures.

Measurements of the local curvatures and migration distances were carried out using a Magiscan II image analyzer from the series of micrographs taken for the same area of a specimen. Migration distances were measured relative to a fixed point on the image, generally a small high-contrast spot of contamination on the specimen. A standard software program supplied with Magiscan II was used to measure the distance between the two points selected with a light pen on the CRT screen image. Local curvatures were determined by measuring the radii of circles which are osculated to the APBs at the points where the local curvatures are intended to be measured. For this purpose, a software program, developed at the image analyzing laboratory in the Center for Materials Science and Engineering at M. I. T., was used which gives the diameter of a circle going through three points selected on the digitized image using a light pen. In measuring the curvatures and the distances, numerous independent tries were made to enter the points for measurement using a light pen. After entering each set of the points, the program displays a circle going through three selected points with its diameter or a straight line between two points with its length. We can accept or discard each set of points after reviewing the circle or the line it produces. Only the data points with gave reasonable osculating circles and measuring points on the digitized image were selected in calculating average values.

One source of errors in measurement of curvatures and migration dis-

tances is image projection when the foil normal is tilted with respect to the electron beam. These errors should not exceed 6% unless the tilt angle exceeds 20 degrees. Detailed analysis of errors involved in specimen tilting can be found in Appendix B. In the cases of larger tilt angles, interface locations which move normal to the tilting axis should be used for measurements because the deviation of the measured distances and curvatures from the real values tend to cancel each other in computing the mobility. In the case of circular APBs, deviation of distances and curvatures exactly cancel each other to give a correct mobility value when all the measurements are carried out along the direction normal to the tilting axis on the image plane (see Appendix B).

In actual experiments, the thin foil specimens which could be observed in superlattice dark field imaging with less than 10 degrees of total tilt were chosen for in-situ hot-stage experiments. Thus the possible errors from tilting were comparable to the error range of actual measurements of migrating distances and curvatures.

From the measurements of migration distances with time, migration velocity can be calculated for local features of APBs with measured instantaneous local curvatures. From the velocity equation (Equation (1-12) or Equation (1-18)), the mobilities can be determined as functions of the temperature and the local curvature.

3-2 Experimental Results

3-2-1. Isothermal Antiphase Domain Coarsening in Bulk Specimens.

The starting microstructure obtained from the heat treatment described in section 3.1.2 revealed very fine <100> APBs with $S_V \geq 3x10^7$ m^{-1} within large domains of <111> APBs with $S_V < 1x10^6$ m^{-1}.

The kinetics of domain coarsening of <100> APBs in DO_3 phase in Fe-26%Al alloys were studied at temperatures of 745K and 778K which are in DO_3 phase. Figure (3-6) shows the domain size changes with time. The measured values of S_V vs. time for these temperatures at various times are listed in Table (3-1). Measurements of S_V are made by counting the number of APB intersections with a test circle of known length on the micrographs. The size of the test circle was determined to have more than six intersections for the coarsest domains in our experiment according to the suggestion in reference [62]. The accuracy of the value of S_V determined by this method depends on the total number of intercepts counted [62]. Sufficient number of intersections were counted for the determination of each S_V value so that the standard deviation σ for each S_V is about less than 15%.

The plots of S_V^{-2} vs. time for isothermal coarsening at 745K and 778K are shown in Figure (3-7) (a) and (b) respectively. Equation (1-20) predicts that the plots should be linear if M is constant. But the plots suggest that there is a transition from rapid domain coarsening at small domain sizes (high driving force regime) to slower kinetics at larger domain sizes (low driving force regime). These results are similar to Krzanowski's results for coarsening of <111> domains in a B2 ordered Fe-

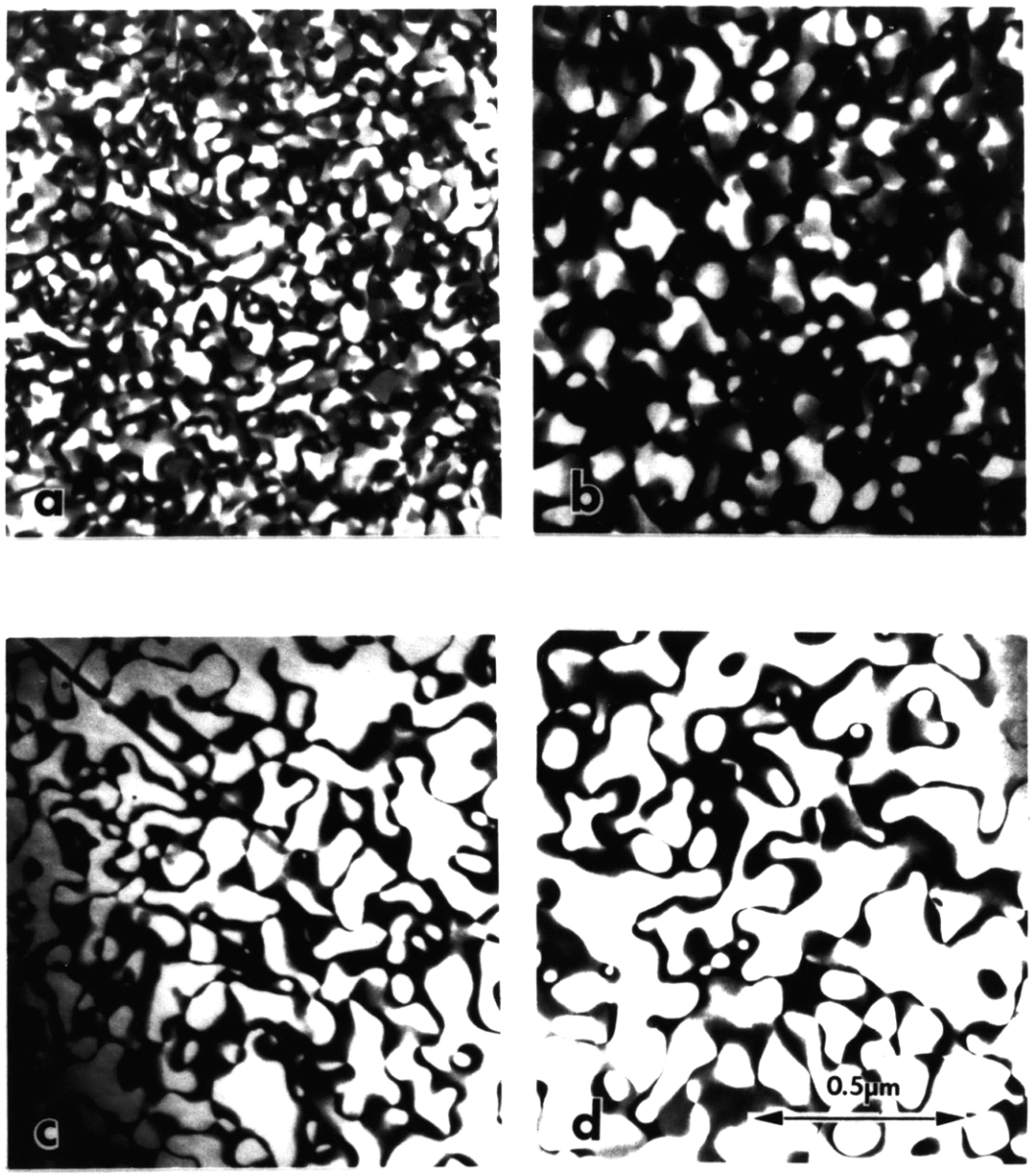

Figure (3-6) Series of dark field electron micrographs in the same magnification showing the average domain size change as thermal <100> APBs are coarsened in bulk specimens at 745K after water quenched from 1474K. Fe-26%Al alloy (a) after 300 s, (b) after 1200 s, (c) after 3600 s, (d) after 14400 s

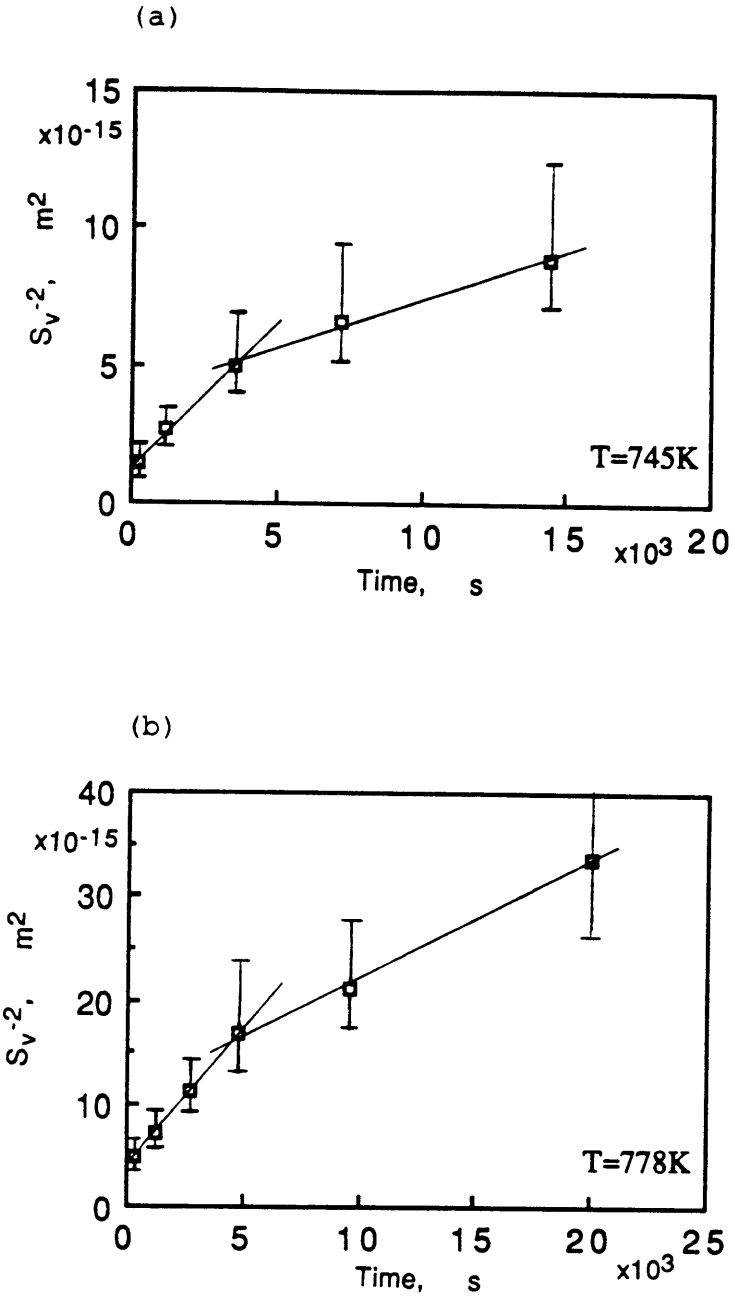

Figure (3-7) Bulk domain coarsening kinetics observed in DO_3 ordered specimens of the Fe-26%Al alloy at (a) 745K and (b) 778K.

Table 3-1

Experimental Data for Antiphase Domain Coarsening

in Fe-26%Al Alloys

	time (s)	$S_V(m^{-1})$	$\sigma(S_V)(m^{-1})$	σ(in %)
T=745K	0	3.02×10^7	2.7×10^6	9%
	300	2.63×10^7	4.3×10^6	16%
	1200	1.95×10^7	1.8×10^6	9%
	3600	1.42×10^7	2.0×10^6	14%
	7200	1.23×10^7	1.7×10^6	14%
	14400	1.06×10^7	1.7×10^6	16%
T=778K	0	3.02×10^7	2.7×10^6	9%
	300	1.44×10^7	1.7×10^6	12%
	1225	1.19×10^7	1.4×10^6	12%
	2700	9.46×10^6	1.1×10^6	12%
	4800	7.09×10^6	1.1×10^6	14%
	9605	6.89×10^6	7.5×10^5	11%
	20015	5.45×10^6	8.7×10^5	16%

σ=standard deviation

24%Al alloy [22]. The slopes of the linear portions of the plots in Figure (3-7) (a) and Figure (3-7) (b) give values for $2M\phi$, as seen by Equation (1-20). These values are presented in Table 3-2.

Table 3-2

Observed Values of $2M\phi$ in High and Low Driving-Force Regime of Migration of Antiphase Domains in an Fe-26%Al Alloy.

Temperature, K	$2M\phi$, m^2/s	
	High Driving Force	Low Driving Force
745	1.0×10^{-18}	3.6×10^{-19}
778	2.7×10^{-18}	1.1×10^{-18}

The error bars in Figure (3-7) become larger as domain coarsens because we plotted S_V^{-2} values, even though the relative standard deviations of S_V are independent of domain sizes. Thus the accuracy of $2M\phi$ values for low driving force regime should be lower than that for high driving force regime.

3-2-2 Separation of Planar Intersecting APBs

Figure (3-8) shows the separation of planar intersecting APBs in an Fe-24%Al alloy at 700K. By applying trace analysis and projected width computation as described in Appendix A, the intersecting planes were identified as $(\bar{1}01)$ and $(\bar{1}10)$. The surface normal of the foil was determined as $\hat{S}$ = (0.026, 0.455, 0.890). Considering the deformation geometry with the aid of stereographic projection, two slip systems were identified as $(\bar{1}01)[111]$ and $(\bar{1}10)[111]$, respectively. The angle between two slip planes, 2α, was 60° and the magnifying function $f(\alpha)$ has a value of 1.4 from Figure (3-4).

The thin foil specimen containing as-deformed planar intersecting APBs of Figure (3-8) (a) was heated quickly up to 700K. Figure (3-8) (b) was taken just after the calibrated temperature reading reached 700K. The time interval between Figure (3-8) (a) and Figure (3-8) (b) was about 1200 s. Because of the quick heating, the image of the specimen was not stable during heating and Figure (3-8) (b) was not sharp. Thus the separation at the intersections in Figure (3-8) (b) was not clear and it was assumed that the separation at this stage would be minimal. The real temperature of the observed specimen at the time when Figure (3-8) (b) was taken might be lower than 700K because the steady state of temperature distribution would not be established at that point. The temperature calibration experiments as described in section 3.1.3 suggested that it would take more than 1800 s to establish the steady state near 820K.

The mobility M was calculated from Equation (3-1) using the true separation distance calculated from the measured separation distance on the micrographs. The mobility M for <100> APBs in the Fe-24%Al alloy at

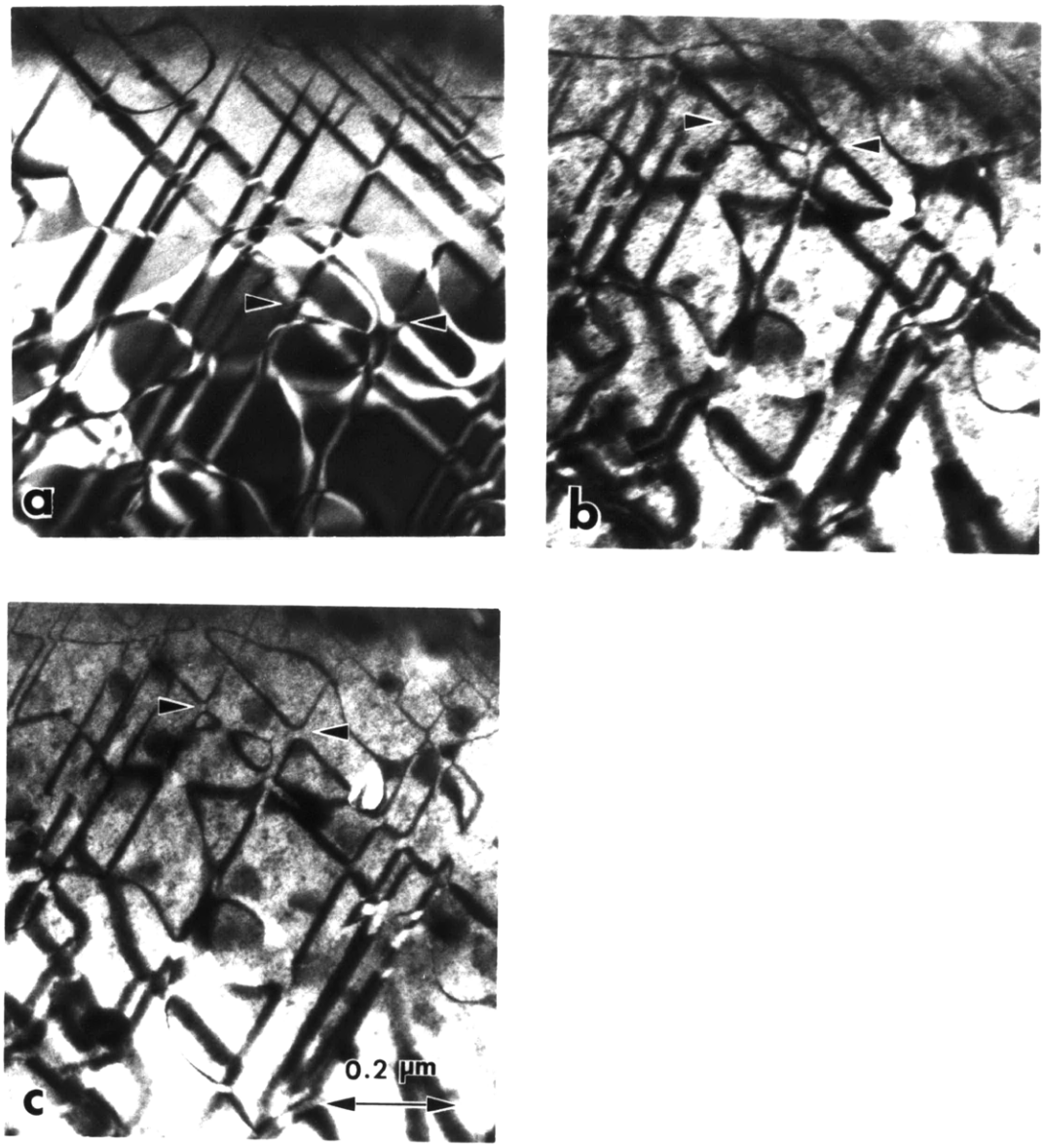

Figure (3-8) Dark-field electron micrographs showing the separation of planar intersecting APBs (Fe-24%Al) during heating at 700K (a) As deformed, (b) just after the temperature reached 700K, (c) after 5540 s at 700K

700K was determined to be 6×10^{-21} m^2/s, but the validity of this value for true intrinsic mobility is doubtful because of several reasons. The onset of the separation, which is believed to occur at the early stage of heating, cannot be detected in the superlattice dark-field image due to the drifting and instability of the specimen during quick heating. It is also difficult to determine when the specimen reaches the intended isothermal temperature as mentioned in the previous paragraph.

Due to these and other difficulties involved in this type of experiments which will be discussed in the later section on Discussion, we have decided that the separation experiments of planar intersecting APBs are not ideal for our purpose of the migration kinetics study.

3-2-3 Two-Dimensional Coarsening of Thermal APBs

Isothermal two-dimensional coarsening processes of the thermal APBs of Fe-26%Al alloys were observed using in-situ hot-stage TEM at temperature of 745, 778, 800, 838, 853, 910K, the first three temperatures being in DO_3 phase and the rest in B2 phase.

Superlattice dark-field micrographs using (111) reflections were taken at various time intervals at 745K and are shown in Figure (3-9). By measuring the change in the local curvatures and the corresponding migration distances in each succeeding micrograph, the mobility was calculated as the ratio of migration velocity to the instantaneous local curvature. Curvature changes and migration distances of the features A and B of Figure (3-9) are plotted in Figure (3-10) (a) and (b), respectively, as functions of time. In Figure (3-10) (a), which is the case of a shrinking circle, the curvature increases rapidly with time, becoming infinite when the circle totally disappears. Migration velocities can be calculated by curve-fitting data of migration distance vs. time. Calculated mobilities have an average value of 6.9×10^{-19} m^2/s with no apparent variation with curvature. In Figure (3-10) (b), the curvature does not change with time, and the migration velocity is constant over the range observed, giving a mobility value of 4.6×10^{-19} m^2/s. In general, the local curvatures can increase (e.g. circular APBs) or decrease (e.g. sinusoidal APBs) or remain roughly constant (e.g. hair-pin like APBs such as the feature B on Figure (3-9)) as the APBs migrate toward their centers of the curvature, depending on the shape of the APBs.

Figure (3-11) shows the migration of two-dimensional <100> APBs at 778K (in DO_3 phase) in the Fe-26%Al alloy. A number of small circular

Figure (3-9) In-situ hot-stage dark-field electron micrographs showing the migration of thermal APBs (Fe-26%Al, DO_3) at 745K. (a) Just after the temperature reached 745K, (b) after 1785 s, (c) after 3045 s, (d) A new area after taking (c), (e) the new area after 1335 s, (f) after 2640 s.

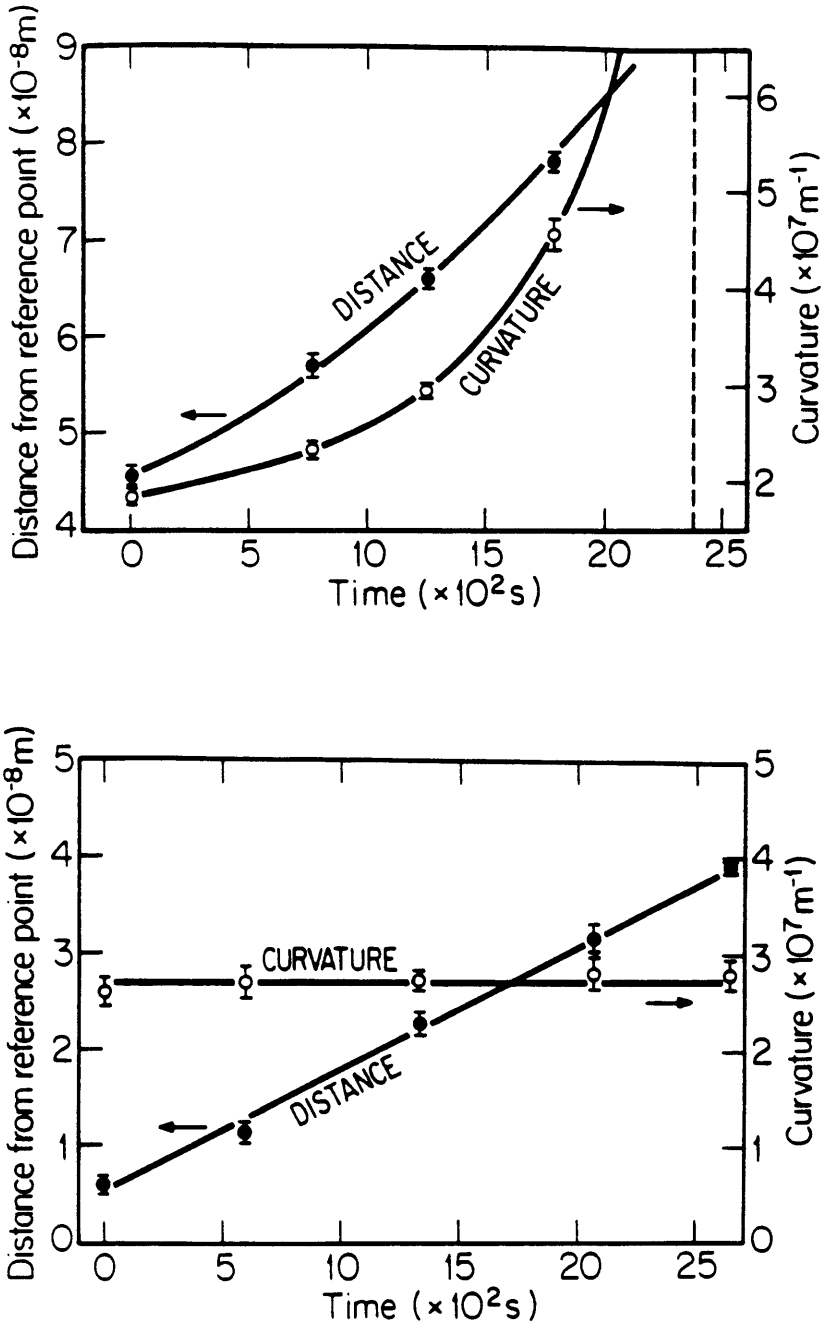

Figure (3-10) Curvature changes and migration distances with time at 745K. (a) Data from feature A of Figure (3-9), dashed line indicates the time at which the shrinking circle disappeared completely. (b) Data from feature B of Figure (3-9)

APBs with very high curvature ($K \geq 20 \times 10^7\ m^{-1}$) can be observed to disappear. Migrations of the features with smaller curvatures are less visible in the time interval taken in the four micrographs shown.

Figure (3-12) shows the migration of two-dimensional <111> APBs at 853K (in B2 phase) in the Fe-26% Al alloy. Because of higher temperature, the migration kinetics are much faster in Figure (3-12) than in Figure (3-11), and features with high curvatures ($K \geq 20 \times 10^7\ m^{-1}$) migrate too fast to be detected even in the shortest time interval between micrographs (> 16 s without using video recording equipment). An elliptic APB was shown to become circular before disappearing due to the higher curvature at the tips of longer axis (see feature A of Figure (3-12)). An analysis of the shape change of an elliptic APB toward a circular APB as it shrinks was carried out in Appendix C. This analysis shows that any elliptic APB will become circular as it shrinks, and it agrees with our numerous experimental observations.

In Figure (3-13), which was taken from the same sample at the same temperature as Figure (3-12), migration of hairpin-like feature is shown where the curvature at the tip of the "hairpin" remains virtually constant as it migrates. This kind of elongated APBs are not thermal APBs (thermal APBs are fairly isotropic in the Fe-Al alloys), but believed to be formed by the movements of dislocations during the heating of the thin-foil sample in TEM. Formation of these linear APBs during in-situ heating experiments is detrimental to our experiments, because the formation of these linear APBs across the thermal APBs which are being observed changes the whole picture by creating numerous intersections of APBs. This will be discussed more in the following section on Discus-

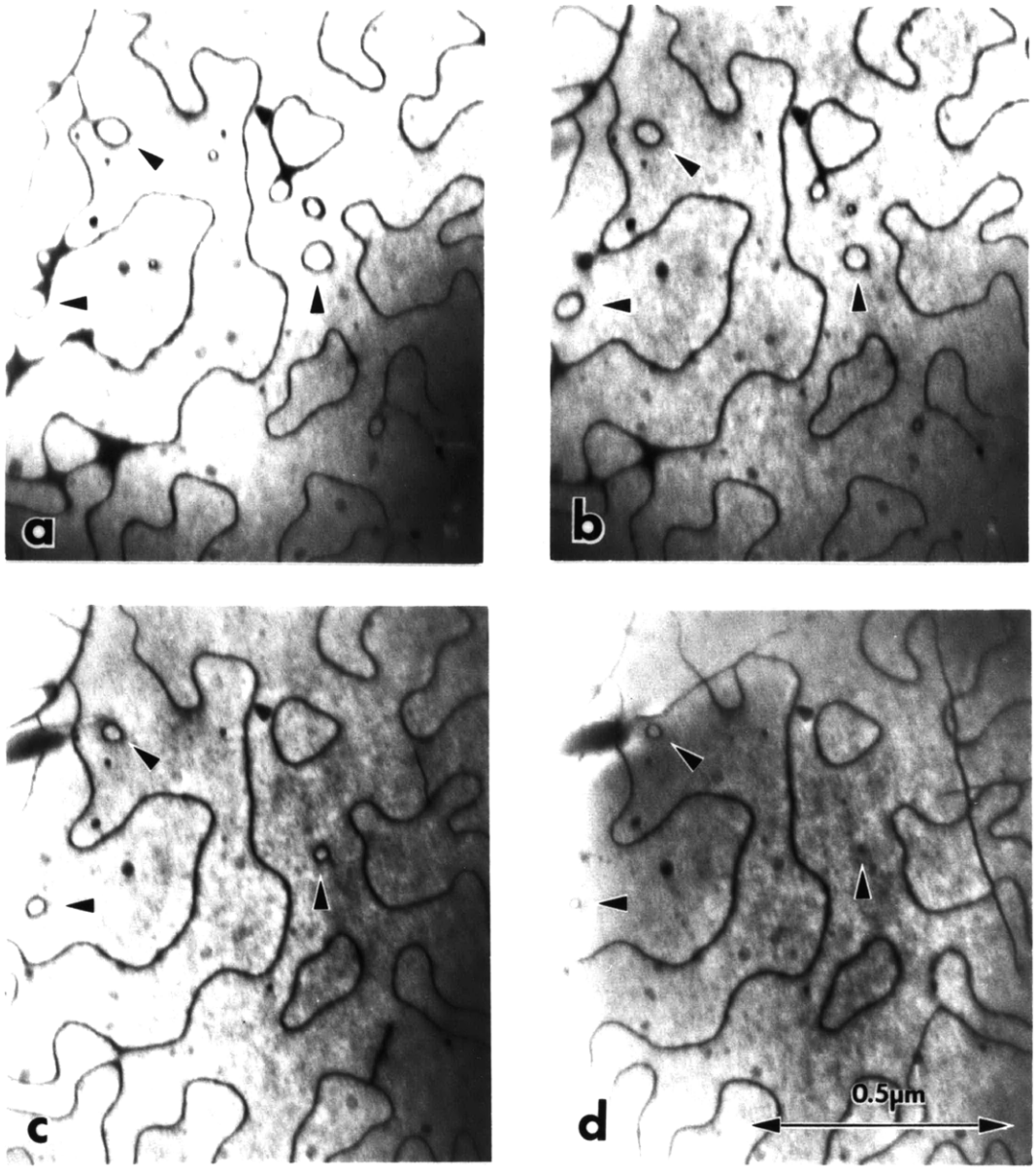

Figure (3-11) In-situ observation of coarsening of <100> APBs of 778K (Fe-26%Al). The time scale of the micrographs are: (a) 0 s, (b) 69 s, (c) 164 s, (d) 224 s.

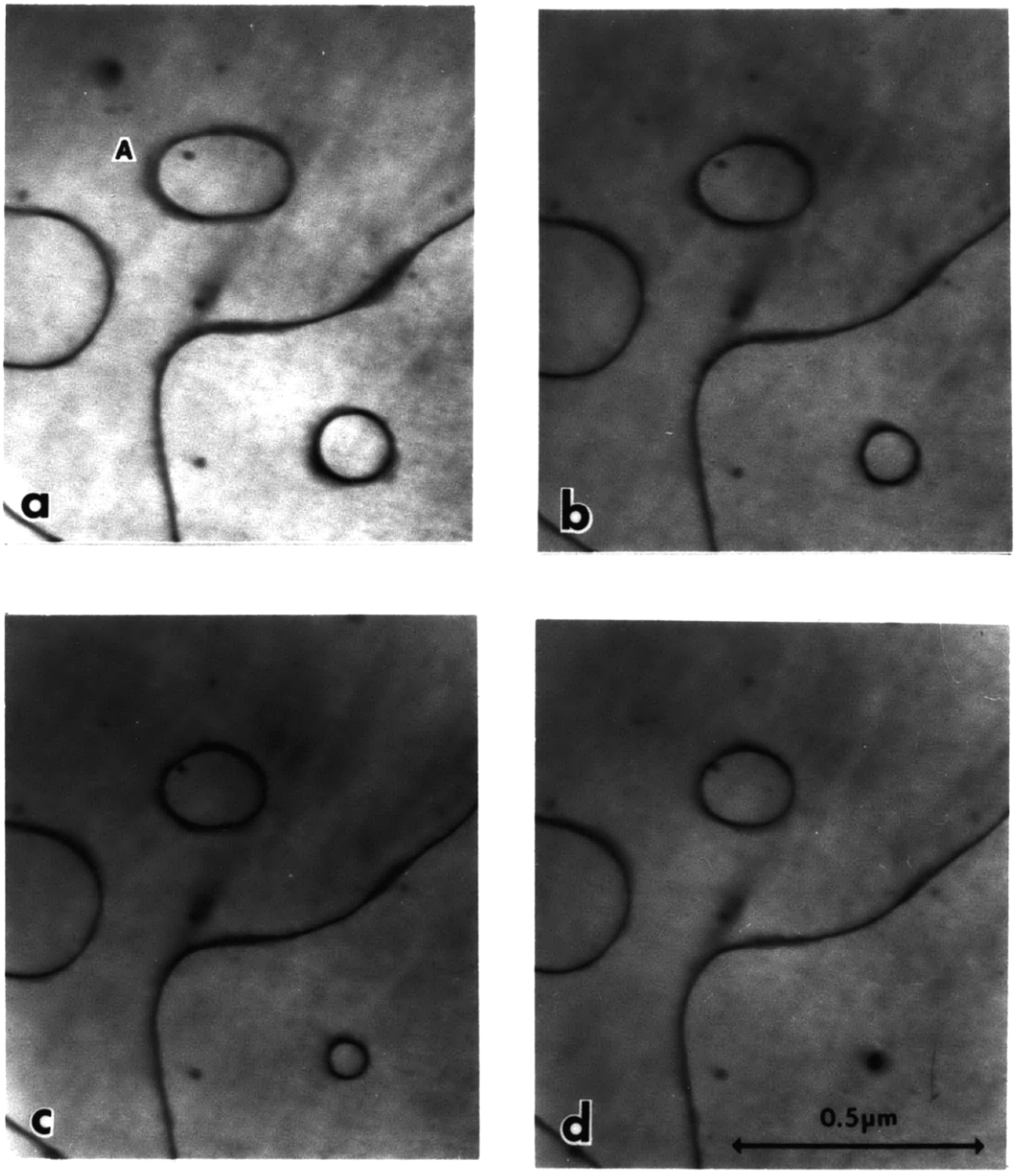

Figure (3-12) In-situ obervation of migration of <111> APBs at 853K (Fe-26%Al) (a) 0 s, (b) 38 s, (c) 62 s, (d) 84 s, (e) 132 s, (f) 154 s, (g) 180 s

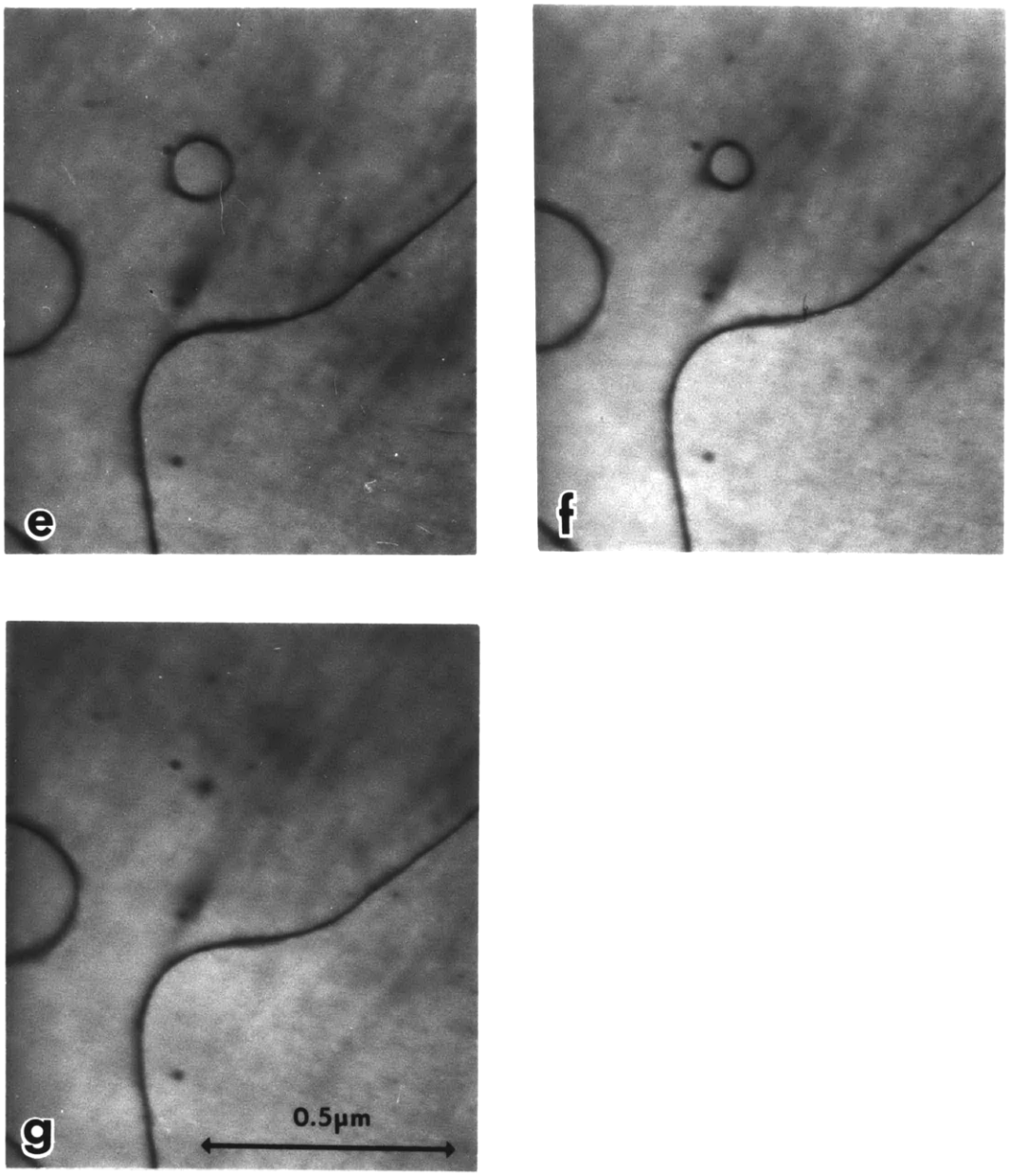

Figure (3-12) continued

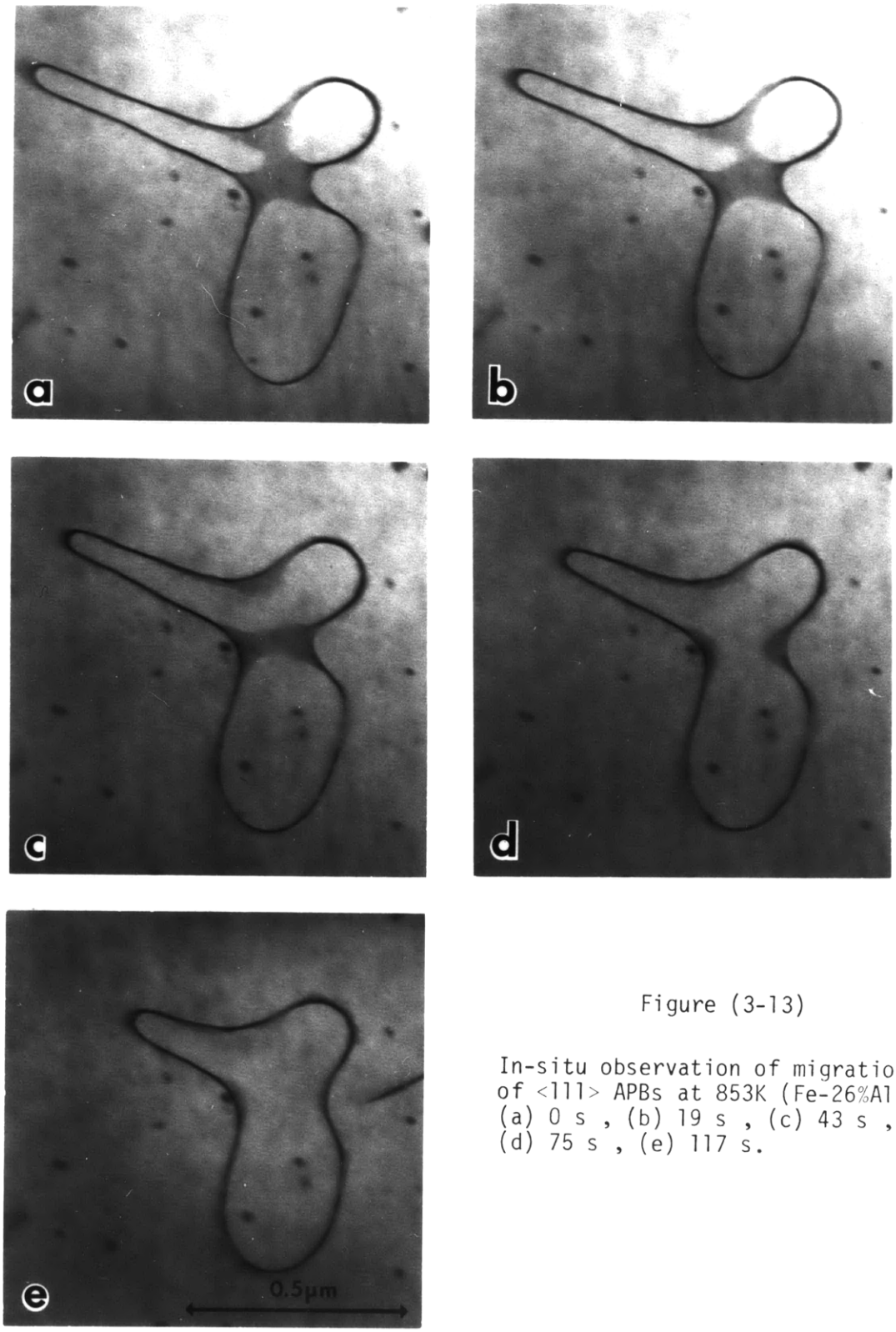

Figure (3-13)

In-situ observation of migration of <111> APBs at 853K (Fe-26%Al) (a) 0 s , (b) 19 s , (c) 43 s , (d) 75 s , (e) 117 s.

sion.

Figure (3-14) summarizes all the data obtained at 745K, giving average mobility for <100> APBs in DO_3 ordered Fe-26%Al alloy, M = 4.8×10^{-19} m^2/s with a standard deviation of 1.3×10^{-19} m^2/s. No systematic dependence of mobility on curvature is apparent. Mobility data for <100> APBs of the same alloy at 778K and 800K are plotted on Figure (3-15) and Figure (3-16) respectively. In plotting these data in Figure (3-14) through Figure (3-19), error bars for individual data points were omitted since the error ranges for the curvature and mobility determination of each data point are relatively quite small compared to the scatter of data points, comparable to the size of square dots used in the plots. But it should be mentioned that the error ranges are larger for the data points of smaller curvatures because of slower kinetics.

Average mobilities of <100> APBs at 778K and 800K are 2.9×10^{-18} m^2/s and 4.7×10^{-18} m^2/s respectively. There is slight tendency of decreased mobility for low curvatures (i.e. $K \simeq 1 \times 10^7$ m^{-1}), though the extent of decrease can be seen as being within the experimental errors. Accurate measurement of the mobility becomes more difficult as the curvature decreases because the absolute migration distance is proportional to the curvature. Measurement of migration distances for low curvature APBs has larger error ranges.

Mobilities of <111> APBs in B2 ordered Fe-26%Al alloys are plotted on Figure (3-17), Figure (3-18) and Figure (3-19) for T=838K, T=853K, and T=910K respectively. The data presented in Figure (3-14) through Figure (3-19) show no evidence for a dramatic change of mobility over the range of curvatures accessible in the experiment. Since the data extends to

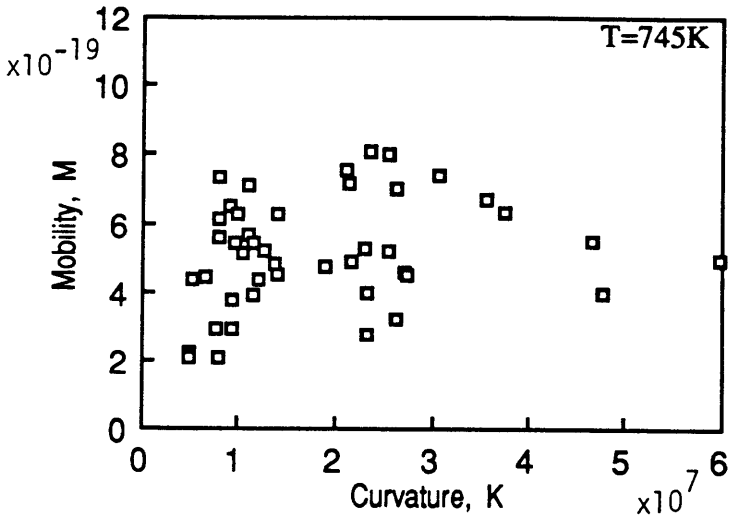

Figure (3-14) Mobility M (m^2/s) vs. curvature K (m^{-1}) of APBs as measured from in-situ experiments. <100> APBs in the Fe-26%Al at 745K.

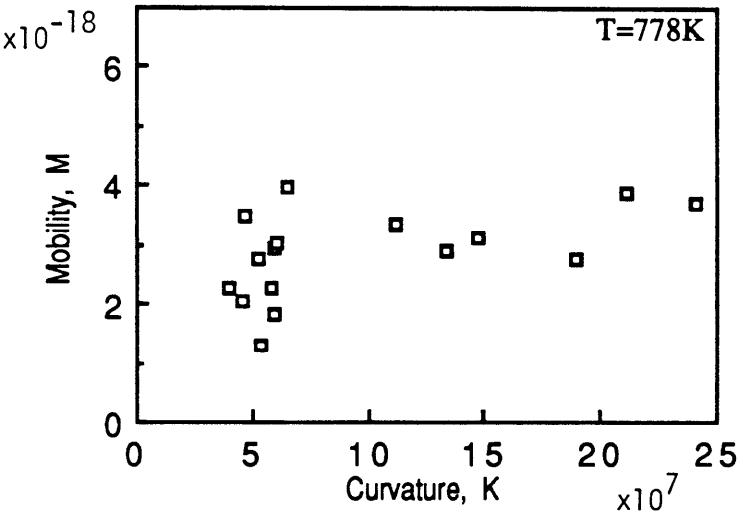

Figure (3-15) Mobility M (m^2/s) vs. curvature K (m^{-1}) of APBs as measured from in-situ experiments. <100> APBs in the Fe-26%Al at 778K.

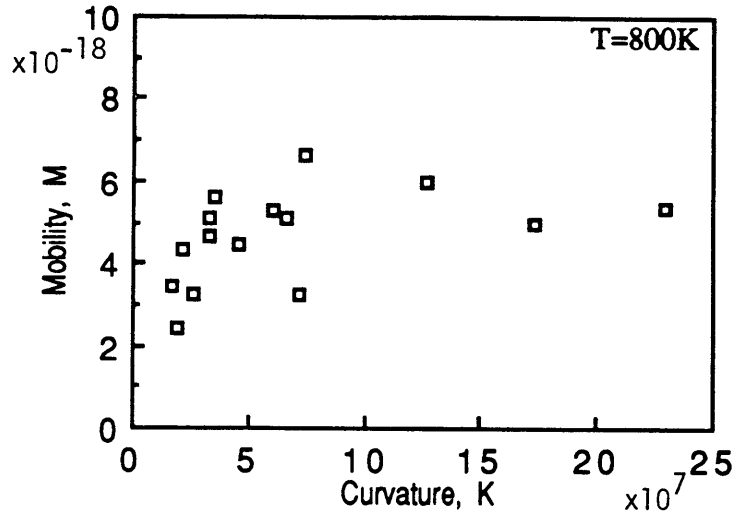

Figure (3-16) Mobility M (m^2/s) vs. curvature K (m^{-1}) of APBs as measured from in-situ experiments. <100> APBs in the Fe-26%Al at 800K.

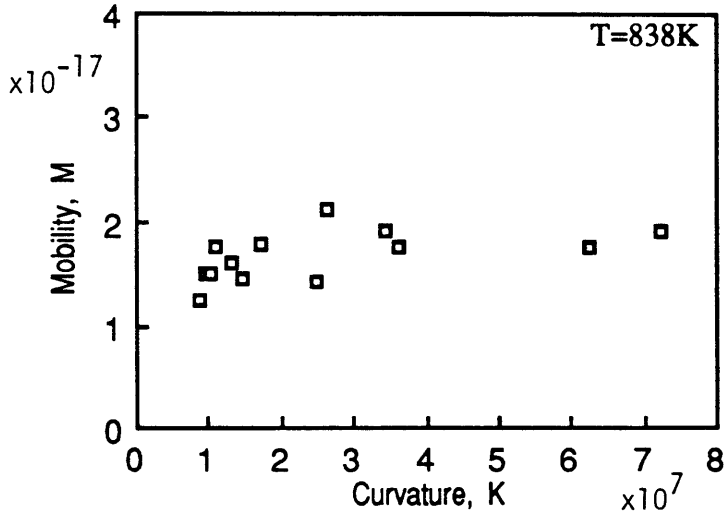

Figure (3-17) Mobility M (m^2/s) vs. curvature K (m^{-1}) of APBs as measured from in-situ experiments. <111> APBs in the Fe-26%Al at 838K.

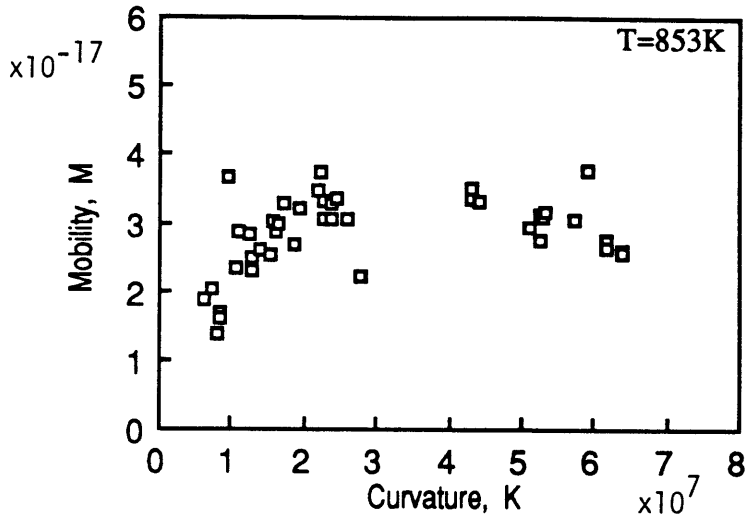

Figure (3-18) Mobility M (m^2/s) vs. curvature K (m^{-1}) of APBs as measured from in-situ experiments. <111> APBs in the Fe-26%Al at 853K.

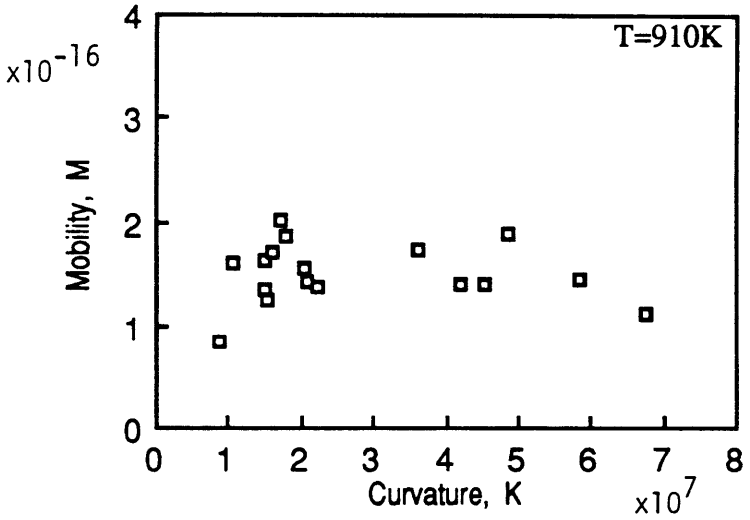

Figure (3-19) Mobility M (m^2/s) vs. curvature K (m^{-1}) of APBs as measured from in-situ experiments. <111> APBs in the Fe-26%Al at 910K.

domain radii as low as 5 nm ($K = 2x10^8\ m^{-1}$), we believe that the bulk of the observations yield mobilities for the intrinsic regime of migration. Average mobilities with standard deviation are summarized in Table (3-3).

Table (3-3)

Intrinsic Mobility of APBs as determined by in-situ Experiments in an Fe-26%Al Alloy

APB type and Phase	Temp (k)	M (m^2/s)	σ (m^2/s)	(%)
<100> DO_3	745	4.8×10^{-19}	1.3×10^{-19}	27
<100> DO_3	778	2.9×10^{-18}	7.5×10^{-19}	26
<100> DO_3	800	4.7×10^{-18}	1.1×10^{-18}	23
<111> B2	838	1.7×10^{-17}	2.4×10^{-18}	14
<111> B2	853	2.9×10^{-17}	5.7×10^{-18}	20
<111> B2	910	1.5×10^{-16}	2.4×10^{-17}	16

σ = standard deviation

An Arrhenius plot of the mobility M vs. 1/T for Fe-26%Al is shown in figure (3-20). From this plot, we can get the activation energies of $2.1x10^5$ J/mole and $1.95x10^5$ J/mole for the APB migration process in DO_3 and B2 phases respectively. These activation energies agree very well with the activation energy of interdiffusion in disordered Fe-25%Al which was reported to be around $2x10^5$ J/mole [63].

We might expect more apparent discontinuity in the Arrhenius plot at B2→DO_3 transition temperature and higher activation energy for the DO_3

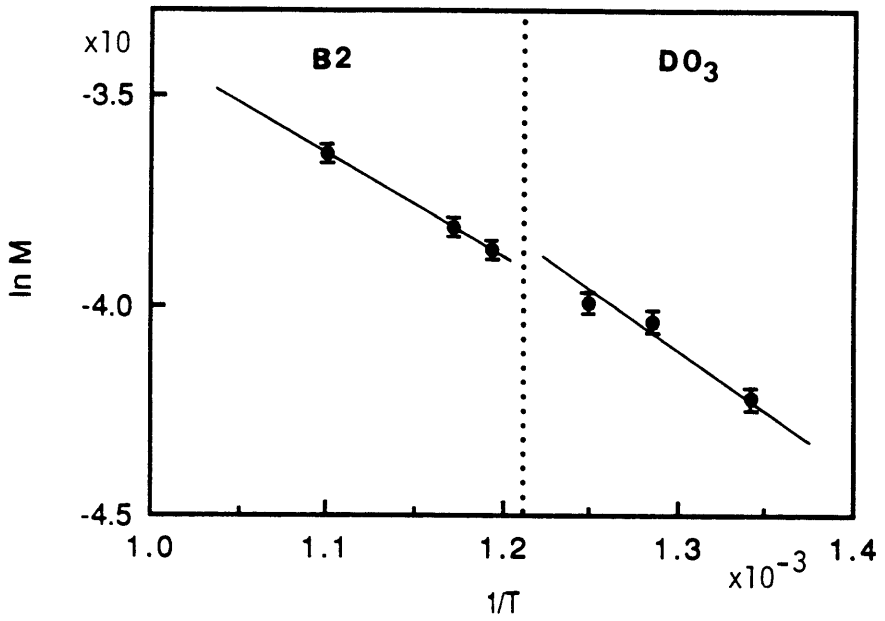

Figure (3-20) Arrhenius plot of mobilites M determined from in-situ migration experiments. Dotted line indicates the critical temperature T_{cr} = 826K for the Fe-26%Al alloy. Data at the left side of the dotted line are for <111> APBs in the B2 phase, which give the activation energy of Q = 1.95×10^5 J/mol. Data at the right side of the dotted line are for <100> APBs in the DO_3 phase, which give Q = 2.10×10^5 J/mol.

phase because of more ordered structure of the DO_3 phase according to the widely accepted study of Kuper et al. [64]. This point will be discussed in the following section of Discussion.

3-3 Discussion

3-3-1. Difficulties Involved in Separation Experiments of Planar Intersecting APBs.

Besides the time-consuming trace analysis required to identify the slip systems, there are several difficulties in carrying out separation experiments of planar intersecting APBs to get the reliable values for the mobility of these APBs.

(a) Ability to Produce Planar APBs by Deformation.

We have not succeeded to produce planar APBs other than in Fe-24%Al alloys (we have tried Fe-26%Al and Fe-30%Al). This might be due to the increase of APB energy as Al content increases. As the APB energy increases, the dislocations in ordered alloys are likely to move in the form of superlattice dislocations without leaving planar APBs on the slip planes.

There have been several studies on the deformation of the Fe-Al ordered alloys where the superlattice dislocations were observed in alloys with an Al content higher than 26 atomic percent [66-69]. It was also reported that the formation of superlattice dislocations is thermally activated [70], and the fact that we performed the plastic deformation at 433K for smooth slip deformation made it even more difficult to produce planar APBs by assisting the nucleation of superlattice dislocations.

Even in the cases where we succeeded to produce planar intersecting APBs, we can not get various intersection angle because it was determined

by the deformation geometry. Thus this technique is very limited in terms of the range of curvatures as well as the alloy composition to study the migration kinetics.

(b) Temperature Uncertainty and Instability of the Images at the Early Stage of Heating.

The real temperature of the rapidly heated sample in the heating specimen holder can not be determined accurately until the steady state is achieved. During the rapid heating, specimen in the form of thin foil moves resulting in drift of the TEM image, and the recording of sharp images is not possible until the image is stabilized. Because of these two reasons, the onset of the separation of planar intersecting APBs which occurs at the early stage of heating can not be detected accurately. This problem gets worse at higher temperature, because the required time for temperature steady state and image stabilization becomes longer whereas the migration kinetics become faster as temperature increases.

(c) Multiple Domain Configuration at Intersection

Four different domains can be produced in DO_3 phases by dislocation movements. In DO_3 structure, superlattice dislocations are composed of four dislocations of ½<111> type, which are schematically sketched in Figure (3-21) along with the superlattice dislocations in B2. Unlike the planar APBs produced in B2 phase, planar APBs produced in DO_3 phase can be either of <111> APBs or <100> APBs depending on the number of dislocations which moved on the slip plane. This is also schematically sketched in Figure (3-21) along with the four domains separated by the ½<111> type

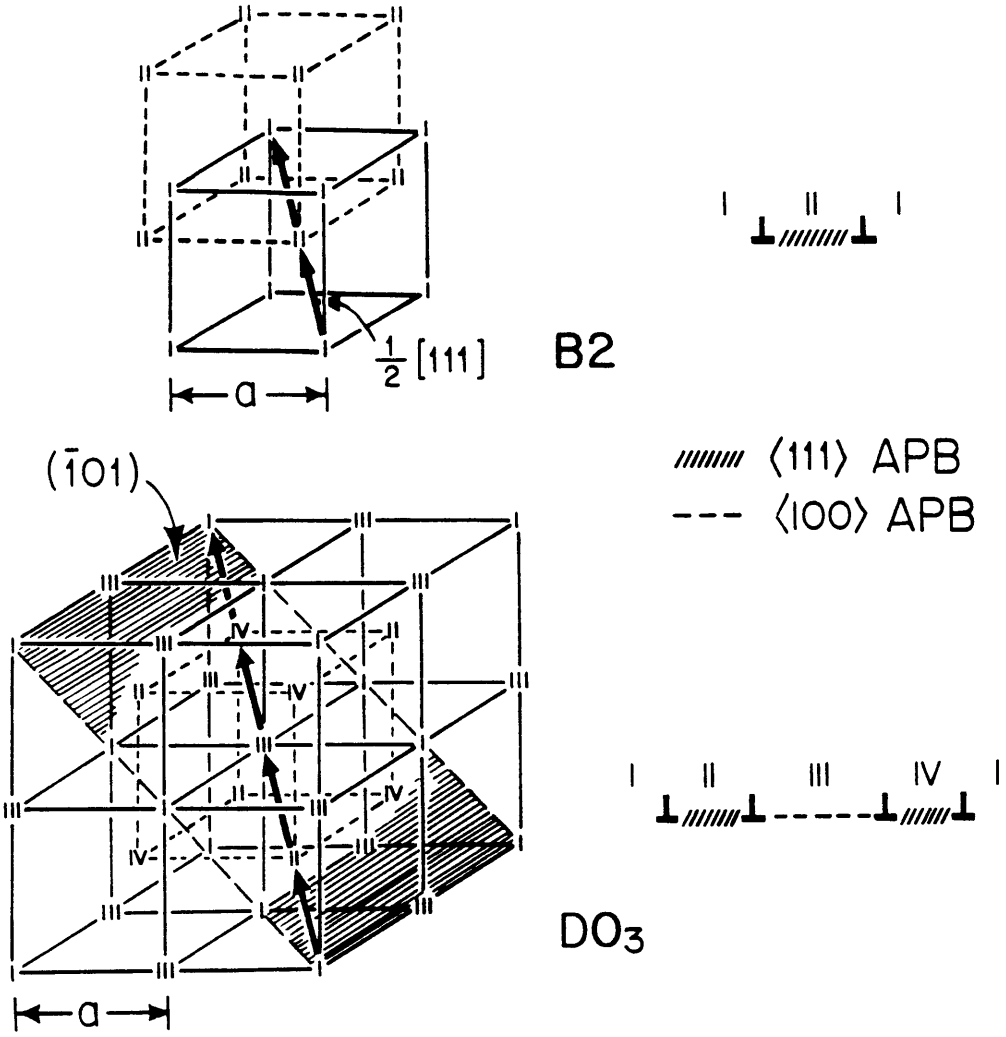

Figure (3-21) Sets of superlattice dislocations and APBs formed by the dissociation of superlattice dislocations in B2 and DO_3 ordered structures. From Reference [66].

dislocations.

Thus if we get planar intersecting APBs by plastic deformation in DO_3 ordered alloys, we can have two different separation configurations as sketched in Figure (3-22) when these intersections are allowed to pull apart by heating. Figure (3-22) (a) shows the separation of two hyperbolic <100> APBs. Similar separation of <111> APBs is shown in (b). In Figure (3-22) (c), the separation of the two hyperbolic sheets of <111> APBs leaves additional <100> APBs along the centerline. In this case, the separation kinetics will be retarded by the additional <100> APB, and the hyperbolic shape will be altered to form metastable junctions at the tip where <111> APBs and <100> APB meet. This kind of separation was actually observed in our experiments, and in that case, the separation distance is significantly smaller.

Relative probabilities of having <100> APBs or <111> APBs by deformation in DO_3 ordered alloys are dependent on the relative magnitude of the energies of <100> APBs and <111> APBs which will determine the dissociation distances between component dislocations of superlattice dislocations. The energies of <111> APBs and <100> APBs in Fe-24%Al DO_3 ordered alloys at room temperature are comparable to each other ($\simeq 8\times10^{-4}$ J/m^2 according to ref. [66]), and consequently the relative probabilities of having <111> and <100> APBs are comparable.

Deformation of B2 ordered alloys will always produce <111> APBs and there will be no case similar to Figure (3-22) (c). But the need to heat the sample into B2 phase which is higher temperature phase causes the severer problems with this type of experiment, as described in previous section.

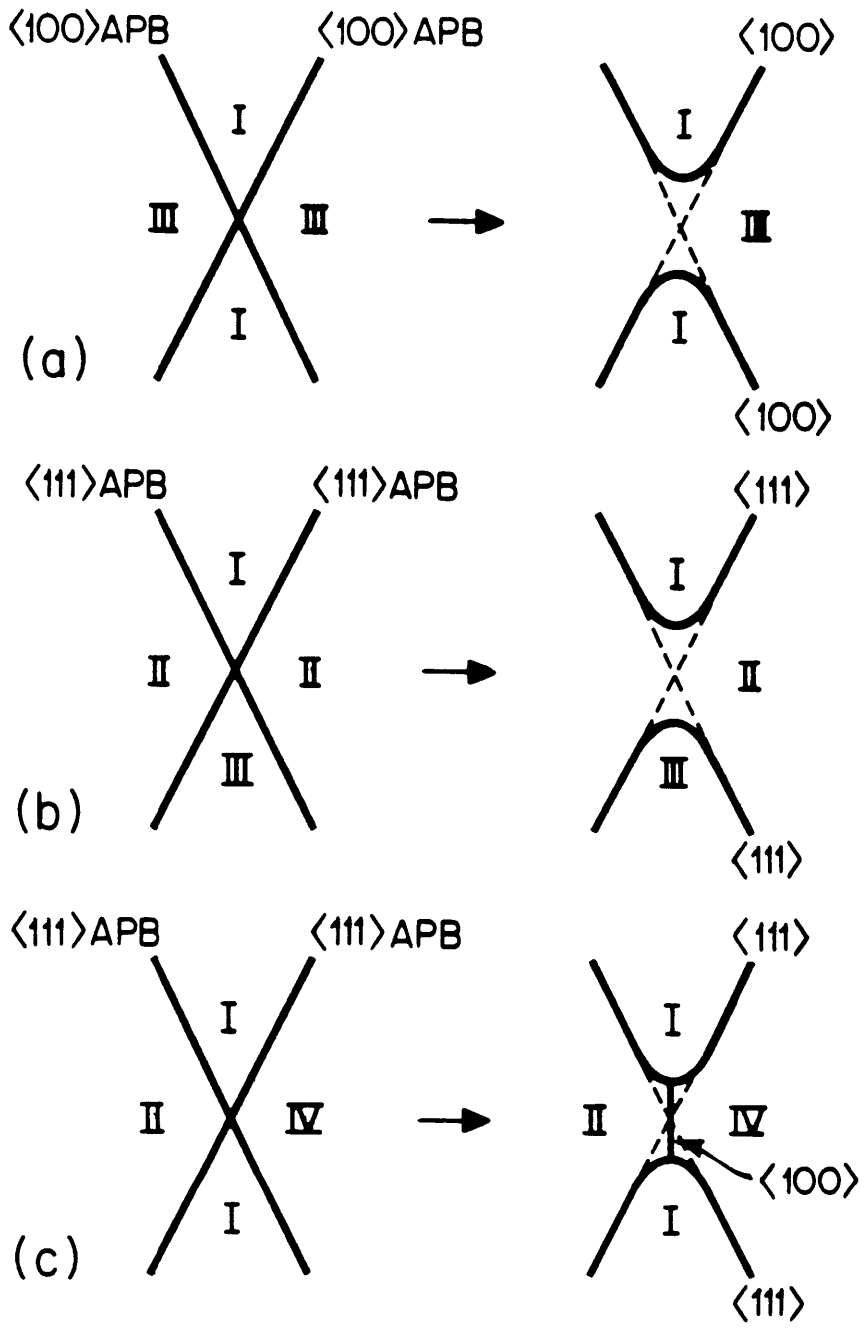

Figure (3-22) Three different types of intersections which can be produced by slip deformation in DO_3 ordered phase and their separation upon heating.

3-3-2. Bulk Domain Coarsening Experiments.

Domain coarsening experiments on bulk specimens give results similar to those obtained by Krzanowski and Allen [22], namely that over a limited range of domain sizes, Equation (1-20) was obeyed. The plots presented in Figure (3-7) indicate a change in growth kinetics that occurs at approximately $S_V \simeq 1.4 \times 10^7$ m^{-1} at 745K and $S_V \simeq 7 \times 10^6$ m^{-1} at 778K. These values correspond to domain sizes (in mean linear intercept, D) of 140 and 260 nm, respectively. Although significant statistical errors are present in the measurements at the largest domain sizes, it is nonetheless clear that the domains coarsen more rapidly at small domain sizes, particularly at 745K.

Such behavior would be expected if solute drag processes influenced the migration of these boundaries as discussed in the Introduction. Small domain sizes correspond to high driving forces for APB migration, since the driving force for capillarity-driven migration is proportional to interface curvature. Conversely, the behavior at large domain sizes is in response to low driving forces for migration. If solute drag processes are important, the migration kinetics in the low driving-force regime would be controlled by diffusion of the solute "atmosphere" with the migrating boundary, resulting in what is termed "extrinsic" behavior. In the high driving-force regime of solute drag behavior, the boundary velocities are too high for solute atoms to keep up, and the kinetics are governed by the kinetics of reordering that occurs in the vicinity of the APB. The resulting migration kinetics are said to be "intrinsic".

Krzanowski and Allen [21] presented a calculation of the expected solute drag force to support their conclusion that the change of domain

coarsening kinetics observed in the B2 ordered Fe-24%Al alloys was due to a solute drag effect. Direct application of their calculation in our experiments is not feasible for the reasons described in Section 1.3.2 in the Introduction. Theoretical efforts to calculate most stable profiles of compositional and order parameter variation at APBs are in progress [72]. Lacking this result, we make the tentative conclusion that the transitional behavior observed in the data presented in Figure (3-7) are due to a solute drag process.

3-3-3. In-Situ Two-Dimensional APB Migration Experiments

The in-situ two-dimensional boundary migration experiments allow for the first time, the measurement of the mobilities of APBs, over a wide range of curvatures (and hence driving forces). It is a versatile technique, in that the mobility data obtained span more than three orders of magnitude (see Table (3-3)). There is also relatively little scatter in the data at a given temperature, because of the large number of data points that can be analyzed from a series of micrographs. Another virtue of the technique is that the inevitable shrinking and disappearance of single domains will always result in an increase of driving force to extremely high values as the domain collapses on itself and disappears. This contrasts with the separation of planar intersecting APBs and domain coarsening in bulk specimens in which the driving force steadily decreases. Thus by observing those shrinking domains, it guarantees access to the intrinsic regime of solute drag behavior.

To maintain the validity of the two-dimensional approximation, only the APBs aligned normal to the thin foil surface, appearing as thin sharp lines on the image, were considered for measurement. One possible cause of the data fluctuation in Figure (3-14) through Figure (3-19) is that the APBs may not be perfectly aligned normal to the surface and the curvature on the surface may not give the mean principal curvature. If there is a small through-thickness curvature which has the same sign as that on the foil surface, the calculated mobility using just the curvature on the foil surface will be higher than the true mobility, and a through-thickness curvature of the opposite sign will reduce the calculated mobility. This point is illustrated schematically in Figure (3-

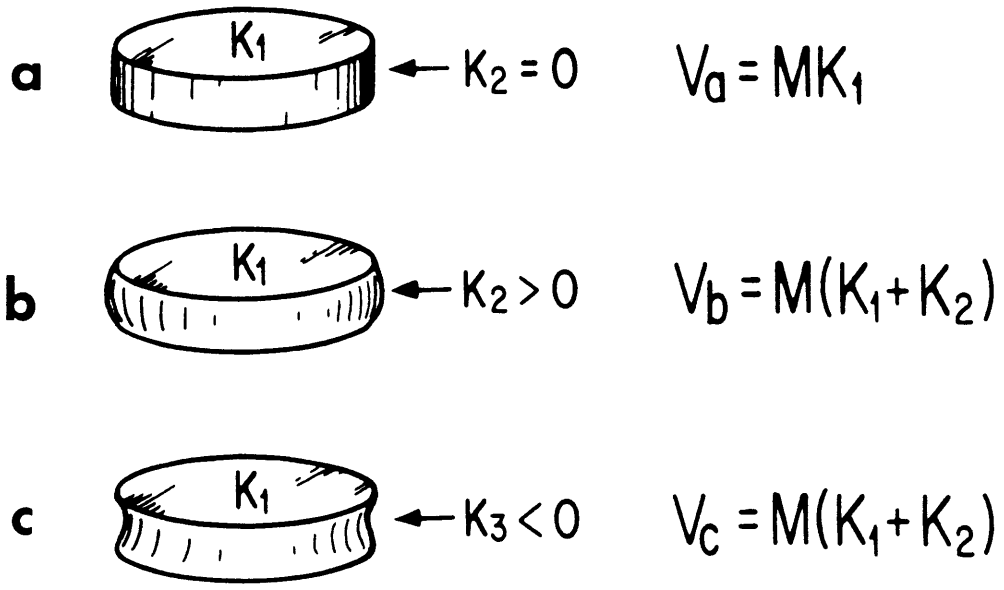

Figure (3-23) Three possible APBs in thin foil TEM samples which may give apparently circular APB images with curvature K_1. (a) has a truly two-dimensional curvature ($K_2 = 0$), (b) has a positive (the same sign as K_1) K_2, and (c) has a negative K_2. Mobility from Va gives true value when only K_1 is measured.

23). All three apparently circular APBs (as they appear in projected TEM images) have the same curvatures on the sample foil surface (K_1). But the through-thickness curvatures (K_2) are $K_2 = 0$, $K_2 > 0$, and $K_2 < 0$ for (a), (b), and (c) respectively. Circular APB (cylindrical, more precisely) in (a) will shrink faster than the APB in (c) but slower than the APB in (b). If we calculate the mobilities by measuring K_1 values only, the mobility from (b) will be higher, and the mobility from (c) will be lower than the mobility determined from (a) which is the true mobility. If there is appreciable surface pinning at the intersection of APBs with the surface of a thin-foil sample, we can expect to have something like Figure (3-23) (c) where K_2 has the opposite sign. This would result in the measurement of lower than actual mobility.

Another possible source of errors is the surface irregularity of thin-foil specimens. If there is large thickness variation in the sample, APBs moving to a thinner area will be accelerated and APBs moving to a thicker area will be decelerated. But the thickness variations in our samples are generally small and gradual, and this would not be much concern in our experiments.

3-3-4 Temperature Dependence of the Mobility

The observed temperature dependence of the mobilities, shown in Figure (3-20) is somewhat surprising. As mentioned earlier in Chapter 1, the mobility, as defined by Equation (1-13), is proportional to the product of a gradient energy coefficient of ordering $K\eta$, and a coefficient α that is related to the kinetics of ordering. The values for the gradient energy coefficients of ordering for B2 and DO_3 order, K_{η_1} and K_{η_2}, were calculated in chapter 2. These quantities are independent of temperature. Values for the Fe-26%Al alloy are presented in Table (3-4).

Table 3-4

Calculated Values of Gradient Energy Coefficients for APBs in Fe-26%Al

APB Type and Phase	Gradient Energy Coefficient K_η, J/m
<111>, B2 and DO_3	4.7×10^{-11}
<100>, DO_3	2.0×10^{-11}

Values for the <100> APBs in the DO_3 phase are seen to be lower by a factor of 2.3 compared with those for <111> APBs in the B2 phase. We have no detailed prediction for the expected temperature variation of the kinetic coefficient α. To a first approximation, we expect it to have a simple Arrhenius dependence within a given phase, similar to an interdiffusion coefficient. But if α does behave like the interdiffusivity, a change to a higher activation energy in the DO_3 phase would be expected [64]. There have been two independent studies on the interdiffusion in A2 and B2 phases in the Fe-Al system [63, 71]. Even though the magni-

tudes of the diffusivities differed between these studies, both studies indicated increased activation energy in B2 ordered phase compared to the activation energy in disordered A2 phase. The more reliable of these two studies gives the activation energy for interdiffusion in disordered A2 phase of $\simeq 2.1 \times 10^5$ J/mol and in B2 phase of $\simeq 2.6 \times 10^5$ J/mol for the Fe-26%Al alloy [63]. Interdiffusion in DO_3 phase has not been studied experimentally mainly due to the slow kinetics at low temperatures where DO_3 order occurs, but we can assume that the activation energy in DO_3 phase is still larger than that in B2 because of more ordered structure of DO_3 phase.

Activation energy calculated from the left-hand portion (B2) of Figure (3-20) is 1.95×10^5 J/m which is comparable to the activation energy of interdiffusion in disordered solid solution (2.1×10^5 J/mol). This can be explained as follows. At the center of a diffuse <111> APB in B2 phase, the order parameter is zero, and order parameter gradient ($d\eta/dx$ from Figure (1-2)) is the maximum at that point. The extent of the local atomic rearrangement required at migrating APBs is dependent on the order parameter gradient. Thus the extent of the atomic rearrangement required at the center of a migrating diffuse APB is the largest. And it becomes smaller at the both edges of the APB where the order parameter gradient approaches zero. Therefore, it may be possible that the change of the order parameter at the center of the APB is rate-controlling process for migration, even though the diffusion rate at the center of the APB is higher. If that is the case, the activation energy of the APB migration will be that of the interdiffusion in disordered α phase.

If the same argument is applied to the migration of <100> APBs in DO_3 phase, the activation energy of DO_3 phase calculated from the right-hand portion of Figure (3-20) should have a value comparable to the activation energy of interdiffusion in B2 phase which is higher than that for disordered A2 phase. At the center of diffuse <100> APBs in DO_3 phase, the DO_3 order parameter η_2 is zero. But B2 order parameter η_1 is constant across the <100> APBs, and the diffusion at the center of <100> APBs would be similar to the diffusion in a B2 ordered phase.

Thus, the generally expected form of Figure (3-20) would be for the right-hand (DO_3) portion of the curve to have a steeper slope, and for a discontinuity to exist at the critical temperature, the magnitude of which depends on the difference between the gradient energy coefficients.

3-3-5 Comparison of Bulk and In-Situ Studies

A comparison of the data obtained in the bulk and the in-situ migration experiments carried out at 745 and 778K allows the topological constant ϕ defined in Equation (1-21) to be determined. In making this comparison, we assume that the in-situ experiments give data for intrinsic migration kinetics, and we use the data from the high-driving force regime of Table (3-2). The calculations give $\phi = 1$ at 745K and $\phi = 0.5$ at 778K. These results seem surprisingly large. For an idealized structure of right circular cylindrical domain boundaries occupying half of the volume of the material, it is easily shown that $\phi = 1$. Thus, the analysis of the experimental data implies that the domain boundary shapes in bulk specimens are on average cylindrical. This is at variance with the long-recognized concept of a multiply-connected morphology for the domain structure [23]. The values of ϕ implied by this study could be too large if some unanticipated drag force were operating in the thin foil experiments. The most obvious possibility, grooving at the intersections of the APBs with the surfaces of the thin-foil specimens, should be negligible because the APB energies are so small in comparison to the free surface energies (APB energies will be calculated in the next chapter). Additional analysis is required to fully interpret the value of ϕ calculated here.

Given the value of S_V at the point where the bulk domain coarsening kinetics change, as seen in the plots of Figure (3-7), plus knowledge of ϕ, it is possible to estimate the curvature K^* at which the transition to high driving-force behavior would be expected in the in-situ experiments. The calculation gives estimates of the conditions for high driving-force

behavior when $K^* > 1.4 \times 10^7$ m^{-1} at 745K, and when $K^* > 0.5 \times 10^7$ m^{-1} at 778K. From Figure (3-14) and Figure (3-15), it is seen that a portion of the data points at 745K falls below this curvature value, while all of the data points at 778K lie well above this curvature value. The most basic conclusion from this analysis is that the bulk of the in-situ data were indeed taken in the high driving-force "intrinsic" regime. The data at 745K shown in Figure (3-14) are not consistent with a change of M when $K^* = 1.4 \times 10^7$ m^{-1}. One possible reason for this is a rather large uncertainty in the value of S_V where M changes in the bulk domain coarsening experiments (i.e. the point where the slope changes in Figure (3-7)). There is a tendency in the data from the in-situ experiments at 745K for reduced mobilities when $K < 0.7 \times 10^7$ m^{-1}, but for such gentle curvatures migration distances are small, and hence errors in the measurements are larger than for the high-curvature data points. A second possibility is that the actual value of ϕ is less than that reported above. This would make the true value of K^* smaller.

3-3-6 Limitations in In-Situ Hot-Stage Experiments.

Through the current study, we have demonstrated unique merits of in-situ experiments employing heating specimen holder in TEM in studying the migration kinetics of the APBs in Fe-Al alloys. But there are some limitations which should be considered before trying to apply this experimental technique to other systems.

(a) Heating Rate and Time Required to Achieve Steady State

Instantaneous heating up to a desired temperature is impossible with the heating holder, and the exact temperature during the transient period before the specimen reaches steady state can not be determined. Furthermore, the TEM images of the sample during this transient period drift and well focused images can not be recorded. To get high quality images the microscope needs to be realigned and the specimen orientation readjusted after the specimen becomes stable. All of these factors make it very difficult to detect any changes in the sample which might occur at the early stage of heating. Therefore, experiments which are mainly intended to detect changes at the early stage of heating will not be very suitable for in-situ hot-stage experiments.

(b) Range of Kinetics

Even though we have successfully observed the migration kinetics over more than three orders of magnitude, there are practical limits of kinetics on both the high and low ends which can be covered. If the migration velocity V is smaller than $V < 1x10^{-13}$ m/s, the migration distance

in four hours of heating should be less than 1.5×10^{-9} m which will be very difficult to detect in good accuracy (0.15 mm of migration distance on the micrograph of magnification 10^5). If the migration velocity is larger than $V > 1 \times 10^{-8}$ m/s, conventional photographic images would not be suitable and a video recording device should be needed.

The migration velocity is given as the product of the mobility and the curvature. For the curvature of $K = 5 \times 10^7$ m^{-1}, $V = 1 \times 10^{-13}$ m/s gives $M = 2 \times 10^{-21}$ m^2/s. Extrapolating for this value in Figure (3-20) gives T = 640K. $V = 1 \times 10^{-8}$ m/s give $M = 2 \times 10^{-16}$ m^2/s. Extrapolating this value gives T = 925K. So if we observe a migrating APB having $K = 5 \times 10^7$ m^{-1} in an Fe-26%Al alloy, temperatures of 640K and 925K would be the lower and upper limits.

Similarly, there is also a limit in the range of the curvatures which can be covered at a given temperature. If the curvature is too small, migration velocity will be too small to be measured accurately. In addition, the errors in the measurement of a small curvature (gently curved) is much larger than the errors involved in the measurement of a large curvature (sharply curved). Because of these reasons, we were not able to accurately determine the mobilities when the curvature is lower than 1×10^7 m^{-1}.

(c) Specimen Damage during Observation at Elevated Temperatures.

We have observed the formation of APBs by the movement of dislocations during TEM observation at elevated temperatures. These APBs are formed preferentially along specific crystallographic orientations, and the process seems to be thermally activated (that is, the formation and

the movement of dislocations seem to occur faster at higher temperatures). These dislocations are believed to be formed by the thermal stresses during heating. APBs forming during the observation at high temperatures are detrimental in studying migration kinetics of APBs. The movement of a dislocation across a thermal APB which is being observed will alter the geometry of the APB. This might be a serious problem particularly when we need to observe the migration of very gently curved APBs which require long time intervals to detect movements.

CHAPTER 4

CALCULATION OF THE ENERGIES AND PROFILES OF THE APBs

There have been several studies on the calculation of APB profiles and energies. Kikuchi and Cahn [54] calculated APB profiles in the body centered cubic stoichiometric B2 alloy using both discrete lattice models of the pair approximation and the Bragg-Williams approximation and a continuum model at temperature of $T = 0.728T_c$ and $T = 0.611T_c$. The discrete profiles were found to agree well with the continuum curves at these temperatures. Furthermore, for the b.c.c. structure, the domain wall energy was isotropic, as is assumed in the continuum diffuse interface theory [17]. Lee and Aaronson [71] calculated coherent interphase boundary structures and energies using discrete lattice and continuum models. They determined that at temperatures above $T = 0.75T_c$ the continuum and discrete lattice models gave equivalent results.

Krzanowski [20] calculated the order parameter and composition profiles and the energies of APBs in the single-phase B2 ordered Fe-Al alloys near the bicritical point applying the diffuse interface theory. But in his calculation he miscalculated the gradient energy coefficient for composition K_c as a positive value, and consequently the validity of the composition profiles he calculated is questionable. In the development of the continuum description of diffuse interface theory [17] positive gradient energy coefficients were assumed. Therefore it would not be possible to calculate composition profiles by applying continuum diffuse interface theory in the alloy system which has a negative gradient energy coefficient for composition. In the Fe-Al system the gradient

energy coefficients for the B2 and the DO_3 ordering, K_{η_1} and K_{η_2} have positive values and the gradient energy coefficient for composition K_c has a negative value as calculated in Chapter 2 of this study.

To calculate the exact profiles of the composition and order parameters of APBs in the B2 or the DO_3 ordered Fe-Al alloys where K_{η_1} and K_{η_2} are positive and K_c negative, a discrete lattice approach similar to the one Cook et al. [25] used when they studied the atomic diffusion at the early stage of ordering where K_c was negative should be used. The preliminary work on this problem is in progress [72].

Although the composition profiles of APBs in the Fe-Al ordered alloys can not be calculated using continuum diffuse interface theory, we can calculate the approximate order parameter profiles and energies of these APBs from the continuum diffuse interface theory if we assume that the composition does not vary across the APBs. These approximate calculations are valuable at this point because exact composition profiles have not been calculated in the Fe-Al system yet. Furthermore, this assumption of no composition variation is very reasonable in our study of APB migration kinetics because our experimental results in Chapter 3 show that most APBs migrate intrinsically without any solute drag effect, indicating negligible composition variation at APBs. If the composition variation at the APBs is thermodynamically favorable, true APB energies would be lower than that calculated by assuming no composition variation at the same temperature and composition.

4.1 Theory of Diffuse Interfaces for More than One Parameter.

In the development of the diffuse interface theory, Cahn and Hilliard expanded the free energy function in a Taylor series about the free energy of a uniform solution. This required that the free energy be a continuous function of its dependent variables, limiting the application of the theory to systems where the free energy can be described in a continuous manner. Physically, this requirement is often met when the two phases have similar atomic structures. The phases which exist in the Fe-rich portion of the Fe-Al binary system (A2, B2, DO_3) are all very similar being derived from the b.c.c. structure, since they undergo continuous transformations from ordered to disordered states.

By using a truncated version of the free energy expansion, Cahn and Hilliard developed a continuum expression for the free energy of a diffuse interface for one and two parameters. When two parameters were considered, cross terms involving the gradient energies were neglected.

When we consider the APBs in single phase paramagnetic B2 or DO_3 phases, up to three parameters may be involved: the first nearest neighbor order parameter η_1, the second nearest neighbor order parameter η_2, and the composition c. If we assume that the composition remains constant across the APBs, the interfacial free energy is then given by:

$$\sigma = \int_{-\infty}^{\infty} \{ \Delta f(\eta_1, \eta_2, c) + K_{\eta_1}(\frac{d\eta_1}{dx})^2 + K_{\eta_2}(\frac{d\eta_2}{dx})^2 \} dx \qquad (4\text{-}1)$$

where x is the distance through the boundary, Δf is given by [73]:

$$\Delta f(\eta_1,\eta_2,c) = \Delta F(\eta_1,\eta_2,c) - \Delta F(\eta_{1e},\eta_{2e},c) - (\frac{\partial \Delta F}{\partial \eta_1})_{\eta_{1e}} (\eta_1 - \eta_{1e})$$

$$- \left(\frac{\partial \Delta F}{\partial \eta_2}\right)_{\eta_{2e}} (\eta_2 - \eta_{2e}) \qquad (4\text{-}2)$$

ΔF is the total free energy with respect to the pure components given by Equation (2-3), and K_{η_1} and K_{η_2} are the gradient coefficients for order parameters η_1 and η_2 respectively. η_{1e} and η_{2e} are equilibrium order parameters for given composition and temperature, and these equilibrium order parameters are defined by following equations:

$$\left(\frac{\partial \Delta F}{\partial \eta_1}\right)_{\eta_{1e}} = 0 \qquad (4\text{-}3)$$

$$\left(\frac{\partial \Delta F}{\partial \eta_2}\right)_{\eta_{2e}} = 0 \qquad (4\text{-}4)$$

Equation (4-2) can be simplified as:

$$\Delta f(\eta_1, \eta_2, c) = \Delta F(\eta_1, \eta_2, c) - \Delta F(\eta_{1e}, \eta_{2e}, c) \qquad (4\text{-}5)$$

Equation (4-1) is specifically for a flat interface. The thermal APBs produced by order transformation are curved, and the expression for the interfacial energy is therefore approximate. However, as long as the radius of curvature of the APB is large relative to the thickness of the APB, this approximation is adequate.

4.2 Minimization of the Interfacial Free Energy.

The variations of order parameters which describe the actual profile in the interfacial region of an APB are those which minimize the interfacial energy. Since the interfacial energy is represented as an integral, it becomes necessary to determine mathematically stationary values of the integral, which are minima in σ. This is done by finding sets of functions $\eta_1(x)$, $\eta_2(x)$ which give stationary values of the integral. These functions are found by solving the Euler equations, one for each independent variable. The general form of Euler equation is given by [74]:

$$\frac{\partial I}{\partial z} - \frac{d}{dx}\left(\frac{dI}{dz'}\right) = 0 \qquad (4\text{-}6)$$

where I is the integrand, z the independent variable, and x the distance from the center of the APB.

The set of Euler equations for the integral in Equation (4-1) is:

$$\frac{\partial \Delta f}{\partial \eta_1} = 2K_{\eta_1}\frac{d^2\eta_1}{dx^2} \qquad (4\text{-}7)$$

$$\frac{\partial \Delta f}{\partial \eta_2} = 2K_{\eta_2}\frac{d^2\eta_2}{dx^2} \qquad (4\text{-}8)$$

The expression on the left side of each equation is an algebraic expression which can be determined by applying Equation (2-3) to the expression for Δf given by Equation (4-5) and then performing the partial differentiation. The equations (4-7) and (4-8) are then coupled second-order ordinary differential equations in x, and each equation requires two boundary conditions to specify a solution.

For the <111> APBs in the B2 phase, η_2 is zero and Equation (4-7)

is the only equation to solve. Since the $+\eta_1$ state is physically identical to the $-\eta_1$ state, all the solutions to the Euler equation must be symmetric about $\eta = 0$ for a flat interface. One boundary condition for equation (4-7) can be specified at $x = \infty$. The second boundary condition can be specified at x = 0, which, by definition, is the point at which $\eta_1 = 0$. These boundary conditions are $\eta_1 = \eta_{1e}$ at $x = \infty$, and $\eta_1 = 0$ at x = 0.

For the <100> APBs in the DO_3 phase, two different order parameters η_1 and η_2 should be considered and two coupled equations (4-7) and (4-8) should be solved simultaneously. In this case we need two boundary conditions for each equation. The boundary condition of $\eta_2 = \eta_{2e}$ at $x = \infty$, and $\eta_2 = 0$ at x = 0 can be derived from the same argument discussed in the previous paragraph for <111> APBs in the B2 phase. For the variable η_1, the boundary condition of $x = \infty$ is $\eta_1 = \eta_{1e}$, this value being determined by thermodynamic equilibrium. Near x = 0, η_1 may also have non-equilibrium values. However, the value of η_1 at x = 0 is not determined by any specific physical requirements, only that the value results in an overall minimum in the interfacial free energy. The process by which the proper boundary conditions for η_1 is obtained is to determine natural boundary condition at x=0 for η_1. Using the method described by Krzanowski [20], the boundary condition becomes:

$$\frac{d\eta_1}{dx} = 0 \qquad \text{at } x = 0 \tag{4-9}$$

In actual calculation of η_2 profiles and energies of <100> APBs in the DO_3 phase, we assumed constant η_1 having the η_{1e} value across the <100> APBs. This is a trivial solution to Equation (4-7) since η_1 does not vary with x. A simple justification for this assumption is that the

<100> APBs in the DO_3 phase are formed inside the domains separated by <111> APBs inherent to the B2 phase where η_1 has the equilibrium value η_{1e}. Nonetheless, it is possible that non-trivial solutions for the case in which $\eta_1(x)$ is non-uniform do exist.

4.3 Calculations of Interfacial Profiles and Energies.

The application of the theory of diffuse interfaces to the APBs in Section 4.1 resulted in the Euler equations which need to be solved for the interfacial profiles. These profiles need to be determined in order to compute the interfacial energy. Due to the complexity of the Euler equations, it will be necessary to compute numerical solutions. This complexity arises due to the form of the left sides of Equations (4-7) and (4-8). The derivatives of Δf are given by:

$$\frac{\partial \Delta f}{\partial \eta_1} = \frac{Nk_B}{2}\left[2\left(\frac{V(\vec{k}_1)}{k_B}\right)\eta_1 + T\{\ln\frac{(1-c+\eta_1)}{(c-\eta_1)} + \frac{1}{2}\ln\frac{(c+\eta_1+\eta_2)(c+\eta_1+\eta_2)}{(1-c-\eta_1-\eta_2)(1-c-\eta_1+\eta_2)}\}\right] \tag{4-10}$$

$$\frac{\partial \Delta f}{\partial \eta_2} = \frac{Nk_B}{2}\left[\frac{V(\vec{k}_2)}{k_B}\eta_2 + \frac{T}{2}\{\ln\frac{(1-c-\eta_1+\eta_2)(c+\eta_1+\eta_2)}{(1-c-\eta_1-\eta_2)(c+\eta_1-\eta_2)}\}\right] \tag{4-11}$$

To solve for the profiles of <111> APBs in the B2 phase, only Equation (4-7) needs to be solved using Equation (4-10). The boundary conditions are $\eta_1 = \eta_{1e}$ at $x = \infty$, and $\eta_1 = 0$ at $x = 0$. To solve for the profiles of <100> APBs in the DO_3 phase, Equation (4-8) needs to be solved using Equation (4-11) with a constant value of η_{1e} for η_1 at given temperature and composition.

For actual calculation of these profiles, NAG Fortran library subroutines C05NBF and D02HAF were used [75]. C05NBF was used to calculate the equilibrium order parameters η_{1e} and η_{2e} at given temperatures and compositions from Equations (2-9) and (2-10). In order to use D02HAF to solve Equations (4-7) and (4-8), these equations were rewritten in the following forms:

$$\frac{d\eta_1}{dx} = \eta_{1P} \tag{4-12}$$

$$\frac{d\eta_{1P}}{dx} = \frac{1}{2K_{\eta_1}} \frac{\partial \Delta f}{\partial \eta_1} \tag{4-13}$$

$$\frac{d\eta_2}{dx} = \eta_{2P} \tag{4-14}$$

$$\frac{d\eta_{2P}}{dx} = \frac{1}{2K_{\eta_2}} \frac{\partial \Delta f}{\partial \eta_2} \tag{4-15}$$

Then we have a two-point boundary-value problem for two ordinary differential equations which can be solved using the Newton iteration in a shooting and matching technique in D02HAF subroutine.

Once we get the profiles of η_1 and η_2 for the APBs, we can calculate the energies of these APBs by numerical integration of Equation (4-1).

A description and listing of a sample computer program to calculate the APB profiles and the energies is given in Appendix D.

4.4 Results

Calculations were done in the single-phase B2 and the single phase DO_3 regions above the Curie temperatures in the composition range from Fe-24%Al to Fe-28%Al. A planar APB in an infinite system was assumed to be stationary and at thermodynamic equilibrium.

Figure (4-1) shows the calculated equilibrium order parameters η_{1e} and η_{2e} as functions of the temperature in the Fe-26%Al alloy. η_{1max} and η_{2max} are maximum theoretical order parameters for the first nearest neighbor and the second nearest neighbor ordering respectively, and for Fe-26%Al, η_{1max}=0.26 and η_{2max} = 0.48. The changes of η_{1e}/η_{1max} and η_{2e}/η_{2max} with respect to T/T_c showed typical characteristics of the higher-order phase transition. η/η_{max} values decrease continuously to zero as the temperature reaches the critical temperature. The critical temperatures T_c are 1096K for A2→B2 and 826K for B2→DO_3 respectively for the Fe-26%Al alloy.

Figure (4-2) shows the calculated order parameter profiles of the <111> APBs in the B2 phases for the Fe-24%Al alloy. Only one-half of the profiles are plotted due to the symmetry of the structure. As the temperature increases, the profile becomes more diffuse with lower η_{1e} value. Profiles of the <100> APBs in the DO_3 phase have also been calculated and the general characteristics are very similar to those of the <111> APBs in the B2 phase.

The diffuseness of the APBs can be expressed by the thickness of the APBs defined as:

$$\delta_\eta = \frac{2\eta_e}{(d\eta/dx)_{x=0}} \qquad (4\text{-}16)$$

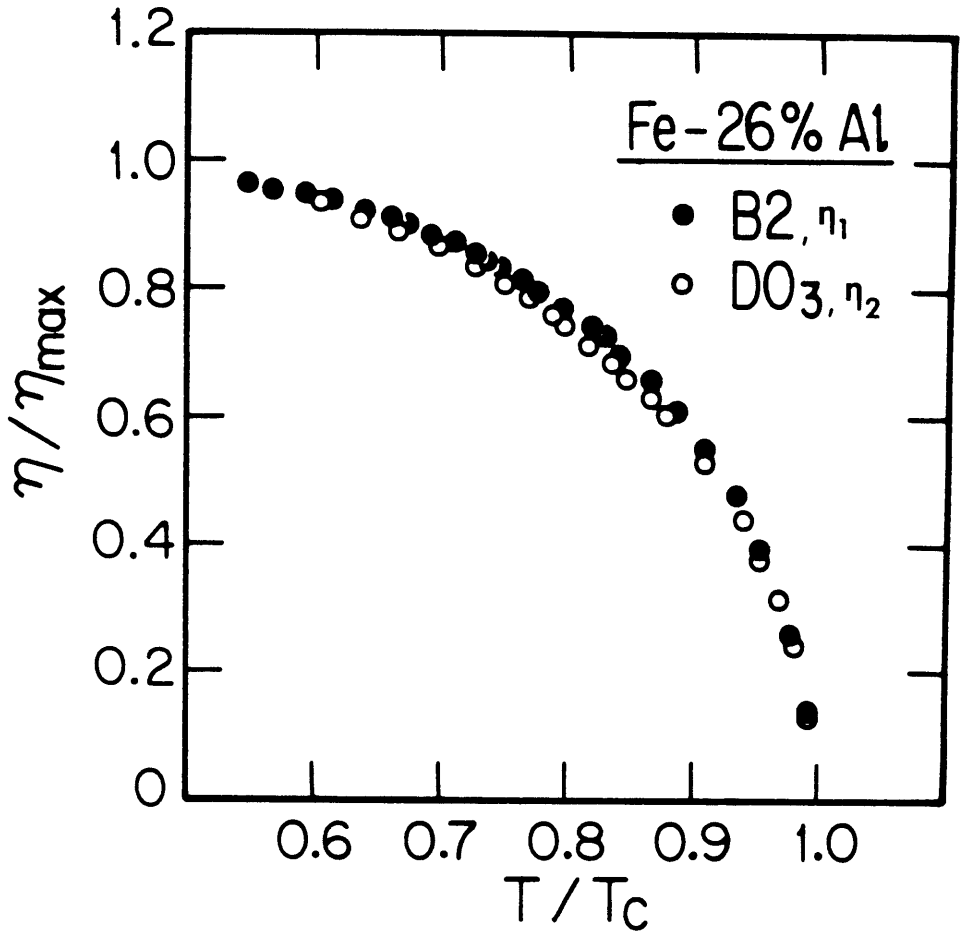

Figure (4-1) Changes of η_e/η_{emax} for η_1 and η_2 in the B2 and the DO_3 phases respectively for the Fe-26%Al alloy. X axis is plotted as the reduced temperature T/T_C where T_C=1096K for A2→B2 and T_C=826K for B2→DO_3. Both η_{1e} and η_{2e} show the typical characteristics of the higher order phase transformation.

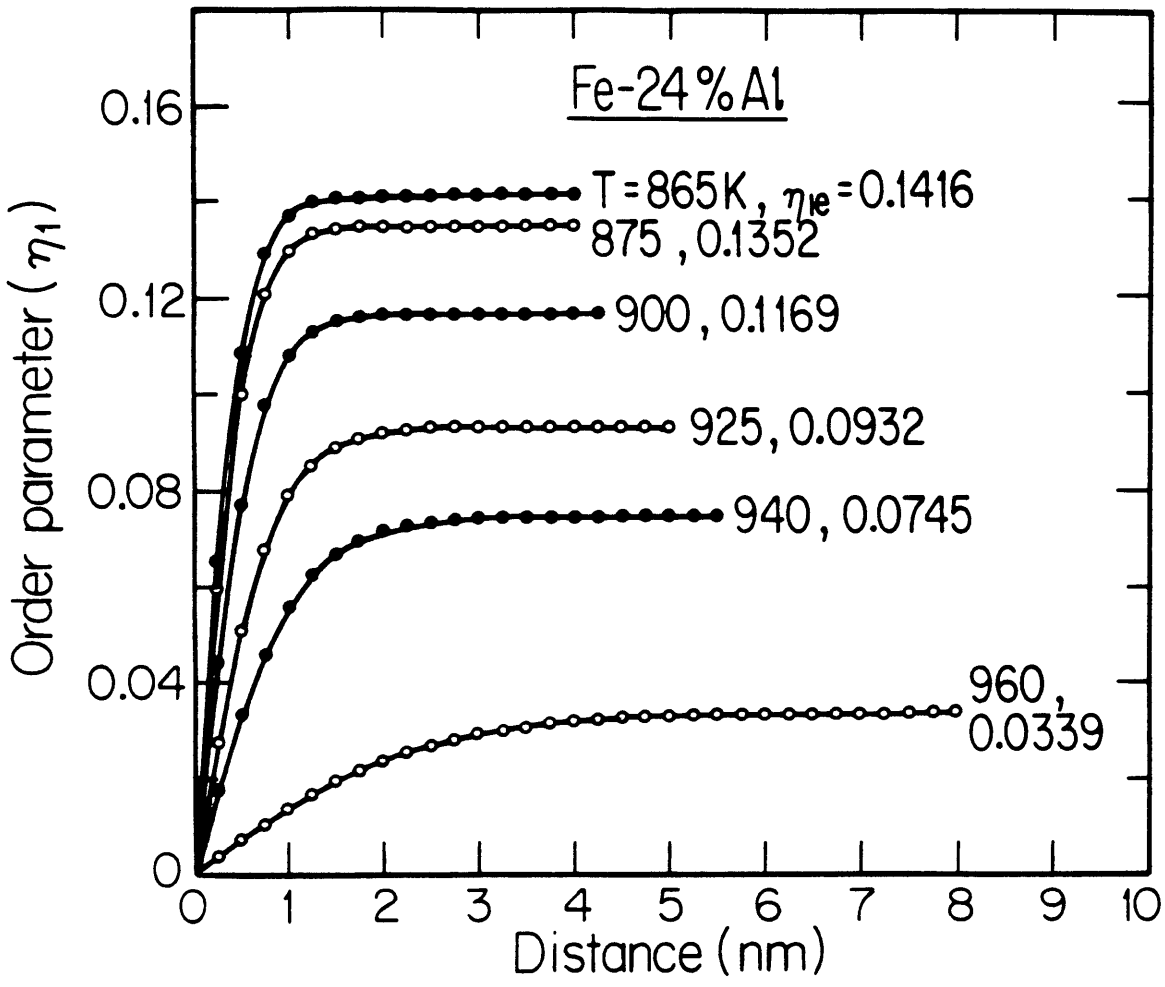

Figure (4-2) Calculated profiles of the order parameter η_1 at <111> APBs in the Fe-24%Al alloy. Due to the symmetry of the structure, only one-half of the interfaces are shown. T_c= 965K.

This relation computes twice the distance at which the extrapolation of the slope of the $\eta(x)$ profile at x = 0 intersects the value of the equilibrium order parameter. The thicknesses of the <111>APBs and the <100>APBs in the B2 and the DO_3 phases respectively for the Fe-26%Al alloy were plotted in Figure (4-3). At the same T/T_c, the <100> APBs in the DO_3 phase are a little more diffuse than the <111> APBs in the B2 phase. When T/T_c is less than 0.7, δ_{η_1} and δ_{η_2} are less than 0.7nm which is less than three times the lattice parameter of the B2 phase. Thus, for temperatures lower than $0.7T_c$ the APBs are not very diffuse in the order parameter profile, and the application of the theory of diffuse interfaces in calculating the profile and the energy of the APBs will not be plausible.

Cahn and Hilliard [17] showed that when the interfacial energy is a function of only a single variable, the value of $(d\eta/dx)_{x=0}$ is given by:

$$\frac{d\eta}{dx} = \sqrt{\frac{\Delta f_{max}}{K_\eta}} \tag{4-17}$$

where Δf_{max} is given by $\Delta f(\eta_e) - \Delta f(0)$. The interfacial thickness is then given by:

$$\delta_\eta = 2\eta_e \sqrt{\frac{K_\eta}{\Delta f_{max}}} \tag{4-18}$$

The calculation of δ_η using Equation (4-18) showed excellent agreement with numerical solutions plotted in Figure (4-3). The APB energies for the <111> APBs, σ_{111}, and <100> APBs, σ_{100}, in the Fe-26%Al alloy were plotted in Figure (4-4).

As expected, σ decreases as the temperature increases for both types

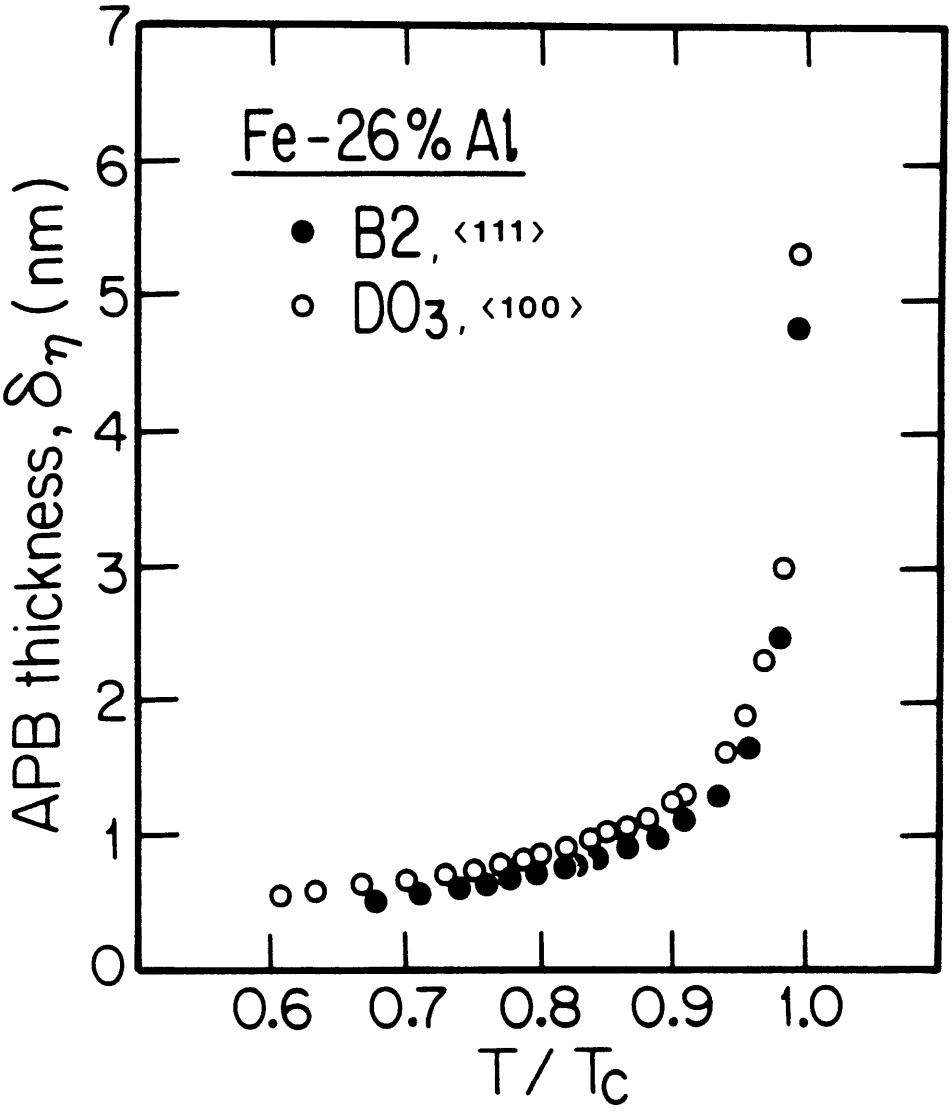

Figure (4-3) Changes of the thickness of <111> APBs and <100> APBs in B2 and DO_3 phases respectively with T/T_c for Fe-26%Al alloy.

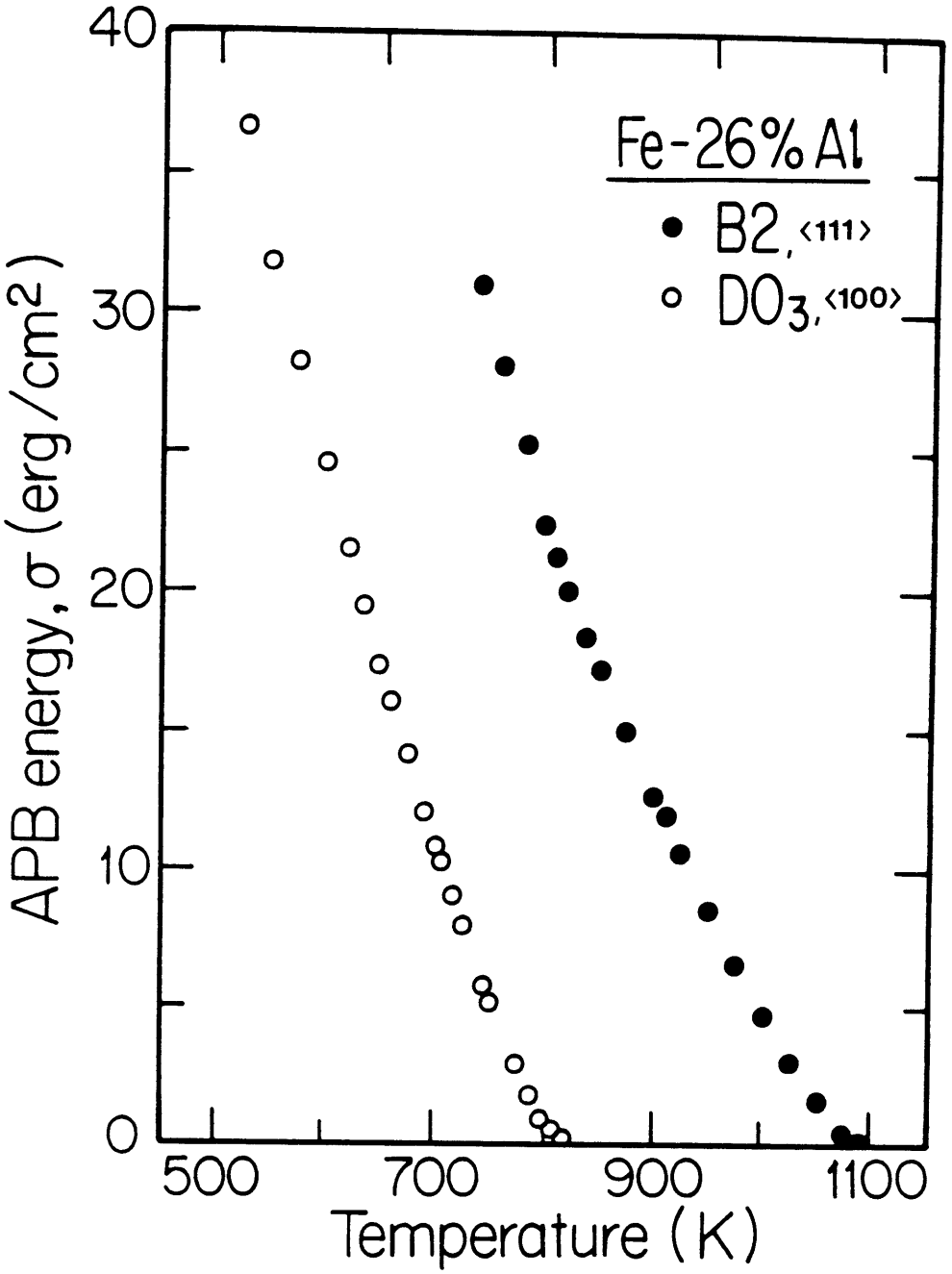

Figure (4-4) Calculated values for APB energy σ (erg/cm^2) for <111> APBs and <100> APBs in the Fe-26%Al.

of APBs, becoming zero at their respective critical temperatures. The excess entropy of the APBs in the limit of approach to the critical temperatures is expected to become zero [76]. If this is the case, σ vs. T plot should have zero slope at the critical temperature. Figure (4-5) shows the σ vs. T plot of the <111> APBs near $T_c(A2 \rightarrow B2)$ for the same alloy. This plot shows the slope decreasing to zero as the temperature reaches the critical temperature. The calculated interfacial energies of the <100> APBs near $T_c(B2 \rightarrow DO_3)$ showed similar behavior.

<111> APB energies in the Fe-25%Al and the Fe-28%Al alloys were plotted along with the <111> APB energies in the Fe-26%Al alloys in Figure (4-6). At a given temperature, σ_{111} increases as the aluminum content increases. σ_{111} would have a maximum around the composition of Fe-50%Al where the equilibrium order parameter is the maximum for a given temperature. In Figure (4-7), σ_{111} vs. η_{1e} were plotted for the Fe-25%Al and the Fe-28%Al alloys. In this plot, σ_{111}, has a higher value in the Fe-25%Al alloy for a given equilibrium order parameter η_{1e}.

<100> APB energies in the Fe-25%Al and the Fe-28%Al alloys were plotted in Figure (4-8). σ_{100} in the Fe-25%Al has a higher value than that in the Fe-28%Al for a given temperature. σ_{100} decreases as the aluminum content increases above Fe-25%Al which is the stoichiometric composition for the DO_3 structure. In Figure (4-9), σ_{100} vs. η_{2e} were plotted for the Fe-25%Al and the Fe-28%Al alloys. In Figure (4-7) and Figure (4-9), σ_{111} and σ_{100} become zero asymptotically as the order parameters η_{1e} and η_{2e} become zero respectively.

As a rough check on the APB energies calculated here, the results can be compared to the experimental measurements of APB energies in Fe-Al

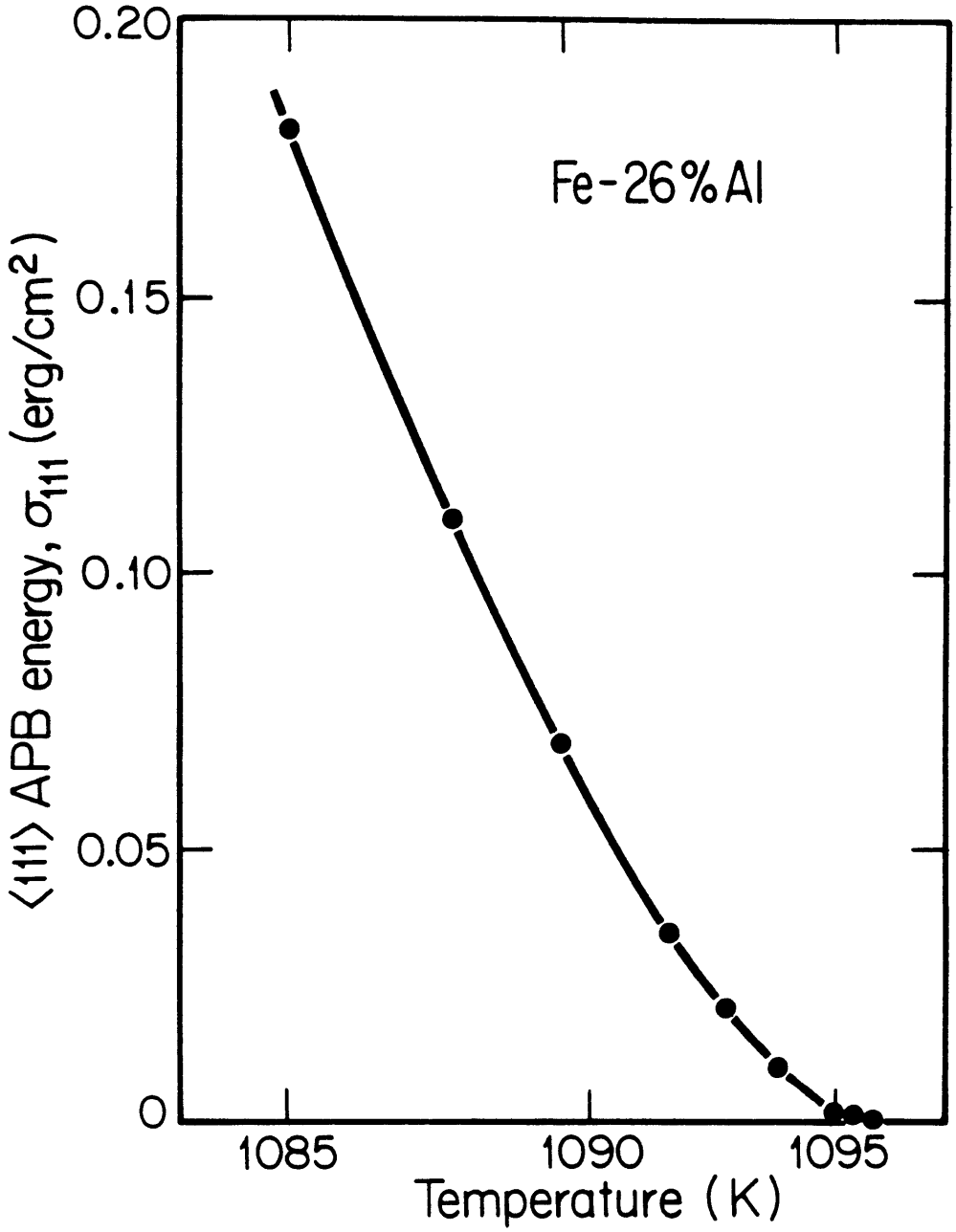

Figure (4-5) <111> APB energy, σ_{111}, in the Fe-26%Al near the critical temperature T_c=1096K. It shows the decreasing slope which becomes zero as the temperature reaches the critcal temperature.

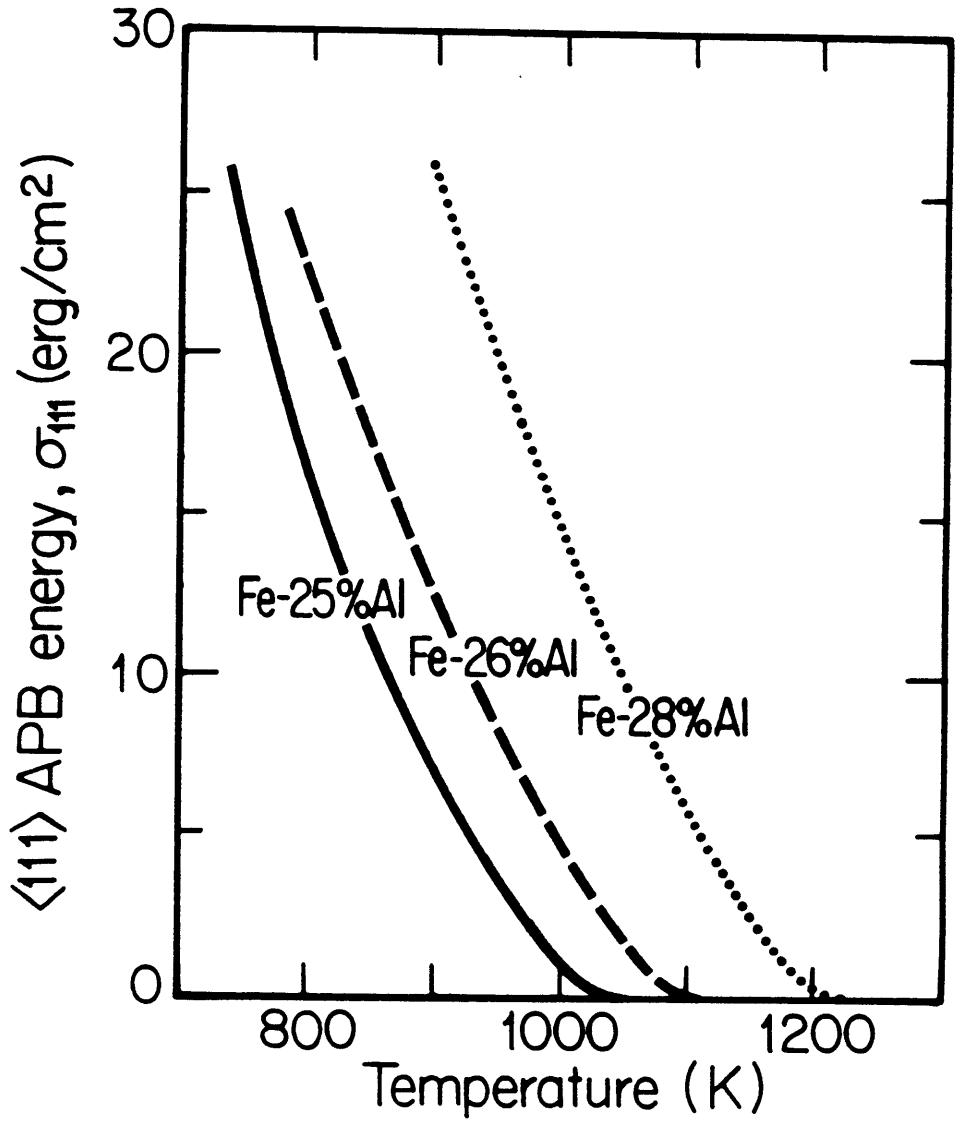

Figure (4-6) <111> APB energy σ_{111} for Fe-25%Al, Fe-26%Al and Fe-28%Al alloys.

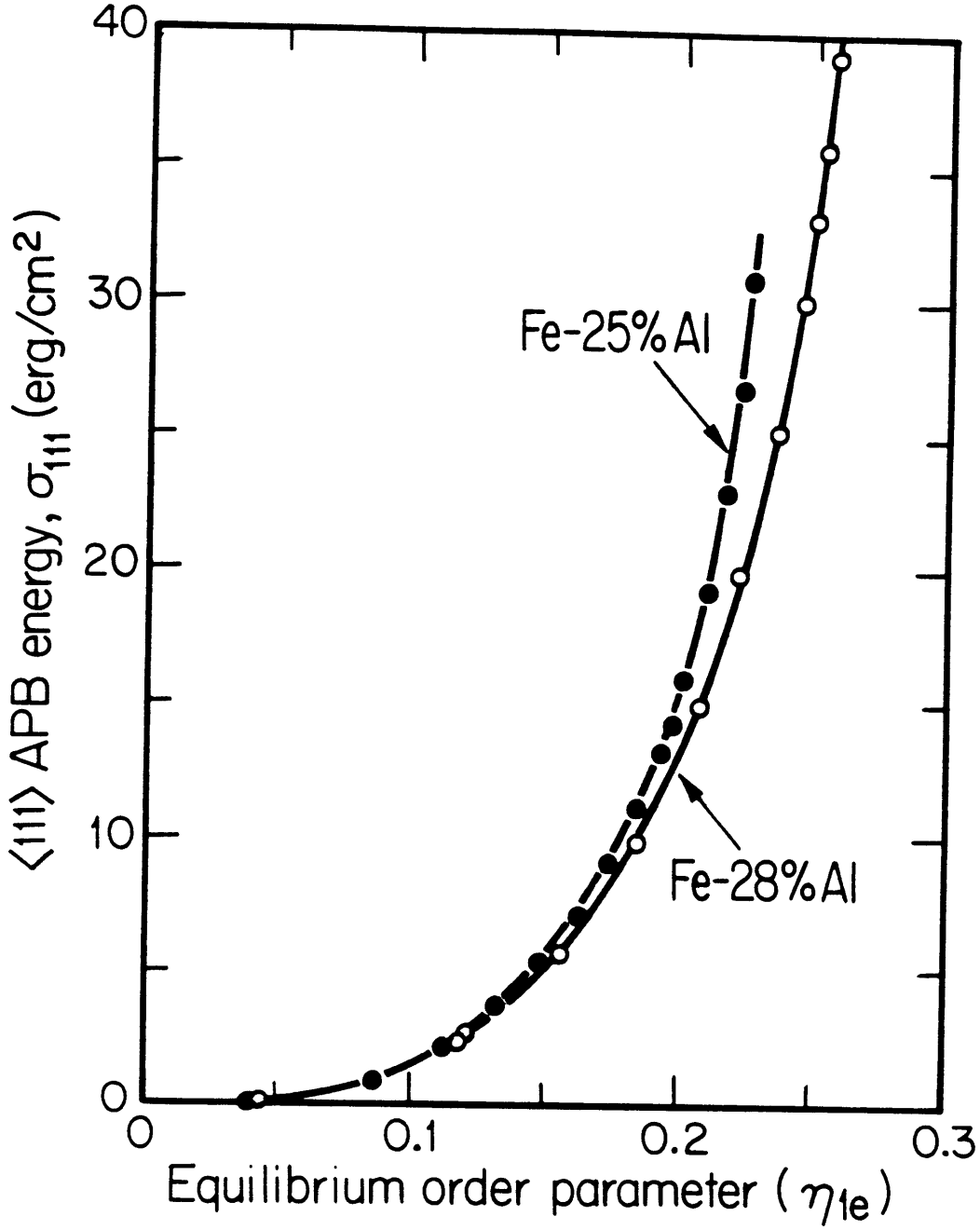

Figure (4-7) <111> APB energy σ_{111} for Fe-25%Al and Fe-28%Al plotted as functions of the equilibrium order parameter η_{1e}.

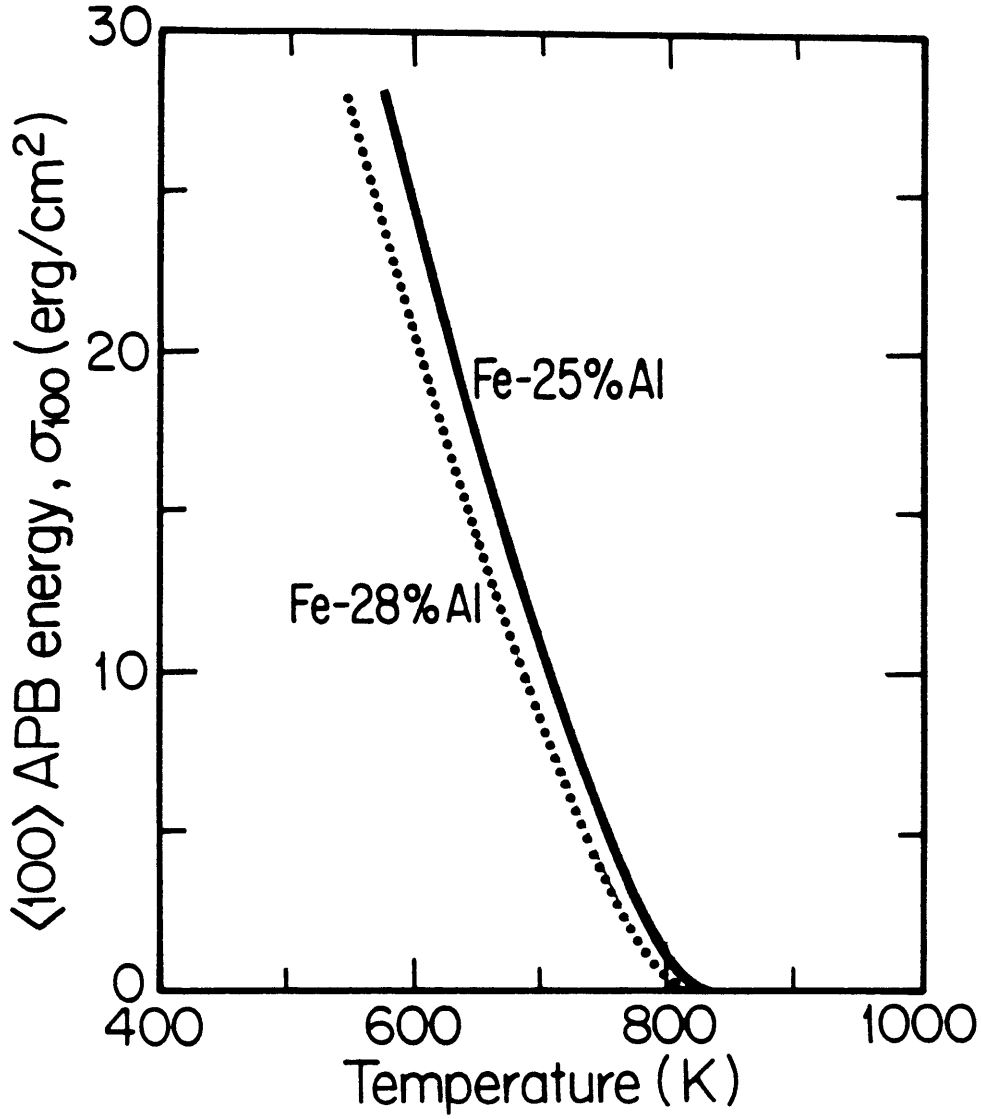

Figure (4-8) <100> APB energy σ_{100} for Fe-25%Al and Fe-28%Al alloys.

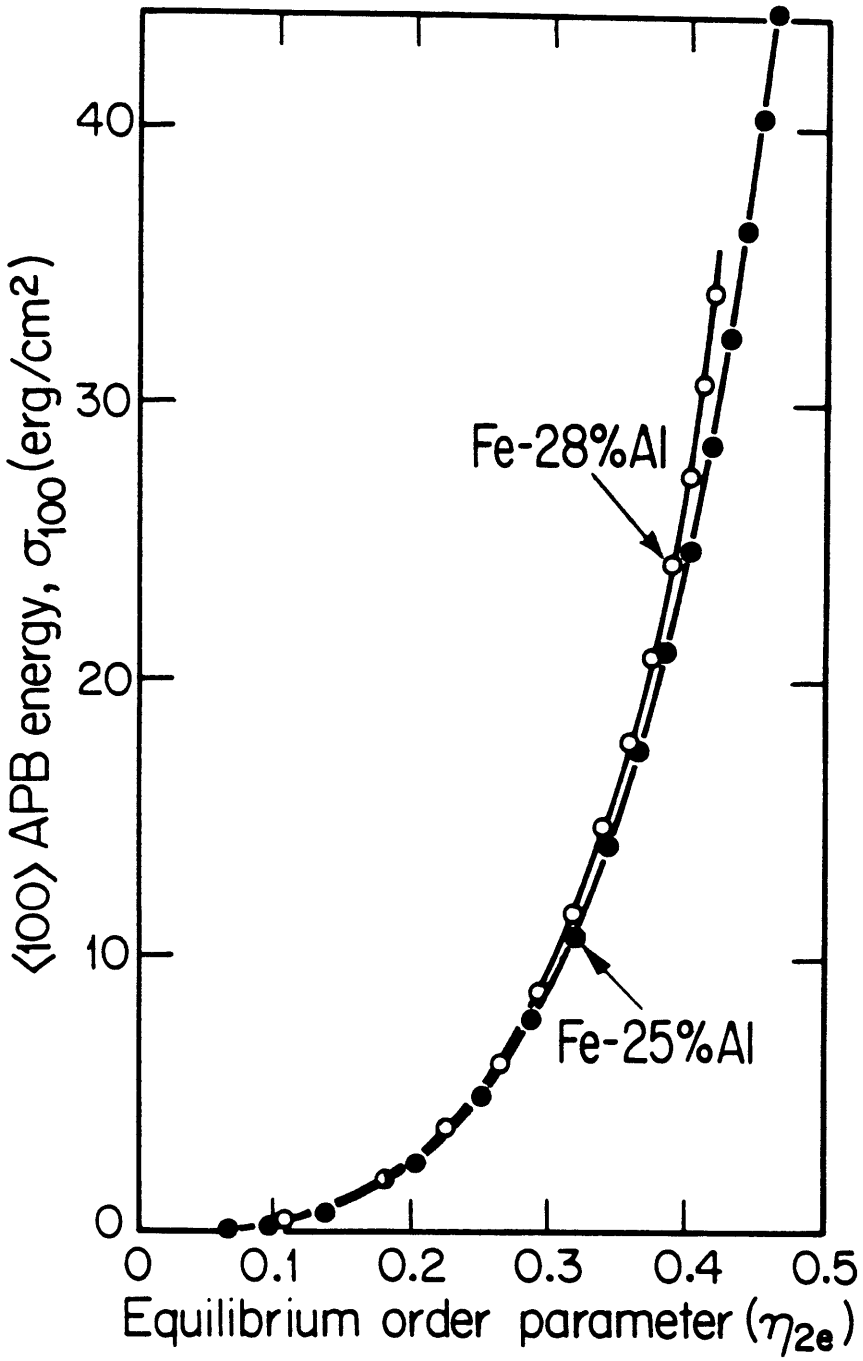

Figure (4-9) <100> APB energy σ_{100} for Fe-25%Al and Fe-28%Al plotted as functions of the equilibrium order parameter η_{2e}

alloys made by Crawford and Ray [66]. They measured the separation distances of dissociated superlattice dislocations in the B2 and the DO_3 phases in order to determine the APB energies. Experimental results were obtained for alloys of 26.9 to 35.8%Al which were slowly cooled to room temperature. Thus, their values for APB energies were not given as functions of temperature. But their results showed that σ_{111} increases and σ_{100} decreases as the aluminum content increases. The magnitudes of their room temperature values for σ_{111} and σ_{100}, which is around $60 \simeq 80$ erg/cm^2, seem to be compatible with our high temperature values of these APB energies.

Krzanowski calculated σ_{111} for the Fe-Al alloys of 24% and 25% Al at high temperatures in the B2 phase using a simple Bragg-Williams model and the diffuse interface theory [20]. The calculated value for σ_{111} at 860K was 4.23 erg/cm^2 for 24%Al and 6.41 erg/cm^2 for 25%Al. Our calculation gives σ_{111} = 10.6 erg/cm^2 at 860K for 25%Al. Thus, his results gave similar magnitudes for the APB energies.

From these energy calculations we can check the validity of our assumption of the negligible surface grooving at the intersection of the APBs with the surface in thin-foil in-situ TEM experiments. Calculated APB energies corresponding to our experimental conditions (temperature and composition) range from 1 mJ/m^2 to 20 mJ/m^2 whereas the surface energy is usually in the order of $1 \simeq 2$ J/m^2 (1 erg/cm^2 = 1 mJ/m^2). Thus the assumption of minimal surface grooving is valid in our experiments in Chapter 3.

It would be of interest to compare the change in APB energy with composition at a constant temperature with the corresponding change in

the mobility M. The intrinsic mobility of <111>APBs in the Fe-26%Al alloy at 910K was determined to be 1.5×10^{-16} m^2/s in our experimental study in Chapter 3. Allen and Cahn [18] reported that $M\phi = 1.1 \times 10^{-16}$ m^2/s for <111>APB migration in the Fe-24%Al alloy at 904K. If we use a value of $\phi = 0.5$ (as calculated in Chapter 3), M is 2×10^{-16} m^2/s for <111>APBs in the Fe-24%Al alloy at 904K. The intrinsic mobilities M for both the Fe-24%Al and Fe-26%Al alloys are very similar in magnitude at the same temperature. On the other hand, APB energies σ for these alloys at 910K are quite different. According to our calculation, $\sigma = 2$ erg/cm^2 for <111>APBs in the Fe-24%Al and $\sigma = 12$ erg/cm^2 for <111>APBs in the Fe-26%Al at 910K. It is quite obvious that the difference in σ is not reflected in the intrinsic mobility M of these APBs.

This agrees well with the APB migration theory of Allen and Cahn [18] which states that the intrinsic mobility is expressed by Equation (1-13) and does not include the interfacial energy term. At a given temperature, the interdiffusion coefficient in the Fe-Al system is not a strong function of composition [63]. Therefore, the intrinsic mobility, whose thermal activation energy is very similar to that of the interdiffusion, would be similar for different compositions at the same temperature.

CHAPTER 5

CONCLUSIONS

The following conclusions have been drawn from this work.

1. Studies of bulk antiphase domain coarsening kinetics indicate that there is a solute drag effect when the driving force is small. Transistions from the high velocity extreme to the low velocity extreme were observed as the <100> domains coarsened in the DO_3 phase of the Fe-26%Al alloy. Average domain sizes at the transition points indicate that most of the in-situ experiments were carried out in the high velocity extreme, thus leading to measurements of the intrinsic mobility M.

2. In-situ hot-stage transmission electron microscopy has been proven to be valuable in studying the migration kinetics of antiphase boundaries (APBs) in Fe-Al ordered alloys. A two-dimensional approximation of the complicated three-dimensional morphology of the APBs made it possible to determine the mobility of the APBs, which is the proportionality constant relating the velocity to the local curvature.

3. The intrinsic mobility, M, of the APBs has been determined experimentally, for the first time, employing in-situ hot-stage TEM. M for <111> APBs in the B2 phase of the Fe-26%Al alloy has values ranging from 1.7×10^{-17} (m^2/s) to 1.5×10^{-16} (m^2/s) for temperatures from 838K to 910K. M for <100> APBs in the DO_3 phase of the same alloy is in the range 4.8×10^{-19} (m^2/s) to 4.7×10^{-18} (m^2/s) for temperatures from

745K to 800K.

4. <111> APBs in the B2 phase and <100> APBs in the DO_3 phase in the Fe-26%Al alloy migrate intrinsically without any noticeable solute drag effect when the curvature is larger than K = $1x10^7$ (m^{-1}). When the curvature is smaller than $1x10^7$ (m^{-1}), there was a tendency toward reduced mobility indicating possible extrinsic behavior due to a solute drag effect.

5. From the temperature dependence of the mobility, the activation energy required for APB migration has been determined. For both the <111> APBs and <100> APBs, this activation energy has almost the same value as the activation energy for interdiffusion in the disordered A2 phase of the Fe-Al system.

6. The Bragg-Williams model has been improved to give a better match between the calculated and the experimental phase diagram of the Fe-Al system. This has been achieved by considering up to third nearest neighbor interactions and composition dependent interaction energies which are calculated from the experimental phase diagram.

7. Using the improved Bragg-Williams model, the gradient energy coefficients K_{η_1}, K_{η_2}, K_c which are for the order parameters η_1 and η_2 and the composition, respectively, have been derived for the Fe-Al system. K_{η_1} and K_{η_2} have positive values, but K_c has a negative value which is consistent with the known fact that the Fe-Al system tends to order.

8. Due to the negative value of K_c, it is not possible to use a continuum description of diffuse interface theory to compute possible composition variations at APBs. A discrete lattice formulation approach is suggested to solve this problem.

9. Assuming no composition variation at APBs, the order parameter profiles and the energies of APBs in the Fe-Al ordered alloys can be calculated approximately using diffuse interface theory. Calculated results are comparable to those obtained in previous work and show good agreement with expected trends resulting from changes of temperature and composition.

CHAPTER 6

SUGGESTIONS FOR FUTURE WORK

The following points, which have arisen from the results of this thesis investigation, could be pursued further.

1. In order to calculate the composition variation at the APBs which is needed for the solute drag effect calculation, a discrete lattice formulation should be developed which is capable of dealing with both positive and negative gradient energy coefficients.

2. Throughout the current research, the APBs were assumed to be isotropic, a very reasonable assumption at elevated temperatures of $T > 0.7T_c$ in the Fe-Al system. But there have been some experimental observations of APB morphologies in Fe-Al alloys which show evidence of anisotropy of the interfacial free energy. It is believed that the elastic strain energy plays a significant role in determining excess free energies of APBs under some conditions. To study this problem, we should incorporate elastic strain energy effects in describing the free energy of an inhomogeneous system containing an APB. This can be achieved by allowing for the variation of the lattice constant with the composition and order parameter. We can then use a continuum formulation which is similar to the one used in the theory of spinodal decomposition, where both profiles $c(x)$ and $\eta(x)$ give rise to elastic strain energy contributions to the free energy. But a discrete lattice formulation which can handle the elastic energy contribution, as well as the negative value of K_c,

would be most desirable to attack these problems simultaneously.

3. It would be worthwhile to study ternary Fe-Al-X alloys, where "X" is an element that segregates strongly to APBs. Such segregation should be marked in systems in which "X" additions markedly change the order-disorder transition temperatures relative to those for binary Fe-Al alloys [78]. If we have strong solute drag forces on the migrating APBs in these ternary alloys, the "break-away" regime will be clearly observed in in-situ hot-stage TEM experiments. Additions of these "X" elements also tend to make the APB more anisotropic, and the combined effects of the anisotropy and segregation could then be studied. Additions of 5%Ti to Fe-25%Al substituting for Fe, is known to cause dramatic anisotropic APB morphologies to develop, and Ti is an addition that significantly raises the order-disorder transition temperature [79].

4. The nature and magnitude of adsorption at APBs have been difficult to quantify experimentally because of the diffuseness of the interfacial regions, particularly in the Fe-Al system, where difficulties with X-ray absorption effects make microanalysis by STEM extremely difficult. But it would be possible to study the structure of APBs by means of atom-probe field-ion microscope. Not only is it be possible to detect and quantify interfacial segregation [80,81], but it is also possible to measure long-range order parameter [82] using the atom probe.

5. Even though we have estimated the range of the values of the topological constant ϕ of the thermal APBs in the Fe-Al system, this

parameter should be studied more carefully. Due to the complexity of the morphology of these APBs, it would not be very easy to determine ϕ experimentally. But, it should be possible to study this problem theoretically because values of ϕ will be set by the random processes that give rise to the ordered domain structure and will not be altered by attempts to adjust the interface shape as the domain coarsens.

APPENDIX A

A-1. Trace Analysis

Exact slip planes are variable for our system. Prior work [67,77] indicated (110), (112), and (123) as possible slip planes for Fe-Al alloys, and degree of order can affect the active slip system. The actual slip planes can be determined using a computer program which employs beam direction, $\hat{B}$, foil normal, $\hat{S}$, a reference direction, R, and a guess for the normal of the slip plane, N.

Beam direction may be determined from the selected area diffraction (SAD) patterns. The surface normal for the sample can be determined from the diffraction pattern taken with all tilts of specimen holder zeroed.

Once $\hat{B}$ and $\hat{S}$ have been determined, the slip plane normal, $\hat{N}$, can determined by trial and error. The {110} family consists of six planes, the {112} family has twelve planes, and the {123} family has twenty-four planes. Forty-two different plane normals have to be tried to get a complete analysis of the potential slip planes. A computer program will be used to do the analysis using the principles shown in Figure A-1.

$\hat{B}$, beam direction, $\hat{S}$, surface normal, R, reference direction, and $\hat{N}$, a guess for the slip plane normal are the input for the program. The program normalizes the vectors and then performs a series of cross products; the first vector product is

$$\vec{T} = \hat{S} \times \hat{N} \qquad \text{(A-1)}$$

$\vec{T}$ is the direction along the line of intersection between a planar defect of normal $\hat{N}$ and the surface of the foil.

To determine where a picture of this defect would lie in the actual micrograph, this direction, $\vec{T}$, must be projected in the plane of the

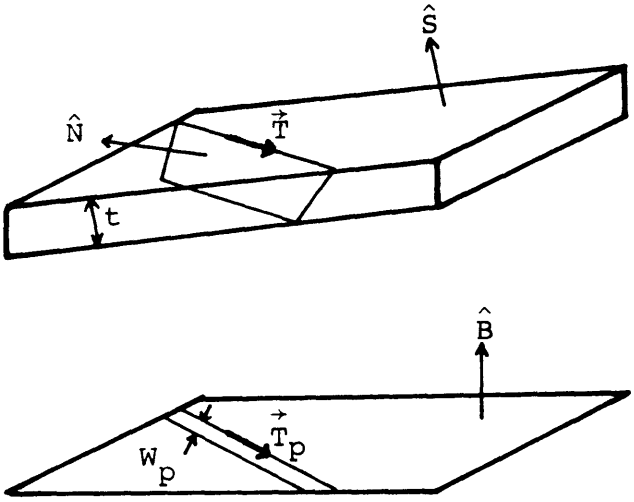

$\vec{T}$ = direction of defect along foil surface, trace
$\hat{S}$ = foil normal
$\hat{N}$ = planar defect normal
$\hat{B}$ = beam direction
$\vec{T}_p$ = projected trace

$\vec{T} = \hat{S}\times\hat{N}$, and $\vec{T}_p = (\vec{T}\times\hat{B})\times\hat{B}$

Figure A-1. Schematic diagram of information necessary for a trace analysis

micrograph. This is done with a triple vector product:

$$\vec{T}_p = (\hat{B} \times \vec{T}) \times \hat{B} \qquad \text{(A-2)}$$

$\vec{T}_p$ gives the direction of the projected trace. The program uses the reference direction to compute the angle between $\vec{R}$ and $\vec{T}_p$. The projected trace can then be sketched on the micrograph (Figure A-2). The reference direction is a direction lying in the plane of the micrograph. This direction is determined with the aid of the pertinent diffraction pattern and the rotation calibration chart for the electron microscope used.

A-2. Projected Width Analysis

After the trace analysis was completed, more than one slip plane had a projected trace that aligned well with the actual trace (Figure A-2). Calculation of projected width that would appear in the micrograph for each well-aligned trace will be done with the formula:

$$W_p = t(\hat{B} \cdot \hat{N})/\left| (\hat{S}x\hat{N})x\hat{B} \right| \qquad \text{(A-3)}$$

From the diffraction patterns, $\hat{B}$ and $\hat{S}$ are known. N is one of the potential slip plane normals. For a given value of thickness t, variation of W_p can be calculated and by comparing these changes in W_p with the micrographs, the actual slip plane normal can be decided. And once actual slip plane is decided, by measuring actual projected width, we can estimate the foil thickness of the sample.

A-3. Separation Analysis

To calculate mobility we must know how far the hyperbolic interfaces have moved. The following analysis should be done to know the real separation distance d from the measured separation distance $d_{s(p)}$.

$\hat{B} = (0.06 \quad 0.66 \quad 0.75)$

near (011) pole

$\bar{1}\bar{1}1$ dark field

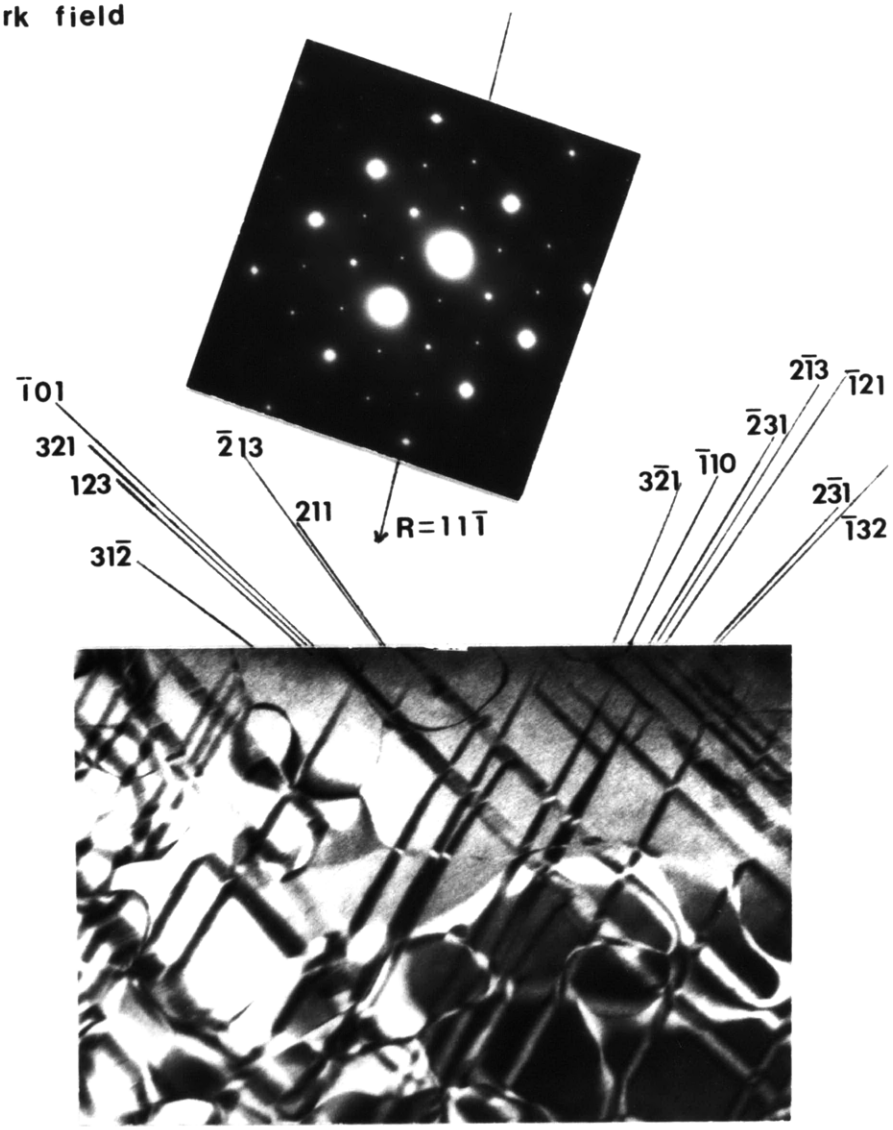

Figure (A-2) Sketch of several T_p lines of possible slip planes with respect to a reference direction $\vec{R}$

Figure A-3 is a schematic diagram of a foil with intersecting planes. As long as the measurement of separation distance is correctly made to represent $d_{s(p)}$, which is the projected length of d_s, the relationship between this $d_{s(p)}$ and real separation d will be independent of the foil thickness. The relationship is given by:

$$d = \frac{d_{s(p)} |\hat{U}_s \cdot \hat{U}_d|}{|\hat{U}_s \times \hat{B}|} \tag{A-4}$$

where $\hat{S}$ = surface normal

$\hat{B}$ = beam direction

$\hat{N}_1$, $\hat{N}_2$ = two slip plane normals (sign of these normals decided so that the direction of separation is parallel to $\hat{N}_1 + \hat{N}_2$)

$\hat{U}_d$ = unit vector along the direction of d (real separation direction

$$\hat{U}_s = \frac{\hat{S} \times (\hat{N}_1 - \hat{N}_2)}{|\hat{S} \times (\hat{N}_1 - \hat{N}_2)|}$$

$$\hat{U}_d = \frac{(\hat{N}_1 \times \hat{N}_2)(\hat{N}_1 - \hat{N}_2)}{|(\hat{N}_1 \times \hat{N}_2) \times (\hat{N}_1 - \hat{N}_2)|} = \frac{\hat{N}_1 + \hat{N}_2}{|\hat{N}_1 + \hat{N}_2|}$$

Two different kinds of APB intersection images are possible, and for each kind, measurement of $d_{s(p)}$ should be done differently. This is schematically represented in Figure A-4. Once the slip planes are known, we can determine which of the two kinds is the case with the aid of stereographic projection.

A-4. Mobility Determination

Equation (3-1) gives the distance migrated by hyperbolic APBs as:

$$R(0,t) = \{2Mf(\alpha)t\}^{\frac{1}{2}}$$

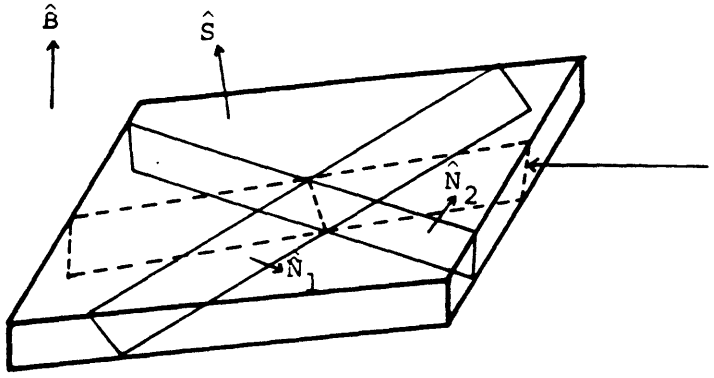

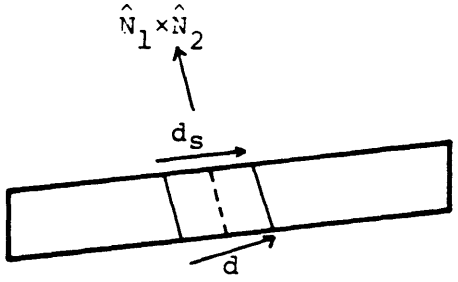

Measured distance $d_{s(p)}$ is the projection of d_s on the plane which is normal to $\hat{B}$.

$\hat{U}_s$ = unit vector in the direction of d_s
$\hat{U}_d$ = unit vector in the direction of d
$\hat{U}_s \cdot \hat{S} = 0$ $\quad$ $\hat{U}_s \cdot (\hat{N}_1 - \hat{N}_2) = 0$

Figure A-3 Schematic diagrams for separation distance analysis

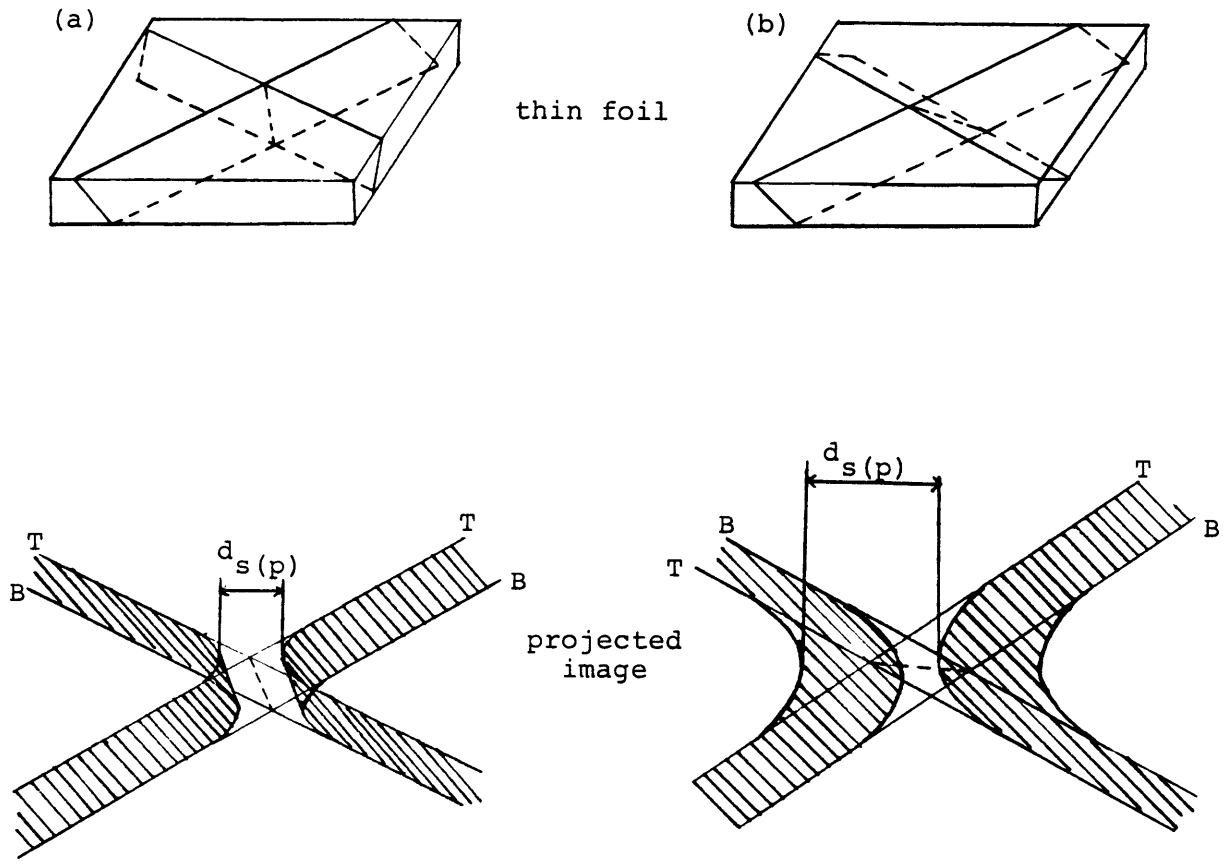

Figure A-4. Schematic diagrams showing two different types of intersecting APBs. Relative directions of two plane normals with beam direction decide the type for a particular intersection. Note the difference of $d_{s(p)}$ measurement from the projected images.

R in this experiment is one half of real separation d, as calculated from Equation (A-4). α is one half the angle between two intersecting planes which is smaller than 180°. α can be calculated once we know two intersecting planes. $f(\alpha)$ can be gotten from Figure (3-4). t is the duration of the APB migration. From this we can calculate the APB mobility, M.

APPENDIX B

ERRORS IN MEASURING DISTANCES AND CURVATURES FROM A PROJECTED IMAGE DUE TO THE SPECIMEN TILTING.

It is inevitable to tilt a thin foil sample of TEM with respect to the beam direction in order to get a superlattice dark-field image of APBs. And the image formed on a plane normal to the beam direction is the projected image of the tilted sample along the beam direction. If the tilt angle is small, the difference between the projected image and the real image will be small because the difference will be proportional to the cosine value of the tilt angle. Roughly speaking, if the tilt angle is less than 20°, the linear difference between the projected and the true image would be less than 6% which is within the measuring error range. In most of our experiments we used the tilt angles less than 20°. But in some cases where the tilt angles were large, we should consider the specimen tilt in measuring distances and curvatures from the projected images.

It would not be feasible to compensate the tilting effect exactly in measuring the local curvatures of APBs from the projected images due to the complex morphology of the APBs. But we can reduce the error if we know the total tilt angle and the tilt axis. The tilt axis can be calculated from the surface normal of the untilted specimen and the beam direction to the tilted specimen. The tilt axis would be normal to both the surface normal $\hat{S}$ and the beam direction $\hat{B}$. The tilt axis $\vec{R}$ can be expressed by:

$$\vec{R} = \frac{\hat{S} \times \hat{B}}{|\hat{S} \times \hat{B}|} \qquad \text{(B-1)}$$

And $\vec{R}$ can be drawn on the projected image if the relative rotation between the image and the diffraction pattern is known.

The linear distance between two arbitrary points on a projected image can not be greater than the true distance, but the local curvature of a projected APB image can be either larger or smaller than the true local curvature depending on the relation between the tilt axis and the APB. This is schematically illustrated in Figure (B-1). In Figure (B-1) (a), the curvature at the tip of a projected parabolic APB is larger than the true curvature. But the measurement of the migrating distance of the tip which will be along the tilt axis will not change with the tilt. The mobility calculated from the measurements of the curvature and the migrating distance of this feature will be lower than the true mobility.

In Figure (B-1) (b), the curvature at the tip of a projected parabolic APB is smaller than the true curvature. And the measurement of the migrating distance of the tip which is normal to the tilt axis is smaller that the true value due to tilting. In calculating the mobility from these measurements, the effects of the tilt on the curvature and the distance tend to cancel themselves out, because the mobility is the ratio of the curvature and the migrating distance in unit time. If we consider a circular APB in Figure (B-1) (c), we can calculate the exact effects of tilting on the measurements. If a circular APB with a radius r is tilted by angle θ, the projected image will be an ellipse with the long axis r and the short axis $r\cos\theta$. The curvature at the tip of the long axis is then given by:

$$(K)_1 = \frac{r}{r^2\cos^2\theta} \qquad \text{(B-1)}$$

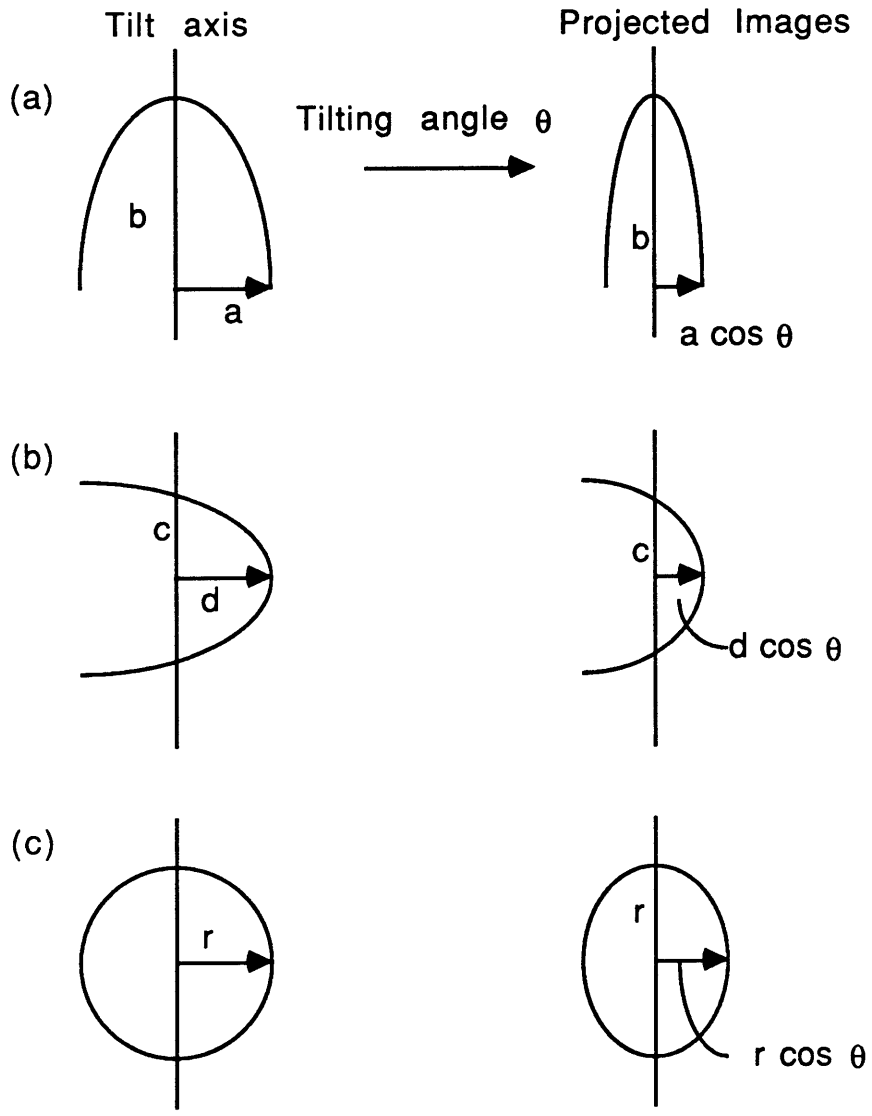

Figure (B-1) Effects of specimen tilting on the projected APB images. Linear distance between any two points is reduced or remains unchanged, and the local curvature can increase or decrease depending on the orientational relation between the tilt axis and the APB.

And the curvature at the tip of the short axis is given by:

$$(K)_s = \frac{r \cos \theta}{r^2} \qquad \text{(B-2)}$$

The migration distance along the long axis which is parallel to the tilt axis is unchanged by image projection. Thus the measured ratio of the migration distance and the curvature, which is proportional to the mobility, is smaller than the real ratio by the factor of $\cos^2\theta$. But the migration distance along the short axis which is normal to the tilt axis reduces by the factor of $\cos\theta$ by image projection. And the measured ratio of the migration distance and the curvature is the same as the real ratio because the $\cos\theta$ terms in both the curvature and distance cancel each other.

Therefore, we can reduce the error introduced by specimen tilting in calculating the mobility by measuring the migration distances and the local curvatures of the APBs which move normal to the tilt axis.

APPENDIX C

SHRINKING OF AN ELLIPTIC APB TO A CIRCULAR APB

As mentioned in Section 3-2-3, we have observed many elliptic APBs became circular as they shrunk to disappear in thin-foil samples. It would be worthwhile to analyze this problem mathematically to see if a two-dimensional elliptic boundary is expected to shrink into a circular boundary before it disappears.

Mullins [61] first considered two-dimensional motion of idealized grain boundaries where any given point of a curve moves toward its center of curvature with a speed that is proportional to the curvature. Let's consider a shrinking ellipse which has the long axis of 2a parallel to y axis and the short axis of 2b parallel to x axis. The equation of this ellipse is then given by:

$$\frac{y^2}{a^2} + \frac{x^2}{b^2} = 1 \qquad \text{(C-1)}$$

The radius of curvature of a two-dimensional curve of $y = f(x)$ is given by:

$$\frac{1}{K} = \frac{\{\sqrt{1+(y'^2)}\}^3}{y''} \qquad \text{(C-2)}$$

The curvature of the ellipse at the tip of the long axis is then given by:

$$(K)_a = \frac{a}{b^2} \qquad \text{(C-3)}$$

And the curvature at the tip of the short axis is:

$$(K)_b = \frac{b}{a^2} \qquad \text{(C-4)}$$

The shrinking rate at the tip of the long axis is then given by:

$$\frac{da}{dt} = -M \frac{a}{b^2} \tag{C-5}$$

Similarly the shrinking rate at the short axis tip is:

$$\frac{db}{dt} = -M \frac{b}{a^2} \tag{C-6}$$

where M is the mobility of the boundary.

In order for the ellipse to preserve the elliptic shape, we should have the condition:

$$\frac{da}{db} = \frac{a}{b} \tag{C-7}$$

But actually we have the condition:

$$\frac{da}{db} = (\frac{a}{b})^3 \tag{C-8}$$

Because a > b by definition, the shrinking rate of the long axis is much faster than that of the short axis. Thus the ellipse will become more circular as it shrinks.

By integrating Equation (C-8), we have:

$$\frac{a}{b} = \frac{1}{\sqrt{1+b^2c}} \tag{C-9}$$

where $c = a_o^{-2} - a_o^{-2}$. a_o and b_o are the respective initial values for a and b.

Thus if the initial ellipse has the ratio of $a_o/b_o = 2$, then

$$\frac{a}{b} = \frac{1}{\sqrt{1-\frac{3}{4}b^2}} \tag{C-10}$$

a/b becomes 1.05 when $b = 0.352b_o$. This means the initial ellipse of aspect ratio 2 becomes virtually circular (difference between the long

axis and the short axis of 5%) when the short axis is 35% of its initial length. But it should be noted that the exact circular boundary having a/b = 1 will not be formed until the ellipse totally disappear. This can be seen from Equation (C-10), where a/b = 1 only when b = 0.

In the limiting case of the infinite aspect ratio where $a_o/b_o = \infty$, we have:

$$\frac{a}{b} = \frac{1}{\sqrt{1 - b^2}} \qquad \text{(C-11)}$$

In this case we have a/b = 1.05 when $b = 0.305b_o$.

Thus we can say that an ellipse becomes virtually circular as it shrinks when their short axis becomes ≃30% of its initial value. This result is consistent with what we observed experimentally.

APPENDIX D

THE COMPUTER PROGRAMS APBPRO1 AND APBPRO2: DESCRIPTION AND SAMPLE LISTS

The programs APBPRO1 and APBPRO2 have been written to compute the equilibrium order parameters, the order parameter profiles and the energies of APBs in the Fe-Al binary alloys for given temperature and alloy composition, based on the equations described in Chapter 4.

The programs have been written in FORTRAN (in CMS operating system of IBM) and use all double precision variables except for integer constants. Alloy composition, CB, is given by the mole fraction of Fe atoms. The unit for the temperature and $V(0)/k_B$, $V(\vec{k}_1)/k_B$ and $V(\vec{k}_2)/k_B$ is the absolute temperature K. The gradient energy parameters K_C, K_{η_1}, and K_{η_2} are given in erg/nm. The free energy of the system per unit volume is calculated in erg/nm^3.

The equilibrium atomic order parameters are computed using a NAG subroutine C05NBF. Because of the logarithmic functions which can not have negative arguments, reasonable guesses for the starting values for the order parameters are needed for this subroutine to compute η_{1e} and η_{2e}.

The order parameter profiles are calculated by solving the Euler equations in Equations (4-12) through Equation (4-15) using a NAG subroutine D02HAF. Two boundary values for each differential equation should be supplied, one being the mathematical boundary condition for one end and the other being a well guessed value for the other end which will be adjusted in the subroutine.

The distance range in which the order parameter profile will be

calculated should be given in nanometers. This range should be adjusted to cover the whole diffuse interface. But if the range is much larger than the thickness of the diffuse interface, the subroutine has troubles to find the solution. Once the distance range is given, the subroutine determines the interval of calculation by itself to optimize the calculation. The number of intervals is usually far more than enough for our purpose of the profile calculation. This subroutine gives the values of η and $d\eta/dx$ from x=0 to x=xFINAL at intervals specified by NLIMIT, which is given as an input data.

The interfacial free energy of the APB is calculated by numerical integration of Equation (4-1) using Simpson's rule. The interfacial energy is calculated in erg/nm^2 and is converted in erg/cm^2 for printout. The program APBPRO1 is for <111> APBs in B2 ordered alloys, and the program APBPRO2 is for <100> APBs in DO_3 ordered alloys.

```
C     PROGRAM NAME: APBPRO1                                                  APB00010
C       THIS PROGRAM SOLVES THE EULER EQUATIONS TO GIVE THE ORDER            APB00020
C       PARAMETER PROFILE OF THE APBS WHICH GIVE MINIMUM INTERFACIAL         APB00030
C       ENERGY IN B2 ORDERED FE-AL ALLOYS. THE PROGRAM USES TWO NAG          APB00040
C       NUMERICAL SUBROUTINES. C05NBF IS USED FOR CALCULATING ORDER          APB00050
C       PARAMETERS FROM NON-LINEAR TRANSCENDENTAL EQUATIONS.                 APB00060
C       D02HAF IS USED FOR SOLVING DIFFERENTIAL EQUATIONS OF THE             APB00070
C       EULER EQUATIONS.                                                     APB00080
C                                                                            APB00090
C       VARING ONLY  B2 ORDER PARAMETER,HOLDING COMP CONSTANT.               APB00100
C       DO3 ORDER PARAMETER IS NEGLECTED IN COMPUTING B2 APB PROFILES        APB00110
C       AND ENERGY SINCE DO3 ORDER IS FORMED ONLY AFTER B2 ORDERING          APB00120
C                                                                            APB00130
C       ROUTINE FOR INTERFACIAL ENERGY CALCULATION INCLUDED.                 APB00140
C       -----------------------------------                                  APB00150
                                                                             APB00160
      IMPLICIT DOUBLE PRECISION (A-H,P-Z)                                    APB00170
C-- ETAFN AND ECFUN DECLARED AS EXTERNAL FOR USE IN C05NBF AND D02HAF        APB00180
      EXTERNAL ETAFN, ECFUN                                                  APB00190
                                                                             APB00200
      COMMON CB,TEMP,V0DK,TKAPC,TKAPE1,TKAPE2,DV1DC,DV2DC,V1DK,V2DK,         APB00210
     &   DFDC,DELF,ET1,ET2,NUMEQ                                             APB00220
                                                                             APB00230
      DIMENSION BOUND2(2,2),BDFLG2(2,2),ECVAL2(2,200)                        APB00240
      DIMENSION ETAE(2),FNVEC(2),WORK2(2,50),WORK(50)                        APB00250
                                                                             APB00260
      LWORK=50                                                               APB00270
C-------  DATA INPUT  ---------                                             APB00280
C-- THE NUMBER OF POINTS TO BE CALCULATED FOR GIVEN INTERVAL                 APB00290
      WRITE (6,*) 'NUMBER OF POINTS= '                                       APB00300
      READ (6,*) NLIMIT                                                      APB00310
C-- DATA FOR COMPOSITION, TEMPERATURE AND ENERGY PARAMETERS                  APB00320
      WRITE (6,*) 'COMPOSITION IN XFE= , TEMP IN K= '                        APB00330
      READ (6,*) CB,TEMP                                                     APB00340
      WRITE (6,*) 'ENERGY PARAMETER V0/K IN K= '                             APB00350
      READ (6,*) V0DK                                                        APB00360
      WRITE (6,*) 'GRADIENT ENERGY PARAMETERS KC,KE1,KE2 IN ERG/NM '         APB00370
      READ (6,*) TKAPC,TKAPE1,TKAPE2                                         APB00380
      WRITE (6,*) 'COMPOSITIONAL DERIVATIVES OF V1/K AND V2/K '              APB00390
      READ (6,*) DV1DC,DV2DC                                                 APB00400
                                                                             APB00410
      CB1MCB=CB*(1D0-CB)                                                     APB00420
      IF (ABS(CB1MCB) .LT. 1D-27) STOP 27                                    APB00430
                                                                             APB00440
C-- CALCULATION OF ENERGY PARAMETERS V1/K AND V2/K AS FUNCTIONS OF CB       APB00450
      V1DK=(2.0764D3+(1D0-CB)*((-1.835D4)+2.3655D4*(1D0-CB)))/CB1MCB         APB00460
      V2DK=2.9512D5+CB*((-1.2021D6)+CB*(1.6157D6+CB*(-7.2461D5)))            APB00470
                                                                             APB00480
C-- COMPUTATION OF EQUILIBRIUM ORDER PARAMETERS ETAE1 AND ETAE2              APB00490
C     USING NAG C05NBF FOR GIVEN CB AND TEMP.                                APB00500
C                                                                            APB00510
C     TOLERANCE FOR C05NBF,  THIS CAN BE ADJUSTED                            APB00520
      ETOL=1.D-05                                                            APB00530
C-- STARTING VALUES FOR ETA1E AND ETA2E, TO BE USED IN C05NBF               APB00540
C     THESE VALUES SHOULD BE ADJUSTED AS CB AND TEMP CHANGE                  APB00550
      ETAE(1)=0.050D0                                                        APB00560
      ETAE(2)=0.00D0                                                         APB00570
                                                                             APB00580
C-- CALL FOR C05NBF TO CALCULATE EQUATIONS IN SUBROUTINE ETAFN              APB00590
      IFAIL=0                                                                APB00600
```

```
      CALL C05NBF(ETAFN,2,ETAE,FNVEC,ETOL,WORK,LWORK,IFAIL)            APB00610
      WRITE(6,*) 'C05NBF ERROR CODE = ',IFAIL                          APB00620
      WRITE(6,*) 'FINAL VALUE OF 1ST ZERO = ',FNVEC(1)                 APB00630
      WRITE(6,*) 'FINAL VALUE OF 2ND ZERO = ',FNVEC(2)                 APB00640
      WRITE(6,*) 'TEMP= ',TEMP                                         APB00650
      WRITE(6,*) 'ETA1E = ',ETAE(1) ,'ETA2E = ',ETAE(2)                APB00660
      ET1=ETAE(1)                                                      APB00670
      ET2=ETAE(2)                                                      APB00680
                                                                       APB00690
C-- PARTIAL DIFF OF FREE ENERGY DIFFERENCE DELTAF BY CB AT EQUIL.      APB00700
C     ORDER PARAMETERS                                                 APB00710
      CP=CB+ETAE(1)                                                    APB00720
      CMP=CB-ETAE(1) +ETAE(2)                                          APB00730
      CMM=CB-ETAE(1) -ETAE(2)                                          APB00740
      Z=DLOG(CP/(1D0-CP))+.5D0*DLOG(CMM*CMP/((1D0-CMM)*(1D0-CMP)))     APB00750
      Z=TEMP*Z+V0DK*(2D0*CB-1D0)+DV1DC*ETAE(1)**2+                     APB00760
     &  .5D0*DV2DC*ETAE(2)**2                                          APB00770
      DFDC=5.7195D-15*Z/(2D0*TKAPC)                                    APB00780
                                                                       APB00790
C-- SOLVE DIFF'NTIAL EQUATIONS                                         APB00800
C     USING NAG D02HAF. EQUATIONS SUPPLIED IN SUBROUTINE ECFUN         APB00810
      NUMEQ=2                                                          APB00820
                                                                       APB00830
C     FREE ENERGIES IN UNIT VOLUME (ERG/NM3)                           APB00840
      DELF0=5.7195D-15*(V0DK*CB*(CB-1D0)+2.0*TEMP*CB*DLOG(CB)+         APB00850
     &      2.0*TEMP*(1D0-CB)*DLOG(1D0-CB))                            APB00860
      DELF=5.7195D-15*(V0DK*CB*(CB-1D0)+V1DK*ETAE(1)**2+0.5D0*V2DK*    APB00870
     &     ETAE(2)**2+TEMP*(CP*DLOG(CP)+(1D0-CP)*DLOG(1D0-CP)+         APB00880
     &     0.5D0*CMM*DLOG(CMM)+0.5D0*(1D0-CMM)*DLOG(1D0-CMM)+          APB00890
     &     0.5D0*CMP*DLOG(CMP)+0.5D0*(1D0-CMP)*DLOG(1D0-CMP)))         APB00900
      DETADX=DSQRT((DELF0-DELF)/TKAPE1)                                APB00910
C     DETADX IS AN ESTIMATE OF THE INITIAL SLOPE OF ORDER PARAMETER    APB00920
C       PROFILE                                                        APB00930
                                                                       APB00940
C-- BOUNDARY CONDITIONS (SOME FIXED, SOME ADJUSTABLE)                  APB00950
                                                                       APB00960
      BOUND2(1,1)=0D0                                                  APB00970
      BOUND2(2,1)=DETADX                                               APB00980
      BOUND2(1,2)=ETAE(1)                                              APB00990
      BOUND2(2,2)=0D0                                                  APB01000
      BDFLG2(1,1)=0D0                                                  APB01010
      BDFLG2(2,1)=1D0                                                  APB01020
      BDFLG2(1,2)=0D0                                                  APB01030
      BDFLG2(2,2)=1D0                                                  APB01040
                                                                       APB01050
C-- RANGE OF THE DISTANCE OF APB THICKNESS IN NM                       APB01060
C    XFINAL SHOULD BE ADJUSTED ACCORDING TO THE DIFFUSENESS OF APB     APB01070
      XINIT=0D0                                                        APB01080
      WRITE (6,*) 'XFINAL= '                                           APB01090
      READ (6,*) XFINAL                                                APB01100
C     ADJUSTABLE TOLERANCE FOR D02HAF                                  APB01110
      TOL=1D-6                                                         APB01120
      IFAIL=110                                                        APB01130
                                                                       APB01140
      CALL D02HAF(BOUND2, BDFLG2, NUMEQ, XINIT, XFINAL, TOL, ECFUN,    APB01150
     &   ECVAL2, NLIMIT, WORK2,LWORK, IFAIL)                           APB01160
                                                                       APB01170
      IF (IFAIL .EQ. 0) GOTO 9000                                      APB01180
      WRITE(6,*) 'Diff-eq. failure = ',IFAIL,'Tolerance =',TOL         APB01190
                                                                       APB01200
```

```
 9000 WRITE(6,9015) CB,TEMP,ETAE(1),ETAE(2)                              APB01210
 9015 FORMAT (1X,'CB=',F5.3,2X,'TEMP=',F6.1,2X,'ETA1E=',E11.4,2X,        APB01220
     & 'ETA2E=',E11.4)                                                   APB01230
      WRITE(6,*) 'FROM X=0NM TO XFINAL= ',XFINAL                         APB01240
      WRITE(6,9014)(ECVAL2(1,J),J=1,NLIMIT)                              APB01250
      WRITE(6,9013)(ECVAL2(2,J),J=1,NLIMIT)                              APB01260
 9014 FORMAT(1X,'VALUE OF ETA1 FROM X=0 TO XFINAL'  //6(D11.4,1X))       APB01270
 9013 FORMAT(1X,'VALUE OF (ETA1)" FROM X=0 TO XFINAL'  //6(D11.4,1X))    APB01280
                                                                         APB01290
C-----------------------------------------------------------------       APB01300
C--  CALCULATION OF INTERFACIAL ENERGY SIGMA USING SIMPSON FORMULA        APB01310
      WRITE(6,9020) NLIMIT                                               APB01320
 9020 FORMAT(1X,'NUMBER OF POINTS USED IN INTEGRATION FOR SIGMA=',I7)     APB01330
      IF (NLIMIT .EQ. (NLIMIT/2)*2) GOTO 210                             APB01340
      NU1=NLIMIT-1                                                       APB01350
      NU2=NLIMIT-2                                                       APB01360
      GOTO 220                                                           APB01370
  210 NU1=NLIMIT                                                         APB01380
      NU2=NLIMIT-1                                                       APB01390
  220 H=(XFINAL-XINIT)/(NLIMIT-1)                                        APB01400
      SUM1=0D0                                                           APB01410
      SUM2=0D0                                                           APB01420
      DO 110 I=2,NU1,2                                                   APB01430
         SUM1=SUM1+4D0*ECVAL2(2,I)**2                                    APB01440
  110 CONTINUE                                                           APB01450
      DO 120 I=3,NU2,2                                                   APB01460
         SUM2=SUM2+2D0*ECVAL2(2,I)**2                                    APB01470
  120 CONTINUE                                                           APB01480
                                                                         APB01490
      TINT1=(H/3D0)*(SUM1+SUM2+ECVAL2(2,1)**2+ECVAL2(2,NLIMIT)**2)       APB01500
      SUM3=0D0                                                           APB01510
      SUM4=0D0                                                           APB01520
      DO 130 I=2,NU1,2                                                   APB01530
         SUM3=SUM3+4D0*FREE(ECVAL2(1,I))                                 APB01540
  130 CONTINUE                                                           APB01550
      DO 140 I=3,NU2,2                                                   APB01560
         SUM4=SUM4+2D0*FREE(ECVAL2(1,I))                                 APB01570
  140 CONTINUE                                                           APB01580
      TINT2=(H/3D0)*(SUM3+SUM4+FREE(ECVAL2(1,1))                         APB01590
     &       +FREE(ECVAL2(1,NLIMIT)))                                    APB01600
      SIGMA=(2D0*TINT2+2D0*TKAPE1*TINT1)*1D14                            APB01610
      WRITE(6,9016) SIGMA                                                APB01620
 9016 FORMAT(1X,'INTERFACIAL ENERGY OF B2 APB= ',D12.5,' ERG/CM2')       APB01630
                                                                         APB01640
                                                                         APB01650
      STOP 9000                                                          APB01660
      END                                                                APB01670
                                                                         APB01680
C---- END OF MAIN PROGRAM  ------------------------------                APB01690
                                                                         APB01700
                                                                         APB01710
      FUNCTION FREE(ETA)                                                 APB01720
C-- CALCULATION OF FREE ENERGY DIFFERENCE                                APB01730
      IMPLICIT DOUBLE PRECISION (A-H,P-Z)                                APB01740
      COMMON CB,TEMP,V0DK,TKAPC,TKAPE1,TKAPE2,DV1DC,DV2DC,V1DK,V2DK,     APB01750
     &       DFDC,DELF,ET1,ET2,NUMEQ                                     APB01760
                                                                         APB01770
      CP=CB+ETA                                                          APB01780
      CMP=CB-ETA                                                         APB01790
      CMM=CB-ETA                                                         APB01800
```

```
                                                                      APB01810
      FREE=5.7195D-15*(V0DK*CB*(CB-1D0)+V1DK*ETA**2+                  APB01820
     &     TEMP*(CP*DLOG(CP)+                                         APB01830
     &     (1D0-CP)*DLOG(1D0-CP)+0.5D0*CMM*DLOG(CMM)+0.5D0*(1D0-CMM)* APB01840
     &     DLOG(1D0-CMM)+0.5D0*CMP*DLOG(CMP)+0.5D0*(1D0-CMP)*         APB01850
     &     DLOG(1D0-CMP)))-DELF                                       APB01860
                                                                      APB01870
      RETURN                                                          APB01880
      END                                                             APB01890
                                                                      APB01900
                                                                      APB01910
C-- SUBROUTINE ETAFN TO BE USED IN C05NBF                            APB01920
                                                                      APB01930
      SUBROUTINE  ETAFN(N,ETAE,FNVEC,IFLAG)                           APB01940
      IMPLICIT DOUBLE PRECISION (A-H,P-Z)                             APB01950
      COMMON CB,TEMP,V0DK,TKAPC,TKAPE1,TKAPE2,DV1DC,DV2DC,V1DK,V2DK,  APB01960
     &   DFDC,DELF,ET1,ET2,NUMEQ                                      APB01970
      DIMENSION ETAE(N),FNVEC(N)                                      APB01980
                                                                      APB01990
      WRITE(6,*) 'ETAFN CALLED WITH: ',ETAE(1),ETAE(2)                APB02000
                                                                      APB02010
      CM=CB-ETAE(1)                                                   APB02020
      CP=CB+ETAE(1)                                                   APB02030
      CMP=CM+ETAE(2)                                                  APB02040
      CMM=CM-ETAE(2)                                                  APB02050
      ETV=DEXP(4D0*ETAE(1)*V1DK/TEMP)                                 APB02060
                                                                      APB02070
      CCCC=(1D0-CMP)*CMM/((1D0-CMM)*CMP)                              APB02080
      FNVEC(1)=CCCC-DEXP(2D0*ETAE(2)*V2DK/TEMP)                       APB02090
                                                                      APB02100
      CE1=CP**2*ETV-(1-CP)**2                                         APB02110
      IF (CE1 .NE. 0D0) GOTO 90                                       APB02120
      WRITE(6,*) 'ETAFN(2) 1ST  RESET AT ',ETAE(1),ETAE(2)            APB02130
      CE1=1D0                                                         APB02140
90    C1EC1=(CP*(1D0-CM))**2*ETV-(CM*(1D0-CP))**2                     APB02150
                                                                      APB02160
      C1EC1=C1EC1/CE1                                                 APB02170
      FNVEC(2)=ETAE(2)**2-C1EC1                                       APB02180
                                                                      APB02190
      RETURN                                                          APB02200
      END                                                             APB02210
                                                                      APB02220
                                                                      APB02230
C-- SUBROUTINE ECFUN TO BE USED IN D02HAF                            APB02240
                                                                      APB02250
      SUBROUTINE ECFUN(X, VARS, DIFVEC)                               APB02260
C     Compute derivates according to expanded first-order eqns.       APB02270
      IMPLICIT DOUBLE PRECISION (A-H, O-Z, $)                         APB02280
      DIMENSION VARS(2), DIFVEC(2), ETAE(2)                           APB02290
      DATA IPRINT / 1 /                                               APB02300
      COMMON CB,TEMP,V0DK,TKAPC,TKAPE1,TKAPE2,DV1DC,DV2DC,V1DK,V2DK,  APB02310
     &   DFDC,DELF,ET1,ET2,NUMEQ                                      APB02320
                                                                      APB02330
      CP=CB+VARS(1)                                                   APB02340
      CMP=CB-VARS(1)                                                  APB02350
      CMM=CB-VARS(1)                                                  APB02360
      CPD1=CP/(1D0-CP)                                                APB02370
      CMPD1=CMP/(1D0-CMP)                                             APB02380
      CMMD1=CMM/(1D0-CMM)                                             APB02390
      IF (CPD1 .LE. 0D0) THEN                                         APB02400
```

```
      WRITE (6,*) CPD1,X,VARS(1), VARS(2)                                APB02410
      STOP 1000                                                          APB02420
     ENDIF                                                               APB02430
                                                                         APB02440
13   CMMD1=CMMD1*CMPD1                                                  APB02450
     IF (CMMD1 .GT. 1D-44) GOTO 14                                      APB02460
     WRITE(6,*) '2ND LOGARITHM ARGUMENT RESET IN ECFUN'                 APB02470
     WRITE (6,*)X,VARS(1),VARS(2),CMMD1                                 APB02480
     STOP 1100                                                          APB02490
14   CPD1L=DLOG(CPD1)                                                   APB02500
     CCCCL2=.5D0*DLOG(CMMD1)                                            APB02510
                                                                         APB02520
     DIFVEC(1)=VARS(2)                                                  APB02530
     DIFVEC(2)=(5.7195D-15/TKAPE1)*( V1DK*VARS(1)+(TEMP/2D0)*           APB02540
    &    (CPD1L-CCCCL2) )                                              APB02550
                                                                         APB02560
                                                                         APB02570
     RETURN                                                             APB02580
     END                                                                APB02590
```

```
C     PROGRAM NAME: APBPRO2                                                  APB00010
C       THIS PROGRAM SOLVES THE EULER EQUATIONS TO GIVE THE ORDER            APB00020
C       PARAMETER PROFILE OF THE APBS WHICH GIVES THE MINIMUM                APB00030
C       INTERFACIAL ENERGY IN D03 ORDERED FE-AL ALLOYS.                      APB00040
C       THE PROGRAM USES TWO NAG NUMERICAL SUBROUTINES.  C05NBF              APB00050
C       IS USED FOR CALCULATING ORDER PARAMETERS FROM NON-LINEAR             APB00060
C       TRANSCENDENTAL EQUATIONS.  D02HAF IS USED FOR SOLVING                APB00070
C       DIFFERENTIAL EQUATIONS OF THE EULE EQUATIONS.                        APB00080
C                                                                            APB00090
C       VARING ONLY THE D03 ORDER PARAMETER ETA2, HOLDING                    APB00100
C       COMPOSITION AND B2 ORDER PARAMETER ETA1 CONSTANT.                    APB00110
C                                                                            APB00120
C       ROUTINE FOR INTERFACIAL ENERGY CALCULATION INCLUDED.                 APB00130
C       ---------------------------------------------------                  APB00140
                                                                             APB00150
                                                                             APB00160
      IMPLICIT DOUBLE PRECISION (A-H,P-Z)                                    APB00170
C-- ETAFN AND ECFUN DECLARED AS EXTERNAL FOR USE IN C05NBF AND D02HAF        APB00180
      EXTERNAL ETAFN, ECFUN                                                  APB00190
                                                                             APB00200
      COMMON CB,TEMP,V0DK,TKAPC,TKAPE1,TKAPE2,DV1DC,DV2DC,V1DK,V2DK,         APB00210
     &  ET1,ET2, DFDC,DELF2,NUMEQ                                            APB00220
                                                                             APB00230
      DIMENSION BOUND2(2,2),BDFLG2(2,2),ECVAL2(2,131)                        APB00240
      DIMENSION ETAE(2),FNVEC(2),WORK2(2,50),WORK(50)                        APB00250
                                                                             APB00260
      LWORK=50                                                               APB00270
C--------   DATA INPUT   ------------                                        APB00280
C     THE NUMBER OF POINTS TO BE CALCULATED FOR GIVEN INTERVAL               APB00290
      WRITE (6,*) 'NUMBER OF POINTS= '                                       APB00300
      READ (6,*) NLIMIT                                                      APB00310
C     DATA FOR COMPOSITION, TEMPERATURE AND ENERGY PARAMETERS                APB00320
      WRITE (6,*) 'COMPOSITION IN XFE= , TEMP IN K= '                        APB00330
      READ (6,*) CB,TEMP                                                     APB00340
      WRITE (6,*) 'ENERGY PARAMETER V0/K IN K= '                             APB00350
      READ (6,*) V0DK                                                        APB00360
      WRITE (6,*) 'GRADIENT ENERGY PARAMETERS KC,KE1,KE2 IN ERG/NM'          APB00370
      READ (6,*) TKAPC,TKAPE1,TKAPE2                                         APB00380
      WRITE (6,*) 'COMPOSITIONAL DERIVATIVES OF V1/K AND V2/K'               APB00390
      READ (6,*) DV1DC,DV2DC                                                 APB00400
                                                                             APB00410
                                                                             APB00420
      CB1MCB=CB*(1D0-CB)                                                     APB00430
      IF (ABS(CB1MCB) .LT. 1D-27) STOP 27                                    APB00440
                                                                             APB00450
C-- CALCULATION OF ENERGY PARAMETERS V1/K AND V2/K AS FUNCTIONS OF CB        APB00460
      V1DK=(2.0764D3+(1D0-CB)*((-1.835D4)+2.3655D4*(1D0-CB)))/CB1MCB         APB00470
      V2DK=2.9512D5+CB*((-1.2021D6)+CB*(1.6157D6+CB*(-7.2461D5)))            APB00480
                                                                             APB00490
C-- COMPUTATION OF EQUILIBRIUM ORDER PARAMETERS ETAE1 AND ETAE2              APB00500
C     USING NAG C05NBF FOR GIVEN CB AND TEMP.                                APB00510
                                                                             APB00520
C     TOLERANCE FOR C05NBF,  THIS CAN BE ADJUSTED                            APB00530
      ETOL=1.D-06                                                            APB00540
C     STARTING VALUES FOR ETA1E AND ETA2E                                    APB00550
C     THESE VALUES SHOULD BE ADJUSTED AS CB AND TEMP CHANGE                  APB00560
      ETAE(1)=0.20D0                                                         APB00570
      ETAE(2)=0.02D0                                                         APB00580
                                                                             APB00590
C-- CALL FOR C05NBF TO CALCULATE EQUATIONS IN SOUBROUTINE ETAFN             APB00600
```

```
      IFAIL=0                                                          APB00610
      CALL C05NBF(ETAFN,2,ETAE,FNVEC,ETOL,WORK,LWORK,IFAIL)            APB00620
      WRITE(6,*) 'C05NBF ERROR CODE = ',IFAIL                          APB00630
      WRITE(6,*) 'FINAL VALUE OF 1ST ZERO = ',FNVEC(1)                 APB00640
      WRITE(6,*) 'FINAL VALUE OF 2ND ZERO = ',FNVEC(2)                 APB00650
      WRITE(6,*) 'TEMP= ',TEMP                                         APB00660
      WRITE(6,*) 'ETA1E = ',ETAE(1) ,'ETA2E = ',ETAE(2)                APB00670
      ET1=ETAE(1)                                                      APB00680
      ET2=ETAE(2)                                                      APB00690
C-- PARTIAL DIFF OF FREE ENERGY DIFFERENCE DELTAF BY CB AT EQUIL.      APB00700
C     ORDER PARAMETERS.                                                APB00710
      CM=CB-ETAE(1)                                                    APB00720
      CP=CB+ETAE(1)                                                    APB00730
      CMP=CB-ETAE(1) +ETAE(2)                                          APB00740
      CMM=CB-ETAE(1) -ETAE(2)                                          APB00750
      Z=DLOG(CP/(1D0-CP))+.5D0*DLOG(CMM*CMP/((1D0-CMM)*(1D0-CMP)))     APB00760
      Z=TEMP*Z+V0DK*(2D0*CB-1D0)+DV1DC*ETAE(1)**2+                     APB00770
     &  .5D0*DV2DC*ETAE(2)**2                                          APB00780
      DFDC=5.7195D-15*Z/(2D0*TKAPC)                                    APB00790
                                                                       APB00800
C-- SOLVING DIFF'NTIAL EQUATIONS USING NAG D02HAF.                     APB00810
C     EQUATIONS SUPPLIED IN SUBROUTINE ECFUN                           APB00820
                                                                       APB00830
      NUMEQ=2                                                          APB00840
                                                                       APB00850
C     FREE ENERGIES IN UNIT VOLUME (ERG/NM3)                           APB00860
      DELF20=5.7195D-15*(V0DK*CB*(CB-1D0)+V1DK*ETAE(1)**2+TEMP*(CP*    APB00870
     &       DLOG(CP)+CM*DLOG(CM)+(1D0-CP)*DLOG(1D0-CP)+(1D0-CM)*      APB00880
     &       DLOG(1D0-CM)))                                            APB00890
      DELF2=5.7195D-15*(V0DK*CB*(CB-1D0)+V1DK*ETAE(1)**2+0.5D0*V2DK*   APB00900
     &      ETAE(2)**2+TEMP*(CP*DLOG(CP)+(1D0-CP)*DLOG(1D0-CP))+       APB00910
     &      0.5D0*TEMP*(CMM*DLOG(CMM)+(1D0-CMM)*DLOG(1D0-CMM)+         APB00920
     &      CMP*DLOG(CMP)+(1D0-CMP)*DLOG(1D0-CMP)))                    APB00930
      DET2DX=DSQRT((DELF20-DELF2)/TKAPE2)                              APB00940
      WRITE(6,*) 'DET2DX=',DET2DX                                      APB00950
C-- DET2DX IS AN ESTIMATE OF THE INITIAL SLOPE OF ORDER PARAMETER      APB00960
C     PROFILE                                                          APB00970
                                                                       APB00980
C-- BOUNDARY CONDITIONS (SOME FIXED, SOME ADJUSTABLE)                  APB00990
                                                                       APB01000
      BOUND2(1,1)=0D0                                                  APB01010
      BOUND2(2,1)=DET2DX                                               APB01020
      BOUND2(1,2)=ETAE(2)                                              APB01030
      BOUND2(2,2)=0D0                                                  APB01040
      BDFLG2(1,1)=0D0                                                  APB01050
      BDFLG2(2,1)=1D0                                                  APB01060
      BDFLG2(1,2)=0D0                                                  APB01070
      BDFLG2(2,2)=1D0                                                  APB01080
                                                                       APB01090
C-- RANGE OF THE DISTANCE OF APB THICKNESS IN NM                       APB01100
C   XFINAL SHOULD BE ADJUSTED ACCORDING TO THE DIFFUSENESS OF APB.     APB01110
      XINIT=0D0                                                        APB01120
      WRITE(6,*) 'XFINAL= '                                            APB01130
      READ (6,*) XFINAL                                                APB01140
C     ADJUSTABLE TOLERANCE FOR D02HAF                                  APB01150
      TOL=1D-6                                                         APB01160
      IFAIL=110                                                        APB01170
                                                                       APB01180
      CALL D02HAF(BOUND2, BDFLG2, NUMEQ, XINIT, XFINAL, TOL, ECFUN,    APB01190
     &   ECVAL2, NLIMIT, WORK2,LWORK, IFAIL)                           APB01200
```

```
                                                                      APB01210
      IF (IFAIL .EQ. 0) GOTO 9000                                     APB01220
      WRITE(6,*) 'Diff-eq. failure = ',IFAIL,'Tolerance =',TOL        APB01230
                                                                      APB01240
 9000 WRITE(6,9015) CB,TEMP,ETAE(1),ETAE(2)                          APB01250
 9015 FORMAT (1X,'CB=',F5.3,2X,'TEMP=',F5.1,2X,'ETA1E=',E11.4,2X,     APB01260
     & 'ETA2E=',E11.4)                                                APB01270
      WRITE(6,*) 'FROM X=0NM TO XFINAL= ', XFINAL                     APB01280
      WRITE(6,9014)(ECVAL2(1,J),J=1,NLIMIT)                           APB01290
      WRITE(6,9013)(ECVAL2(2,J),J=1,NLIMIT)                           APB01300
 9014 FORMAT(1X,'VALUE OF ETA2 FROM X=0 TO XFINAL  //6(D11.4,1X))     APB01310
 9013 FORMAT(1X,'VALUE OF (ETA2)" FROM X=0 TO XFINAL  //6(D11.4,1X))  APB01320
                                                                      APB01330
                                                                      APB01340
C-- CALCULATION OF INTERFACIAL ENERGY SIGMA USING SIMPSON FORMULA      APB01350
                                                                      APB01360
      WRITE(6,9020) NLIMIT                                            APB01370
 9020 FORMAT(1X,'NUMBER OF POINTS USED IN INTEGRATION = ',I7)         APB01380
      IF (NLIMIT .EQ. (NLIMIT/2)*2) GOTO 210                          APB01390
      NU1=NLIMIT-1                                                    APB01400
      NU2=NLIMIT-2                                                    APB01410
      GOTO 220                                                        APB01420
  210 NU1=NLIMIT                                                      APB01430
      NU2=NLIMIT-1                                                    APB01440
  220 H=(XFINAL-XINIT)/(NLIMIT-1)                                     APB01450
      SUM1=0D0                                                        APB01460
      SUM2=0D0                                                        APB01470
      DO 110 I=2,NU1,2                                                APB01480
         SUM1=SUM1+4D0*ECVAL2(2,I)**2                                 APB01490
  110 CONTINUE                                                        APB01500
      DO 120 I=3,NU2,2                                                APB01510
         SUM2=SUM2+2D0*ECVAL2(2,I)**2                                 APB01520
  120 CONTINUE                                                        APB01530
      TINT1=(H/3.0D0)*(SUM1+SUM2+ECVAL2(2,1)**2                       APB01540
     &        +ECVAL2(2,NLIMIT)**2)                                    APB01550
      SUM3=0D0                                                        APB01560
      SUM4=0D0                                                        APB01570
      DO 130 I=2,NU1,2                                                APB01580
         SUM3=SUM3+4D0*FREE(ECVAL2(1,I))                              APB01590
  130 CONTINUE                                                        APB01600
      DO 140 I=3,NU2,2                                                APB01610
         SUM4=SUM4+2D0*FREE(ECVAL2(1,I))                              APB01620
  140 CONTINUE                                                        APB01630
      TINT2=(H/3D0)*(SUM3+SUM4+FREE(ECVAL2(1,1))                      APB01640
     &       +FREE(ECVAL2(1,NLIMIT)))                                 APB01650
      SIGMA=(2D0*TINT2+2D0*TKAPE2*TINT1)*1D14                         APB01660
      WRITE(6,9017) SIGMA                                             APB01670
 9017 FORMAT(1X,'INTERFACIAL ENERGY OF DO3 APB= ',D12.5,' ERG/CM2')   APB01680
                                                                      APB01690
      STOP 9000                                                       APB01700
      END                                                             APB01710
                                                                      APB01720
C---- END OF MAIN PROGRAM   ----------------------------------------  APB01730
                                                                      APB01740
                                                                      APB01750
C-- FUNCTION FOR FREE ENERGY DIFFERENCE CALCULATION                   APB01760
      FUNCTION FREE(ETA2)                                             APB01770
      IMPLICIT DOUBLE PRECISION (A-H,P-Z)                             APB01780
      COMMON CB,TEMP,V0DK,TKAPC,TKAPE1,TKAPE2,DV1DC,DV2DC,V1DK,V2DK,  APB01790
     &       ET1,ET2,DFDC,DELF2,NUMEQ                                 APB01800
```

```
                                                                      APB01810
      CP=CB+ET1                                                       APB01820
      CM=CB-ET1                                                       APB01830
      CMP=CM+ETA2                                                     APB01840
      CMM=CM-ETA2                                                     APB01850
                                                                      APB01860
      FREE=5.7195D-15*(V0DK*CB*(CB-1D0)+V1DK*ET1**2                   APB01870
     &     +0.5D0*V2DK*ETA2**2                                        APB01880
     &     +TEMP*(CP*DLOG(CP)+(1D0-CP)*DLOG(1D0-CP))+0.5D0*TEMP*      APB01890
     &     (CMM*DLOG(CMM)+(1D0-CMM)*DLOG(1D0-CMM)+CMP*DLOG(CMP)+      APB01900
     &     (1D0-CMP)*DLOG(1D0-CMP)))-DELF2                            APB01910
                                                                      APB01920
      RETURN                                                          APB01930
      END                                                             APB01940
                                                                      APB01950
C---- SUBROUTINE ETAFN TO BE USED IN C05NBF                           APB01960
                                                                      APB01970
      SUBROUTINE  ETAFN(N,ETAE,FNVEC,IFLAG)                           APB01980
      IMPLICIT DOUBLE PRECISION (A-H,P-Z)                             APB01990
      COMMON CB,TEMP,V0DK,TKAPC,TKAPE1,TKAPE2,DV1DC,DV2DC,V1DK,V2DK,  APB02000
     &  ET1,ET2, DFDC,DELF2,NUMEQ                                     APB02010
      DIMENSION ETAE(N),FNVEC(N)                                      APB02020
                                                                      APB02030
      WRITE(6,*) 'ETAFN CALLED WITH: ',ETAE(1),ETAE(2)                APB02040
                                                                      APB02050
      CM=CB-ETAE(1)                                                   APB02060
      CP=CB+ETAE(1)                                                   APB02070
      CMP=CM+ETAE(2)                                                  APB02080
      CMM=CM-ETAE(2)                                                  APB02090
      ETV=DEXP(4D0*ETAE(1)*V1DK/TEMP)                                 APB02100
                                                                      APB02110
      CCCC=(1D0-CMP)*CMM/((1D0-CMM)*CMP)                              APB02120
      FNVEC(1)=CCCC-DEXP(2D0*ETAE(2)*V2DK/TEMP)                       APB02130
                                                                      APB02140
      CE1=CP**2*ETV-(1-CP)**2                                         APB02150
      IF (CE1 .NE. 0D0) GOTO 90                                       APB02160
      WRITE(6,*) 'ETAFN(2) 1ST  RESET AT ',ETAE(1),ETAE(2)            APB02170
      CE1=1D0                                                         APB02180
90    C1EC1=(CP*(1D0-CM))**2*ETV-(CM*(1D0-CP))**2                     APB02190
                                                                      APB02200
      C1EC1=C1EC1/CE1                                                 APB02210
      FNVEC(2)=ETAE(2)**2-C1EC1                                       APB02220
                                                                      APB02230
      RETURN                                                          APB02240
      END                                                             APB02250
C---- SUBROUTINE ECFUN TO BE USED IN D02HAF                           APB02260
                                                                      APB02270
      SUBROUTINE ECFUN(X, VARS, DIFVEC)                               APB02280
C     Compute derivates according to expanded first-order eqns.       APB02290
      IMPLICIT DOUBLE PRECISION (A-H, O-Z, $)                         APB02300
      DIMENSION VARS(2), DIFVEC(2), ETAE(2)                           APB02310
      DATA IPRINT / 1 /                                               APB02320
      COMMON CB,TEMP,V0DK,TKAPC,TKAPE1,TKAPE2,DV1DC,DV2DC,V1DK,V2DK,  APB02330
     &  ET1,ET2, DFDC,DELF2,NUMEQ                                     APB02340
                                                                      APB02350
                                                                      APB02360
      CM=CB-ET1                                                       APB02370
      CP=CB+ET1                                                       APB02380
      CMP=CM+VARS(1)                                                  APB02390
      CMM=CM-VARS(1)                                                  APB02400
```

```
      CPD1=CP/(1D0-CP)                                                  APB02410
      CMPD1=CMP/(1D0-CMP)                                               APB02420
      CMMD1=CMM/(1D0-CMM)                                               APB02430
      CMPM=(CMP*(1D0-CMM))/(CMM*(1D0-CMP))                              APB02440
                                                                        APB02450
      IF ((VARS(1).GT.(1D0-CB+ET1)).OR. (VARS(1).GT.(CB-ET1)))          APB02460
     &   THEN                                                           APB02470
         WRITE(6,*) X,VARS(1), VARS(2)                                  APB02480
         STOP 100                                                       APB02490
      ENDIF                                                             APB02500
                                                                        APB02510
15    DIFVEC(1)=VARS(2)                                                 APB02520
      DIFVEC(2)=(5.7195D-15/(2D0*TKAPE2))*(V2DK*VARS(1)+                APB02530
     &   .5D0*TEMP*DLOG(CMPM) )                                         APB02540
      RETURN                                                            APB02550
      END                                                               APB02560
```

BIBLIOGRAPHY

1. R. Smoluchowski, Phys. Rev. 83, 69 (1951)
2. D. Turnbull, Trans. AIME 191, 661 (1951)
3. B. Sundquist, Metall. Trans. 4, 1919 (1973)
4. J. W. Cahn, Acta Met. 10, 789 (1962)
5. M. Hillert, Acta Met. 13, 227 (1965)
6. G. Sauthoff, Acta Met. 21, 273 (1973)
7. A. J. Ardell, M. Mardesich, and C.N.J. Wagner, Acta Met. 27, 1261 (1979)
8. B. B. Rath and H. Hu, Trans. AIME 245, 1243 (1969)
9. K. Lücke and K. Detert, Acta Met. 5, 628 (1957)
10. J. W. Cahn, Acta Met. 10, 789 (1962)
11. M. Hillert and B. Sundman, Acta Met. 24, 731 (1976)
12. J. E. Krzanowski and S. M. Allen, Surface Science 144, 153 (1984)
13. J. W. Rutter and K. T. Aust, Trans, AIME 218, 682 (1960)
14. C. Frois and O. Ditrimov, Mem. Sci. Rev. Met. 59, 643 (1962)
15. R. C. Sun and C. L. Bauer, Acta Met. 18, 639 (1970)
16. A. M. Glaeser, H. K. Bowen, and R. M. Cannon, Conference Proceeding of "Surfaces and Interfaces in Ceramic and Ceramic-Metal Systems," Ed. J. A. Pask and A. G. Evans, July 1980 Berkely, California. Plenum Press. Laboratory Report No. 8.
17. J. W. Cahn and J. E. Hilliard, J. Chem. Phys. 28, 258 (1958)
18. S. M. Allen and J. W. Cahn, Acta Met. 27, 1085 (1979)
19. J. E. Krzanowski and S. M. Allen, Acta Met. 31, 213 (1983)
20. J. E. Krzanowski, Ph.D. Thesis Dept. of Mat. Sci. Eng. M.I.T., Cambridge, Mass., (1983)
21. J. E. Krzanowski and S. M. Allen, Acta Met. 34, 1035 (1986)
22. J. E. Krzanowski and S. M. Allen, Acta Met. 34, 1045 (1986)
23. A. English, Trans. AIME 236, 14 (1966)
24. W. L. Bragg and E.L. Williams, Proc. Roy. Soc. London A145, 699 (1934), 151, 540 (1935), 152, 231 (1935)
25. H. E. Cook, D. deFontaine and J.E. Hilliard, Acta Met. 17, 765 (1969)
26. A. J. Bradley and A. H. Jay, Pro. Roy. Soc. London (A) 136, 210 (1932)
27. M. Hansen and K. Anderko, Constitution of Binary Alloys, McGraw-Hill, New York (1958)
28. A. Taylor and R. M. Jones, J. Phys. Chem. Solids 6, 16 (1958)
29. A. Lawley and R. W. Cahn, J. Phys. Chem. Solids 20, 204 (1961)
30. R. G. Davis, J. Phy. Chem. Solids 24, 985 (1963)
31. H. Okamoto and P. A. Beck, Met. Trans. 2, 569 (1971)
32. K. Oki, M. Hasaka and T. Eguchi, Trans. JIM 14, 8 (1973)
33. H. J. McQueen and G. C. Kuczynski, Trans. TMS-AIME 215, 619 (1959)
34. P. A. Flinn and S. L. Ruby, Phys. Rev. 124, 34 (1961)
35. L. Cser, J. Ostanevich and L. Pál, Phys. Status Solidi 20, 581 (1967)
36. K. Oki, A. Yamamura, K. Kudo and T. Eguchi, Trans. JIM 20, 451 (1979)
37. P. R. Swann, W. R. Duff and R. M. Fisher, Trans. TMS-AIME 245, 851 (1969)
38. P. R. Swann, W. R. Duff and R. M. Fisher, Met. Trans. 3, 409 (1972)
39. P. S. Rudman, Acta Met. 8, 321 (1960)
40. G. Inden, Acta Met. 22, 945 (1974)

41. N. S. Golosov, A. M. Tolstik and L. Ya Pudan, J. Phys. Chem. Solids. 37, 273 (1970)
42. M. Hasaka, Trans. JIM 21, 660 (1980)
43. H. Sagane and K. Oki, Trans. JIM 21, 811 (1980)
44. S. V. Semenovskaya, Phys. Stat. Sol. (b) 64, 291 (1974)
45. A. G. Khachaturyan, Phys. Stat. Sol. (b) 60, 9 (1973)
46. A. G. Khachaturyan, Theory of Structural Transformations in Solids, John Wiley & Sons, New York (1983) Chapter 3
47. S. M. Allen and J. W. Cahn, Acta Met. 23, 1017 (1975)
48. P. Clapp, Mat. Res. Soc. Symp. Proc. 39, 31 (1985)
49. S. V. Semenovskaya and D.M. Umidov, Sov. Phys. Crystallogr. 19 (4), 437 (1975)
50. S. V. Semenovskaya, Sov. Phys. Solid State 20 (5), 783 (1978)
51. S. V. Semenovskaya, Phys. Stat. Sol. (b) 87, 733 (1978)
52. S. M. Allen and J.W. Cahn, Bulletin of Alloy Phase Diagrams 3, 287 (1982)
53. G. Inden and W. Pitsch, Z. Metal. 63, 253 (1972)
54. R. Kichuchi and J. W. Cahn, J. Phys. Chem. Sol. 23, 137 (1962)
55. H. E. Cook and J. E. Hilliard, J. Appl. Phys. 40, 2191 (1969)
56. I. M. Lifshitz, Soviet Physics JETP 15, 939 (1962)
57. M. G. Mendiratta and S. K. Ehlers, Met. Trans. A. 14A, 2435 (1983)
58. M. J. Marcinkowski and N. Brown, J. Appl. Phys. 33, 537 (1962)
59. E. E. Underwood, Quantitative Stereology, P.81, Addison-Wesley, Reading, MA (1970)
60. R. C. Sun and C. L. Bauer, Acta Met. 18, 635 (1970)
61. W. W. Mullins, J. Appl. Phys. 27, 900 (1956)
62. J. E. Hilliard, Metal Progress 85, 99 (1964)
63. K. Nishida, T. Yamamoto, and T. Nagata, Trans. JIM 12, 310 (1971)
64. A. B. Kuper, D. Lazarus, J. R. Manning and C. T. Tomizuka, Phys. Rev. 104, 1536 (1956)
65. R. C. Crawford, Phil. Mag. 35, 567 (1977)
66. R. C. Crawford and I. L. F. Ray, Phil. Mag. 35, 549 (1977)
67. H. J. Leamy, F. X. Kayser and M. J. Marcinkowski, Phil. Mag. 20, 779 (1969)
68. I. L. F. Ray, R. C. Crawford and D. J. H. Cockayne, Phil. Mag. 21, 1027 (1970)
69. R. C. Crawford, I. L. F. Ray and D. J. H. Cockayne, Phil. Mag. 27, 1 (1973)
70. H. J. Leamy and F. X. Kayser, Phys. Stat. Sol. 34, 765 (1969)
71. Y. W. Lee and H. I. Aaronson, Acta Met. 28, 539 (1980)
72. R. G. van der Heide, Ph.D. Thesis Research, Dept. of Mat. Sci. Eng. M.I.T. (1988)
73. J. W. Cahn, J. Chem. Phys. 66, 3667 (1977)
74. F. B. Hildebrand, Methods of Applied Mathematics, P. 119, Prentice Hall, Englewook Cliffs, N.J., (1965)
75. NAG FORTRAN LIBRARY MANUAL, Mark 10, Numerical Alogrithms Group, Oxford, UK (1983)
76. J. W. Cahn and R. Kikuchi, J. Phys. Chem. Solids 27, 1305 (1976)
77. R. C. Crawford, Phil. Mag. 33, 529 (1956)
78. J. W. Cahn, 'Thermodynamics of Solid and Fluid Surfaces', in "Interfacial Segregation", American Society of Metals, Metals Park, Ohio pp 17-18 (1979)

79. M. G. Mendiratta and H. A. Lipsitt, High-Temperature Ordered Intermetallic Alloys, C. C. Koch, C. T. Liu and N. S. Stoloff, eds., Materials Research Society, Pittsburgh, PA, pp 155-162 (1985)
80. R. Herschitz and D. N. Seidman, Acta Met. 33, 1547 (1985)
81. R. Herschitz and D. N. Seidman, Acta Met. 33, 1565 (1985)
82. P. A. Beaven, M. K. Miller and G.D.W. Smith, Proc. Conf. on Phase Transformations, York, UK, Inst. of Metallurgists Conf. Series 3, No. 11, 2, 98 (1979)
83. C. M. Bedell, B.S. Thesis, Dept. of Mat. Sci. Eng. M.I.T., Cambridge, Mass. (1983)

BIOGRAPHICAL NOTES

The author was born in Seoul, Korea in January, 1958. He graduated from Kyunggi High School in 1976.

As an undergraduate he attended Seoul National University in Seoul, Korea where he graduated with honor in 1980. In 1982 he received an M.S. in Metallurgical Engineering from Seoul National University.

He spent the summer of 1982 at Yale University, New Haven before coming to M.I.T. At M.I.T. he has been working as a graduate research assistant to Professor Samuel M. Allen since September 1982.

He got married to Grace Young Min Choi in May 1983, and has been having a happy family life ever since. They have a lovely daughter Jane Kyungjoo Park who was born in February 1985.